

Robert Johannes Triebel, BSc

Wannier charge centers and the calculation of topological invariants: Application to the Kane-Mele-Hubbard model

MASTER THESIS

For obtaining the academic degree
Diplom-Ingenieur

Master Programme of
Technical Physics



Graz University of Technology

Supervisor:

Univ.-Prof. Dr.rer.nat. Enrico Arrigoni

Co-Supervisor:

Dr.techn. Markus Aichhorn

Institute of Theoretical and Computational Physics

Graz, March 2015

Acknowledgements

I would like to thank Prof. Arrigoni for the supervision of my work. He was a great help in understanding concepts of many-body physics and had always time for questions and concerns.

Furthermore, I owe my gratitude to Markus Aichhorn. He was the driving force in developing the framework of this thesis and helped a lot with distinguished advice, always willing to listen to me.

I am thankful to Prof. von der Linden for helpful discussion. I am also grateful to the other members of the Institute of Theoretical and Computational Physics for the great atmosphere and their willingness to discuss upcoming problems. Here I would like to emphasize Manuel Zingl, whose cooperation helped me to solve many minor problems of daily work.

Last but not least I would like to thank my parents and my whole family, who have always been there for me and helped me in all regards.

Abstract

Topological insulators are a class of materials different from trivial band insulators. The topological order of the insulators, classified by invariants, is the reason for gapless states emerging at the surface. Currently, they are in the spotlight of theoretical as well as experimental physics due to the possible applications of such edge states in quantum computing. Of certain interest is the influence of strong electron-electron interaction, which is investigated in this thesis. The system used here is the Kane-Mele-Hubbard (KMH) model, which is an interacting two-dimensional tight-binding model on a honeycomb lattice. Unlike trivial models for graphene, a spin-orbit coupling is added that gaps the system and leads to a nontrivial topology. To test a possible evaluation of topological invariants using Wannier charge centers (WCC), the noninteracting Kane-Mele model is analyzed in detail. The Hubbard term is first introduced in mean-field (MF) approximation in order to keep the determination of invariants using WCC possible, which requires the existence of Bloch functions. Using this tool, the phase diagram of the KMH model is determined as a function of interaction strength, spin-orbit coupling, on-site potential and Rashba coupling. The resulting topological invariants are compared to the existence of edge states of the MF-KMH model on a zigzag ribbon, showing perfect agreement. Finally, a two-site dynamical impurity approximation (DIA) which is based on the self-energy-functional approach is used to obtain results beyond MF. The topological invariants of this fully interacting system are determined using a so-called topological Hamiltonian in order to allow a calculation with WCC. The DIA results show that the direction of a possible magnetic moment is of great importance in order to calculate topological properties.

Kurzfassung

Topologische Isolatoren sind eine Klasse von Materialien, die sich von gewöhnlichen Band-Isolatoren unterscheiden. Die topologische Ordnung der Isolatoren, klassifiziert durch Invarianten, ist der Grund für die Existenz von Zuständen ohne Bandlücke an der Oberfläche. Derzeit sind sie wegen möglicher Anwendungen dieser Randzustände in der Quanteninformatik im Rampenlicht sowohl in der theoretischen, als auch der experimentellen Physik. Von besonderem Interesse ist der Einfluss von starker Wechselwirkung der Elektronen, die in dieser Arbeit untersucht wird. Das System, das hier verwendet wird, ist das Kane-Mele-Hubbard-Modell (KMH), welches ein zweidimensionales Tight-Binding-Modell auf einem Bienenwabengitter ist. Im Unterschied zu einfachen Modellen von Graphen ist eine Spin-Orbit-Kopplung hinzugefügt, die eine Bandlücke und die nichttriviale Topologie verursacht. Um eine mögliche Bestimmung von topologischen Invarianten unter Verwendung von Wannier-Zentren zu testen, wird das nichtwechselwirkende Kane-Mele-Modell im Detail analysiert. Der Hubbard-Term wird zuerst in einer Mean-Field-Näherung (MF) eingeführt, um die Bestimmung von Invarianten mit Wannier-Zentren zu ermöglichen, welche die Existenz von Bloch-Zuständen voraussetzen. Mit dieser Methode wird das Phasendiagramm des KMH-Modells in Abhängigkeit von der Wechselwirkungsstärke, der Spin-Orbit-Kopplung, einer Energiedifferenz zwischen den Untergittern, und der Rashba-Kopplung bestimmt. Die topologischen Invarianten werden mit der Existenz von Randzuständen des MF-KMH-Modells verglichen und zeigen perfekte Übereinstimmung. Zum Abschluss wurde eine dynamische Störstellen-Näherung (DIA) auf zwei Plätzen, die auf der Selbstenergie-Funktional-Methode fußt, verwendet, um Resultate zu erzielen, die über MF hinausgehen. Die topologischen Invarianten dieses wechselwirkenden Systems wurden mit einem so genannten topologischen Hamilton-Operator bestimmt, um die Berechnung mit Wannier-Zentren zu erlauben. Die DIA Resultate zeigen, dass die Richtung eines möglichen magnetischen Momentes von großer Wichtigkeit sind, um topologische Eigenschaften zu berechnen.

Contents

1	Topological invariants	11
1.1	Berry phase	11
1.2	Chern invariant	12
1.3	Integer Quantum Hall effect	13
1.3.1	Quantum Spin Hall insulator	15
1.4	Time reversal symmetry	16
1.5	Theory of charge polarisation - Wannier functions	17
1.6	Definition of \mathbb{Z}_2 invariant by Fu and Kane	18
1.6.1	Topological systems with inversion symmetry	21
1.7	Soluyanov-Vanderbilt method	21
1.8	Topological invariants for interacting systems	25
1.9	Bulk boundary correspondence	27
2	The Kane-Mele model	31
2.1	Graphene	31
2.2	Haldane model	34
2.3	Kane-Mele model	35
2.3.1	Bloch Hamiltonian	36
2.3.2	Topology in inversion symmetric case	38
2.3.3	Topology in general case	40
2.4	Ribbon	44
2.4.1	Geometry	44
2.4.2	Kane-Mele model on a zigzag ribbon	48
3	Kane-Mele-Hubbard model	53
3.1	Magnetisation	54
3.2	Topological transitions	56
3.2.1	Generalisation of \mathbb{Z}_2 invariant definition	58
3.3	Influence of a sublattice potential	59
3.4	Influence of Rashba coupling	63
3.5	KMH model on a zigzag ribbon	68
3.5.1	Magnetisation	68
3.5.2	Topology and edge states	69
4	KMH beyond mean-field	73
4.1	Self-energy-functional approach	73
4.2	Kane-Mele-Hubbard model in 2 site DIA	76

5	Conclusions and outlook	83
A	Kane-Mele Bloch Hamiltonians	85
A.1	Bulk	85
A.2	Zigzag ribbon	88

Chapter 1

Topological invariants

1.1 Berry phase

In quantum mechanics, wave functions are usually defined up to a phase which has no physical meaning since it vanishes in expectation values which are the only physically relevant quantities. However, Berry has shown in 1984 that a geometric phase which may have observable effects appears if a system is transformed adiabatically in a cyclical manner [1–3].

The derivation given here is following the review of Yoichi Ando [2]. Given a Hamiltonian H which depends on a set of parameters \mathbf{a} which change cyclically over time t , the equation for the eigenvectors $|n, \mathbf{a}(t)\rangle$ reads

$$H[\mathbf{a}(t)] |n, \mathbf{a}(t)\rangle = E_n[\mathbf{a}(t)] |n, \mathbf{a}(t)\rangle. \quad (1.1)$$

Assume the parameters \mathbf{a} change adiabatically from certain values $\mathbf{a}(0) = \mathbf{a}_0$. The associated state evolves in time obeying the time dependent Schrödinger equation

$$H[\mathbf{a}(t)] |n, \mathbf{a}_0\rangle (t) = i\hbar \frac{\partial}{\partial t} |n, \mathbf{a}_0\rangle (t). \quad (1.2)$$

The solution can be expressed in terms of the eigenstates of the explicitly time dependent Hamiltonian in equation (1.1)

$$|n, \mathbf{a}_0\rangle (t) = \exp \left\{ \frac{i}{\hbar} \int_0^t dt' (i\hbar \dot{\mathbf{a}}(t') \langle n, \mathbf{a}(t') | \nabla_{\mathbf{a}} |n, \mathbf{a}(t')\rangle - E_n[\mathbf{a}(t')]) \right\} |n, \mathbf{a}(t)\rangle \quad (1.3)$$

which can be shown by inserting the solution (1.3) in the Schrödinger equation (1.2).

Thus, if the parameters \mathbf{a} change adiabatically, a phase factor consisting of two terms appears. The second term gives the expected time dependence of an eigenstate in a system which does not explicitly depend on time, and is called dynamical phase factor θ_n :

$$\theta_n(t) = -\frac{1}{\hbar} \int_0^t dt' E_n[\mathbf{a}(t')]. \quad (1.4)$$

The first phase in equation (1.3) is nontrivial and is called *Berry phase* γ_n , if the parameters \mathbf{a} describe a closed path C as time evolves from 0 to a period T :

$$\begin{aligned}\gamma_n[C] &\equiv i \int_0^T dt \dot{\mathbf{a}}(t) \cdot \langle n, \mathbf{a}(t) | \nabla_{\mathbf{a}} | n, \mathbf{a}(t) \rangle = i \oint_C d\mathbf{a} \cdot \langle n, \mathbf{a} | \nabla_{\mathbf{a}} | n, \mathbf{a} \rangle = \\ &= - \oint_C d\mathbf{a} \cdot \mathbf{A}_n(\mathbf{a}) = - \int_S d^2\mathbf{a} \cdot \mathbf{F}_n(\mathbf{a}),\end{aligned}\quad (1.5)$$

where we introduced the the Berry connection

$$\mathbf{A}_n(\mathbf{a}) \equiv -i \langle n, \mathbf{a} | \nabla_{\mathbf{a}} | n, \mathbf{a} \rangle \quad (1.6)$$

and the Berry curvature

$$\mathbf{F}_n(\mathbf{a}) \equiv \nabla_{\mathbf{a}} \times \mathbf{A}_n(\mathbf{a}). \quad (1.7)$$

In the last step of equation (1.5), Stokes' theorem has been used.

To conclude, the Berry phase is a phase factor additional to the dynamical one accumulated by following a closed path in parameter space \mathbf{a} . It is important to note that it cannot be removed by a simple gauge transformation

$$|n, \mathbf{a}\rangle \rightarrow |n, \mathbf{a}'\rangle = e^{i\xi_n(\mathbf{a})} |n, \mathbf{a}\rangle \quad (1.8)$$

which is shown for example in [3].

1.2 Chern invariant

In mathematics, Chern numbers are defined for vector bundles on an oriented manifold of even dimension $2n$. Details on the mathematics of Chern classes can be found in several textbooks as for example in [4].

For two-dimensional topological insulators the *Chern topological invariant* of the m^{th} band, which is a first Chern number, is defined by [5]

$$C_m \equiv \frac{1}{2\pi} \int_{BZ} d^2\mathbf{k} \cdot \mathbf{F}_m(\mathbf{k}) = \frac{1}{2\pi} \oint_{\partial BZ} d\mathbf{k} \cdot \mathbf{A}_m(\mathbf{k}) = \frac{1}{2\pi} \gamma_m[\partial BZ], \quad (1.9)$$

with $\mathbf{F}_m(\mathbf{k}) = \nabla_{\mathbf{k}} \times \mathbf{A}_m(\mathbf{k})$ and $\mathbf{A}_m(\mathbf{k}) = i \langle u_{m\mathbf{k}} | \nabla_{\mathbf{k}} | u_{m\mathbf{k}} \rangle$. Hence, the Chern invariant is up to a factor of 2π a Berry phase. The set of parameters which are changed adiabatically in the eigenvalue equation (1.1) is the wave vector \mathbf{k} , the closed path is the boundary of the Brillouin zone.

The Chern invariant is not necessarily uniquely defined, in case of degeneracies it can depend on gauge. However, the total Chern invariant, which is the sum of Chern invariants related to occupied bands, is an uniquely defined integer if the gap between filled and empty bands remains finite [6, 7],

$$C = \sum_{m \text{ occupied}} C_m. \quad (1.10)$$

If the Hamiltonian of a band can be written as $H_m(\mathbf{k}) = \mathbf{h}_m(\mathbf{k}) \cdot \boldsymbol{\sigma}$, where $\boldsymbol{\sigma}$ is the vector of Pauli matrices, the Chern number reads [8]

$$C_m = \frac{1}{4\pi} \int d^2k \left[\frac{\partial \hat{\mathbf{h}}_m(\mathbf{k})}{\partial k_x} \times \frac{\partial \hat{\mathbf{h}}_m(\mathbf{k})}{\partial k_y} \right] \cdot \hat{\mathbf{h}}_m(\mathbf{k}). \quad (1.11)$$

The hat denotes the normalized vector $\hat{\mathbf{h}} = \mathbf{h}/|\mathbf{h}|$.

1.3 Integer Quantum Hall effect

The first experiment of an effect that is fundamentally based on a nontrivial Chern number was the discovery of the quantum Hall effect under high magnetic fields at low temperature by von Klitzing *et al.* in 1980 [9]. The astonishing result was that the longitudinal conductivity σ_{xx} vanishes whereas the Hall conductance σ_{xy} is quantised to integer multiples of e^2/h :

$$\sigma_{xy} = n \frac{e^2}{h}. \quad (1.12)$$

The quantisation is due to the topological nontrivial structure of the bands, as Thouless, Kohmoto, Nightingale and den Nijs (TKNN) have shown in 1982 [5, 10]. Hereafter, a short derivation of the TKNN invariant n is given, following the review by Ando [2]. In order to highlight operators, they are denoted by hats.

Since the Hall conductivity is given by

$$\sigma_{xy} \equiv \frac{\langle \hat{j}_x \rangle_E}{E_y}, \quad (1.13)$$

an expression for the expectation value of the current density given a certain electric field \mathbf{E} has to be found.

Let's consider a 2D electron system of size $L \times L$ with an electric field E in y direction and a magnetic field in z direction. If the electric field is homogeneous, the potential can be set to $V(\mathbf{x}) = -eEy$. Perturbation theory gives as a first order correction of the eigenstates

$$|n\rangle_E = |n\rangle + \sum_{m(\neq n)} \frac{\langle m | (-eE\hat{y}) | n \rangle}{E_n - E_m} |m\rangle + \mathcal{O}(E^2). \quad (1.14)$$

The current density $\langle \hat{j}_x \rangle$ is given by

$$\langle \hat{j}_x \rangle_E = \sum_n f(E_n) \left\langle n \left| \frac{e\hat{v}_x}{L^2} \right| n \right\rangle_E = \frac{e}{L^2} \sum_n f(E_n) \langle n | \hat{v}_x | n \rangle_E \quad (1.15)$$

where $f(E)$ is the Fermi Dirac distribution and v_x the velocity in x direction.

Up to the first order of the electric field E , the solution is

$$\begin{aligned} \langle \hat{j}_x \rangle_E &\approx \langle \hat{j}_x \rangle_0 + \frac{1}{L^2} \sum_n f(E_n) \times \\ &\times \sum_{m(\neq n)} \frac{\langle n | e\hat{v}_x | m \rangle \langle m | (-eE\hat{y}) | n \rangle + \langle n | (-eE\hat{y}) | m \rangle \langle m | e\hat{v}_x | n \rangle}{E_n - E_m} \\ &= \frac{e^2 \hbar E}{iL^2} \sum_n f(E_n) \sum_{m(\neq n)} \frac{\langle n | \hat{v}_x | m \rangle \langle m | \hat{v}_y | n \rangle - \langle n | \hat{v}_y | m \rangle \langle m | \hat{v}_x | n \rangle}{(E_n - E_m)^2}. \end{aligned} \quad (1.16)$$

In the last step, the equality

$$\langle m | \hat{v}_i | n \rangle = \frac{1}{i\hbar} (E_n - E_m) \langle m | \hat{x}_i | n \rangle \quad (1.17)$$

has been used, which follows from the Heisenberg equation of motion $\frac{d}{dt} \hat{x}_i = \hat{v}_i = \frac{1}{i\hbar} [\hat{x}_i, H]$. If the labels n and m are exchanged in the second term of the numerator, the Hall conductivity given by equations (1.13) and (1.16) is simplified to

$$\sigma_{xy} = \frac{e^2 \hbar}{iL^2} \sum_n \sum_{m(\neq n)} (f(E_n) - f(E_m)) \frac{\langle n | \hat{v}_x | m \rangle \langle m | \hat{v}_y | n \rangle}{(E_n - E_m)^2}. \quad (1.18)$$

In the limit $T \rightarrow 0$, the Fermi functions become Heaviside functions $F(E) = \Theta(E_F - E)$. Reversing the exchange of n and m , the *Nakano-Kubo* formula

$$\sigma_{xy} = \frac{e^2 \hbar}{iL^2} \sum_{E_n < E_F} \sum_{E_m > E_F} \frac{\langle n | \hat{v}_x | m \rangle \langle m | \hat{v}_y | n \rangle - \langle n | \hat{v}_y | m \rangle \langle m | \hat{v}_x | n \rangle}{(E_n - E_m)^2} \quad (1.19)$$

is obtained, that is also used by Kohmoto [5]. Further evaluation is possible if the eigenfunctions are written in momentum space as Bloch functions $|n\rangle = |u_{n\mathbf{k}}\rangle$, $|m\rangle = |u_{m\mathbf{k}'}\rangle$. The matrix elements of the velocity operator are transformed back to matrix elements of the position operator using equation (1.17). The position operator is then acting on the Bloch wave as a derivative, i.e. $\hat{x}_i \rightarrow i \frac{\partial}{\partial k_i}$, as known from basic quantum mechanics [11]. The resulting matrix elements are thus [2, 5]

$$\begin{aligned} \langle u_{n\mathbf{k}} | \hat{v}_i | u_{m\mathbf{k}'} \rangle &= \frac{1}{\hbar} (E_{n\mathbf{k}} - E_{m\mathbf{k}'}) \left\langle u_{n\mathbf{k}} \left| \frac{\partial u_{m\mathbf{k}'}}{\partial k'_i} \right. \right\rangle = \\ &= -\frac{1}{\hbar} (E_{n\mathbf{k}} - E_{m\mathbf{k}'}) \left\langle \frac{\partial u_{n\mathbf{k}}}{\partial k_i} \left| u_{m\mathbf{k}'} \right. \right\rangle. \end{aligned} \quad (1.20)$$

Using these equations, the Nakano-Kubo formula becomes

$$\begin{aligned} \sigma_{xy} &= \frac{e^2}{i\hbar L^2} \sum_{\substack{\mathbf{k} E_n < E_F \\ \mathbf{k}' E_m > E_F}} \left(\left\langle \frac{\partial u_{n\mathbf{k}}}{\partial k_x} \left| u_{m\mathbf{k}'} \right. \right\rangle \left\langle u_{m\mathbf{k}'} \left| \frac{\partial u_{n\mathbf{k}}}{\partial k_y} \right. \right\rangle - \right. \\ &\quad \left. - \left\langle \frac{\partial u_{n\mathbf{k}}}{\partial k_y} \left| u_{m\mathbf{k}'} \right. \right\rangle \left\langle u_{m\mathbf{k}'} \left| \frac{\partial u_{n\mathbf{k}}}{\partial k_x} \right. \right\rangle \right) \end{aligned} \quad (1.21)$$

The summation over m can be reduced due to the completeness relation

$$\sum_{\mathbf{k}' E_m > E_F} |u_{m\mathbf{k}'}\rangle \langle u_{m\mathbf{k}'}| = \mathbb{1} - \sum_{\mathbf{k}' E_m < E_F} |u_{m\mathbf{k}'}\rangle \langle u_{m\mathbf{k}'}|. \quad (1.22)$$

The term resulting from the second part is identical to the sum in equation (1.21) except that $E_m < E_F$ instead of $E_m > E_F$. Because of this change, the term is now asymmetric in exchanging the indices $n\mathbf{k}$ and $m\mathbf{k}'$, wherefore the sum must vanish. This can be seen by applying all differential operators to the corresponding bra vectors instead of the ket vectors, which gives a minus sign according to equation (1.20), i.e.

$$\left\langle \frac{\partial u_{n\mathbf{k}}}{\partial k_x} \middle| u_{m\mathbf{k}'} \right\rangle \left\langle u_{m\mathbf{k}'} \middle| \frac{\partial u_{n\mathbf{k}}}{\partial k_y} \right\rangle - \left\langle \frac{\partial u_{n\mathbf{k}}}{\partial k_y} \middle| u_{m\mathbf{k}'} \right\rangle \left\langle u_{m\mathbf{k}'} \middle| \frac{\partial u_{n\mathbf{k}}}{\partial k_x} \right\rangle = \quad (1.23)$$

$$= - \left\langle \frac{\partial u_{n\mathbf{k}}}{\partial k_x} \middle| u_{m\mathbf{k}'} \right\rangle \left\langle \frac{\partial u_{m\mathbf{k}'}}{\partial k'_y} \middle| u_{n\mathbf{k}} \right\rangle + \left\langle \frac{\partial u_{n\mathbf{k}}}{\partial k_y} \middle| u_{m\mathbf{k}'} \right\rangle \left\langle \frac{\partial u_{m\mathbf{k}'}}{\partial k'_x} \middle| u_{n\mathbf{k}} \right\rangle. \quad (1.24)$$

The last term is obviously antisymmetric in $n\mathbf{k} \leftrightarrow m\mathbf{k}'$. As mentioned above, the sum therefore vanishes and the conductivity (1.21) simplifies to

$$\sigma_{xy} = \frac{e^2}{i\hbar L^2} \sum_{\mathbf{k} E_n < E_F} \left(\left\langle \frac{\partial u_{n\mathbf{k}}}{\partial k_x} \middle| \frac{\partial u_{n\mathbf{k}}}{\partial k_y} \right\rangle - \left\langle \frac{\partial u_{n\mathbf{k}}}{\partial k_y} \middle| \frac{\partial u_{n\mathbf{k}}}{\partial k_x} \right\rangle \right). \quad (1.25)$$

The sum over n with the restriction $E_n < E_F$ is equivalent to a sum over occupied bands if the band structure is gapped, which is assumed from now on. The summation over \mathbf{k} is replaced by an integral $\sum_{\mathbf{k}} \rightarrow (\frac{L}{2\pi})^2 \int d^2k$ if the crystal size tends to infinity, which leads to

$$\begin{aligned} \sigma_{xy} &= -\frac{ie^2}{h2\pi} \sum_{n \text{ occupied}} \int d^2k \left(\left\langle \frac{\partial u_{n\mathbf{k}}}{\partial k_x} \middle| \frac{\partial u_{n\mathbf{k}}}{\partial k_y} \right\rangle - \left\langle \frac{\partial u_{n\mathbf{k}}}{\partial k_y} \middle| \frac{\partial u_{n\mathbf{k}}}{\partial k_x} \right\rangle \right) = \\ &= -\frac{ie^2}{h2\pi} \sum_{n \text{ occupied}} \int d^2k \left(\frac{\partial}{\partial k_x} \left\langle u_{n\mathbf{k}} \middle| \frac{\partial u_{n\mathbf{k}}}{\partial k_y} \right\rangle - \frac{\partial}{\partial k_y} \left\langle u_{n\mathbf{k}} \middle| \frac{\partial u_{n\mathbf{k}}}{\partial k_x} \right\rangle \right) = \\ &= -\frac{e^2}{h2\pi} \sum_{n \text{ occupied}} \int d^2k (\nabla_{\mathbf{k}} \times \mathbf{A}_n(\mathbf{k}))_z = -\frac{e^2}{h2\pi} \sum_{n \text{ occupied}} \int d^2k (\mathbf{F}_n)_z = \\ &= -\frac{e^2}{h} \sum_{n \text{ occupied}} C_n = -\frac{e^2}{h} C. \end{aligned} \quad (1.26)$$

Hence it is proven that the TKNN invariant in equation (1.12) is minus the Chern number, i.e. $n = -C$.

1.3.1 Quantum Spin Hall insulator

It is possible that a system has a Hall conductivity equal to zero $\sigma_{xy} = 0$, but a nonzero spin Hall conductivity $\sigma_{xy}^s \equiv \hbar/2e(\sigma_{xy}^\uparrow - \sigma_{xy}^\downarrow)$, when a finite spin current $\mathbf{J}_s \equiv (\hbar/2e)(\mathbf{J}_\uparrow - \mathbf{J}_\downarrow)$ exists [12, 13]. If the spin is conserved, the spin Hall conductivity is also quantized for the same reason as the Hall conductivity

and takes only multiples of $e/2\pi$. The multiplicative integer is minus the spin Chern number [14, 15]:

$$C^s = \sum_{\sigma} \sigma C^{\sigma} = (C^{\uparrow} - C^{\downarrow})/2. \quad (1.27)$$

The topological spin properties are mostly determined by a \mathbb{Z}_2 invariant [7]

$$\nu = C^s \pmod{2}. \quad (1.28)$$

If the spin in z direction, S_z , is not conserved, definition (1.27) cannot be used to calculate a spin Chern number and σ_{xy}^s is not quantized any more [13], but according to [15] it is possible that a quantum spin Hall phase with a quantized quantity ν persists if spin Chern numbers are defined differently. Further definitions of the \mathbb{Z}_2 invariant are given in the sections 1.6 and 1.8.

1.4 Time reversal symmetry

Since spin \mathbf{S} is an angular momentum it should pick up a minus sign under time reversal transformation \mathcal{T} : $t \mapsto -t \Rightarrow \mathbf{S} \mapsto -\mathbf{S}$. A matrix representation Θ of the time reversal transformation \mathcal{T} must therefore obey

$$\Theta \mathbf{S} \Theta^{-1} = -\mathbf{S}. \quad (1.29)$$

A possible representation of Θ for spin 1/2 particles is [16]

$$\Theta = e^{-i\pi S_y/\hbar} K = e^{-i\pi \sigma_y/2} K = -i\sigma_y K, \quad (1.30)$$

where K denotes the operator of complex conjugation. An important theorem in this context is Kramers' theorem which states that the energy eigenvalues of a system with an odd number of fermions are at least two fold degenerate if time reversal symmetry is assured [16]. This is especially important in the case of band structures, which are the one particle energies as a function of \mathbf{k} , as demonstrated in the review of Yoichi Ando [2], which is the guidance for the following lines.

In a periodic system, eigenvectors can be labeled by a band index n and the wave vector \mathbf{k} .

$$H |\psi_{n\mathbf{k}}\rangle = E_{n\mathbf{k}} |\psi_{n\mathbf{k}}\rangle \quad (1.31)$$

Due to Bloch's theorem, the eigenstates can be written as a product of a plane wave with a vector that has the same translational symmetry as the lattice,

$$|\psi_{n\mathbf{k}}\rangle = e^{i\mathbf{k}\cdot\mathbf{r}} |u_{n\mathbf{k}}\rangle. \quad (1.32)$$

Here, $|u_{n\mathbf{k}}\rangle$ is an eigenvector of the Bloch Hamiltonian $H(\mathbf{k}) = e^{-i\mathbf{k}\cdot\mathbf{r}} H e^{i\mathbf{k}\cdot\mathbf{r}}$ and obeys therefore the reduced Schrödinger equation

$$H(\mathbf{k}) |u_{n\mathbf{k}}\rangle = E_{n\mathbf{k}} |u_{n\mathbf{k}}\rangle. \quad (1.33)$$

If the system preserves time reversal symmetry, i.e. $[H, \Theta] = 0$, the Bloch Hamiltonian satisfies

$$H(-\mathbf{k}) = \Theta H(\mathbf{k}) \Theta^{-1}. \quad (1.34)$$

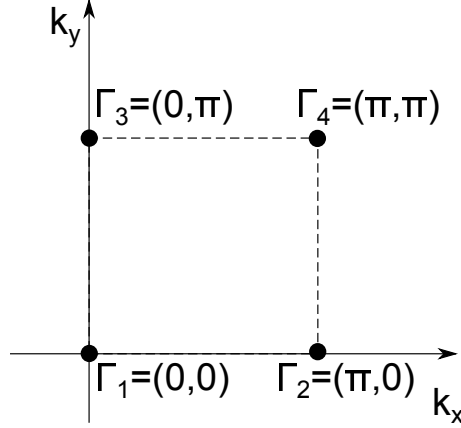


Figure 1.1: Time reversal invariant momenta Γ_i of a 2D quadratic lattice.

This means that Bloch waves with reverse momenta \mathbf{k} and $-\mathbf{k}$ have the same energy. These *Kramers pairs* are an important special case of Kramers degeneracy mentioned above. Accordingly, if \mathbf{k} and $-\mathbf{k}$ are equivalent points in the Brillouin zone, the bands are degenerate at these so called time reversal invariant momenta (TRIM). For example, the TRIM of a simple square lattice are situated at the corners of a square with length π , as shown in figure 1.1.

1.5 Theory of charge polarisation - Wannier functions

As a basis set for periodic Hamiltonians usually Bloch waves $|\psi_{n\mathbf{k}}\rangle = e^{i\mathbf{k}\cdot\mathbf{r}} |u_{n\mathbf{k}}\rangle$ are used, see equations (1.31-1.33). Hence, the wave functions are commonly labelled by their band index n and their momentum \mathbf{k} . This representation has the drawback that it is not suited to receive any information about the localisation of the electrons within a unit cell. For this purpose, Wannier functions are superior. The Wannier function in cell \mathbf{R} of band n is defined by [17]

$$|\mathbf{R}n\rangle \equiv \frac{V}{(2\pi)^D} \int d^D k e^{-i\mathbf{k}\cdot\mathbf{R}} |\psi_{n\mathbf{k}}\rangle, \quad (1.35)$$

the inverse transformation is

$$|\psi_{n\mathbf{k}}\rangle = \sum_{\mathbf{R}} e^{i\mathbf{k}\cdot\mathbf{R}} |\mathbf{R}n\rangle. \quad (1.36)$$

With this definition one can define a charge center of band n by

$$\bar{\mathbf{r}}_n \equiv \langle \mathbf{0}n | \mathbf{r} | \mathbf{0}n \rangle. \quad (1.37)$$

The spread of a Wannier function around the center is given by $\langle r^2 \rangle_n - \bar{\mathbf{r}}_n^2 = \langle \mathbf{0}n | r^2 | \mathbf{0}n \rangle - \bar{\mathbf{r}}_n^2$.

The connection of Wannier functions to topology is due to a relation presented in [18], which links matrix elements of the position operator in the Wannier basis to the Berry connection $\mathbf{A}_n(\mathbf{k}) = -i \langle u_{n\mathbf{k}} | \nabla_{\mathbf{k}} | u_{v\mathbf{k}} \rangle$:

$$\langle \mathbf{R}n | \mathbf{r} | \mathbf{0}m \rangle = i \frac{V}{(2\pi)^3} \int d^3k e^{i\mathbf{k}\cdot\mathbf{R}} \langle u_{n\mathbf{k}} | \nabla_{\mathbf{k}} | u_{m\mathbf{k}} \rangle. \quad (1.38)$$

With this expression one can easily formulate the charge center as well as the spread in terms of Bloch functions $|u_{n\mathbf{k}}\rangle$ [19]:

$$\bar{\mathbf{r}}_n = i \frac{V}{(2\pi)^3} \int d^3k \langle u_{n\mathbf{k}} | \nabla_{\mathbf{k}} | u_{n\mathbf{k}} \rangle \quad (1.39)$$

$$\langle r^2 \rangle_n = \frac{V}{(2\pi)^3} \int d^3k |\nabla_{\mathbf{k}} | u_{n\mathbf{k}} \rangle|^2 \quad (1.40)$$

However, the definition of all quantities above is not unique since the Bloch functions associated with the Wannier functions have a gauge freedom. One can modify the basis function by a phase

$$|u_{n\mathbf{k}}\rangle \rightarrow e^{i\phi_n(\mathbf{k})} |u_{n\mathbf{k}}\rangle \quad (1.41)$$

and still preserve a valid set of Bloch functions. The Wannier center $\bar{\mathbf{r}}_n$ remains the same, modulo a lattice vector, whereas the spread changes [19]. In general, one can transform not only a single Bloch function, but also a set of Bloch functions using a unitary matrix U_{mn} :

$$|u_{n\mathbf{k}}\rangle \rightarrow \sum_m U_{mn}(\mathbf{k}) |u_{m\mathbf{k}}\rangle. \quad (1.42)$$

The new set of vectors $|u_{n\mathbf{k}}\rangle$ are not necessarily eigenvectors of $H(\mathbf{k})$ as defined in equation (1.33) any more but span still the whole space. Furthermore, the generalized gauge transformation changes also the Wannier charge centers $\bar{\mathbf{r}}_n$, the only quantity preserved (up to a lattice vector) is the total charge center $\sum_n \bar{\mathbf{r}}_n$.

1.6 Definition of \mathbb{Z}_2 invariant by Fu and Kane

In their original work [20] Fu and Kane considered a one dimensional periodic Hamiltonian H with a lattice constant $a = 1$, length L and periodic boundary conditions. Furthermore, H changes adiabatically with a pumping parameter t . This parameter is periodic with period T

$$H[t + T] = H[t] \quad (1.43)$$

and odd under time reversal Θ

$$H[-t] = \Theta H[t] \Theta^{-1}. \quad (1.44)$$

The idea is now to use Wannier charge centers (WCCs) to describe the topological properties of this system, since the expression for charge centers (1.39) is proportional to a Berry phase (1.5). In our 1D case, the expression for a polarisation P^n reads

$$P^n \equiv \langle 0n | x | 0n \rangle = \frac{i}{2\pi} \int_{-\pi}^{\pi} dk \langle u_{n\mathbf{k}} | \partial_k | u_{n\mathbf{k}} \rangle = C_n \quad (1.45)$$

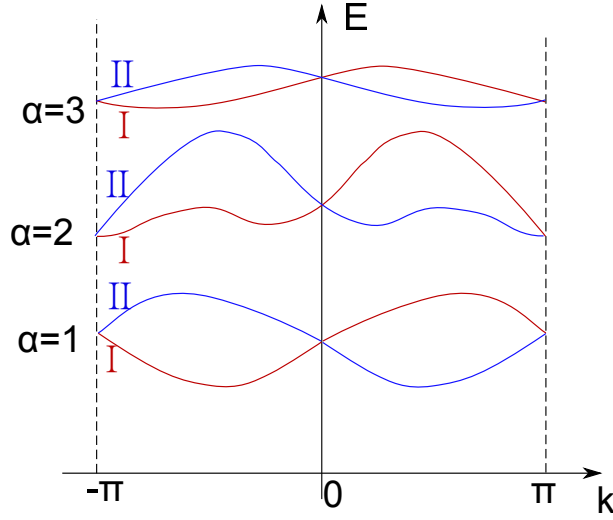


Figure 1.2: Kramers pairs of bands of a 1D time reversal invariant system without additional degeneracies.

and is hence exactly the first Chern number C_n . Note that the charge polarisation is a Wannier charge center \bar{x}_n , but in [20] and related papers it is denoted by P^n , wherefore this notation is also used here. The total charge polarisation is given by $P_\rho = \sum_n P^n$. As already mentioned, the charge polarisation is only defined up to a lattice constant, but if one changes $H(t)$ adiabatically from an initial value t_1 to a final value t_2 and defines $|u_{nk}\rangle$ continuously, the change of charge polarisation is well defined:

$$P_\rho[t_1] - P_\rho[t_2] = \frac{1}{2\pi} \int_{-\pi}^{\pi} dk (A(t_1, k) - A(t_2, k)). \quad (1.46)$$

As in section 1.2, $A(t, k) = i \sum_n \langle u_{nk}(t) | \partial_k | u_{nk}(t) \rangle$ denotes the Berry connection. Considering k and t as two independent coordinates of a 2D system, a Berry curvature can be defined as

$F(k, t) = i \sum_n (\langle \partial_t u_{nk}(t) | \partial_k u_{nk}(t) \rangle - \langle \partial_k u_{nk}(t) | \partial_t u_{nk}(t) \rangle)$, then the change in charge polarisation reads

$$P_\rho[t_1] - P_\rho[t_2] = \frac{1}{2\pi} \int_{-\pi}^{\pi} dk \int_{t_1}^{t_2} dt F(k, t). \quad (1.47)$$

If the integration in time is over a full period, the difference in polarisation $P_\rho[0] - P_\rho[T]$ is the total Chern number of a 2D system with coordinates (k, t) , as can be seen by comparing with the definition (1.9). Since H is supposed to be time reversal invariant, $F(-k, -t) = -F(k, t)$ and hence the total Chern number is zeros. However, as explained in section 1.4, only half period is needed to describe the system because of Kramers pairs. The idea of Fu and Kane was now [20] to split the total charge polarisation P_ρ in two parts. The $2N$ bands are labelled by the number of the related Kramers pair $\alpha = 1, \dots, N$ and a further label within a certain pair $s = \text{I, II}$, see figure 1.2. A consequence of Kramers degeneracy is that a state obtained by time reversing a Bloch function $u_{\alpha, k}^{\text{I}}$ has

to be, up to a phase $\chi_{\alpha,k}$, its Kramers partner $u_{\alpha,-k}^{\text{II}}$. The Bloch waves within a band are thus related by

$$|u_{\alpha,-k}^{\text{I}}\rangle = -e^{i\chi_{\alpha,k}} \Theta |u_{\alpha,k}^{\text{II}}\rangle \quad (1.48)$$

$$|u_{\alpha,-k}^{\text{II}}\rangle = e^{i\chi_{\alpha,-k}} \Theta |u_{\alpha,k}^{\text{I}}\rangle. \quad (1.49)$$

The second equation follows from the first and the properties of the time reversal operator. The splitting of the Kramers pairs allows the definition of *partial polarisations* P^{I} and P^{II} given by

$$P^s = \frac{1}{2\pi} \int_{-\pi}^{\pi} dk A^s(k), \quad (1.50)$$

$$A^s(k) = i \sum_{\alpha=1}^N \langle u_{\alpha k}^s | \partial_k | u_{\alpha k}^s \rangle. \quad (1.51)$$

Obviously, the total charge polarisation is the sum of the two partial polarisations $P_\rho = P^{\text{I}} + P^{\text{II}}$. For the definition of the \mathbb{Z}_2 invariant, the difference of the partial polarisations, called time reversal polarisation

$$P_\theta \equiv P^{\text{I}} - P^{\text{II}} \quad (1.52)$$

is needed. Taking the time reversal invariance into consideration, integrating over half a period is sufficient to determine properties of the system. The \mathbb{Z}_2 invariant for time reversal invariant systems is thus defined by

$$\nu \equiv P_\theta[T/2] - P_\theta[0] \pmod{2}. \quad (1.53)$$

In the same paper [20], Fu and Kane also presented a method to determine the invariant. The method is not used in this thesis, but it is explained for completeness. The most important quantities for that purpose are the overlap matrices of time reversed Bloch states

$$w_{mn}(k) = \langle u_{m,-k} | \Theta | u_{n,k} \rangle. \quad (1.54)$$

Because of equation (1.48), $w(k)$ are direct products of 2×2 matrices where the off-diagonal elements are the complex phases $e^{i\chi_{\alpha,k}}$ and $e^{i\chi_{\alpha,-k}}$. Especially, in the case of the two time reversal invariant momenta (TRIM) $k = 0$ and $k = \pi$, the matrices $w(k)$ are antisymmetric. Remarkably, it can be shown [20] that only the time reversal overlap matrices at $k = \{0, \pi\}$ and $t = \{0, T/2\}$ are necessary to determine the \mathbb{Z}_2 invariant. These four momentum/time pairs are denoted $\mathbf{\Gamma}_i$ and the invariant can be calculated from

$$(-1)^\nu = \prod_{i=1}^4 \delta_i \quad \text{with} \quad \delta_i = \frac{\sqrt{\det[w(\mathbf{\Gamma}_i)]}}{\text{Pf}[w(\mathbf{\Gamma}_i)]}. \quad (1.55)$$

Since the Pfaffian Pf, which is only defined for antisymmetric matrices as it is the case for $w(\mathbf{\Gamma}_i)$, is the square root of the determinant, only the branch of the square root in equation (1.55) determines the sign of δ_i . The branch has to be chosen such that the $|u_{nk}\rangle$ as well as $\sqrt{\det[w(k)]}$ are continuous between $k = 0$ and $k = \pi$. To implement a local gauge satisfying this is the most challenging

part of this method.

The motivation here was given for a 1D system depending on an adiabatic pumping parameter t . For two-dimensional systems the \mathbb{Z}_2 invariant can be defined and calculated similarly, one just has to identify the momentum in the second direction k_y as the pumping parameter, thus all quantities depend on (k_x, k_y) instead of (k, t) . Equation (1.55) is still valid, Γ_i are the TRIM $(0, 0)$, $(0, \pi)$, $(\pi, 0)$ and (π, π) (see figure 1.1). The continuity of $|u_{n\mathbf{k}}\rangle$ and $\sqrt{\det[w(\mathbf{k})]}$ has to be satisfied along two opposing edges of the square defined by the four TRIM, so either from $(0, 0)$ to $(0, \pi)$ and from $(\pi, 0)$ and (π, π) , or from $(0, 0)$ to $(\pi, 0)$ and from $(0, \pi)$ to (π, π) .

1.6.1 Topological systems with inversion symmetry

As mentioned above, to use equation (1.55) a local gauge has to be used such that the eigenstates are continuous between the TRIM. Fortunately, for the special case of Hamiltonians with inversion symmetry it is possible to reformulate this equation so that no knowledge of the eigenstates between the TRIM is necessary.

Inversion symmetry means that mirroring the lattice at an inversion center i leaves the Hamiltonian invariant. Usually, i defines the origin O of the unit cell which means inversion is realized by the parity operation \mathcal{P} which maps all vectors in real space to its negative, i.e. $\mathcal{P}: \mathbf{x} \mapsto -\mathbf{x}$. If a Hamiltonian is inversion symmetric, the Bloch matrix $H(\mathbf{k})$ commutes with a matrix representation P of the parity transformation \mathcal{P} . Thus, a complete set of common eigenvectors exists [21]. The Bloch functions $|u_{n\mathbf{k}}\rangle$ are therefore eigenfunctions of the parity operator P with eigenvalues $\xi_n = \pm 1$.

If the Hamiltonian is furthermore time reversal invariant, the eigenfunctions can be divided in Kramers pairs (see section 1.4). The parity eigenvalue of eigenfunctions belonging to the same Kramers pair are equal $\xi_\alpha^I = \xi_\alpha^{II} = \xi_\alpha$ [22]. It can be shown that the \mathbb{Z}_2 invariant is given just by the eigenvalues ξ_α of the parity operator of the Kramers pair α at the TRIM Γ_i [22].

$$(-1)^\nu = \prod_{i=1}^4 \delta_i \quad \text{with} \quad \delta_i = \prod_{\alpha=1}^N \xi_\alpha(\Gamma_i) \quad (1.56)$$

The calculation of δ_i is here much simpler than in the more general equation (1.55) since no continuous gauge between the TRIM has to be found.

1.7 Soluyanov-Vanderbilt method to determine the \mathbb{Z}_2 invariant

The method described in this section was first published by Soluyanov and Vanderbilt [23] and is based on definition (1.53). Since in this thesis only two-dimensional systems where k_y plays the role of the pumping parameter t are considered, I use in this section only the notation (k_x, k_y) rather than the parametrisation (k, t) which is used in section 1.6 and the original papers [20]

and [23].

In this 2D parametrisation the Wannier functions of interest are the hybrid Wannier functions where in contrast to definition (1.35) only one coordinate is transformed from momentum k to spacial coordinates,

$$|R_x k_y n\rangle = \frac{1}{2\pi} \int_{-\pi}^{\pi} dk_x e^{-iR_x k_x} |\psi_{n\mathbf{k}}\rangle. \quad (1.57)$$

The Wannier charge center (WCC) is thus the expectation value of the x component of the position operator and depends on k_y ,

$$\bar{x}_n(k_y) = \langle 0k_y n | \hat{X} | 0k_y n \rangle. \quad (1.58)$$

From equation (1.39) it follows that the WCC can also be written as

$$\bar{x}_n(k_y) = \frac{i}{2\pi} \int_{-\pi}^{\pi} dk_x \langle u_{n\mathbf{k}} | \partial_{k_x} | u_{n\mathbf{k}} \rangle \quad (1.59)$$

which is the polarisation in x direction, see equation (1.45). Hence, the \mathbb{Z}_2 invariant defined by equation (1.55) can also be written as

$$\nu = \sum_{\alpha} [\bar{x}_{\alpha}^{\text{I}}(\pi) - \bar{x}_{\alpha}^{\text{II}}(\pi)] - \sum_{\alpha} [\bar{x}_{\alpha}^{\text{I}}(0) - \bar{x}_{\alpha}^{\text{II}}(0)] \quad (1.60)$$

where α labels again the Kramers pair and (I,II) the number within a pair, see figure 1.2. Because of Kramers degeneracy, $\bar{x}_{\alpha}^{\text{I}} = \bar{x}_{\alpha}^{\text{II}}$ modulo a lattice constant at $k_y = 0$ and $k_y = \pi$. Therefore, each of the summands in equation (1.60) is an integer. However, to find the correct integer, the branch of $\bar{x}_n(k)$ must not change evolving from $k_y = 0$ to $k_y = \pi$.

The hybrid Wannier functions are not uniquely defined as explained in section 1.5, since the bands still have the freedom of unitary gauge transformations

$$|\tilde{u}_{m\mathbf{k}}\rangle = \sum_n U_{mn}(\mathbf{k}) |u_{n\mathbf{k}}\rangle. \quad (1.61)$$

The desired gauge that makes sure that the correct branches are chosen is the gauge that leads to maximally localised Wannier charge centers, as long as the WCCs evolve smoothly [23]. The maximally localised WCC is defined as the WCC with the minimal total spread [19]

$$\Omega = \sum_n \left[\langle 0k_y n | \hat{X}^2 | 0k_y n \rangle - \langle 0k_y n | \hat{X} | 0k_y n \rangle^2 \right]. \quad (1.62)$$

This condition defines a local gauge where the unitary transformation matrix $U(\mathbf{k})$ can be calculated using the following recipe for each value of k_y [19, 23].

1. Define a discrete mesh of points k_1, \dots, k_N along k_x , see figure 1.3. I used, as recommended by Soluyanov and Vanderbilt, 10 nodes.
2. For all of the discrete points, calculate the eigenvectors $|u_{nk_j}\rangle$.

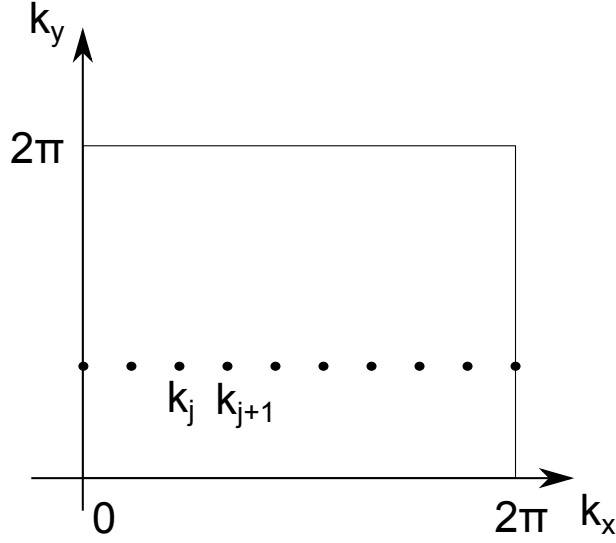


Figure 1.3: Example of an finite k_x mesh for a certain value of k_y . As explained in the text, the local gauge at k_{j+1} is determined from the overlap of the eigenvectors $|u_{\mathbf{k}}\rangle$ with the eigenvectors at the previous node k_j .

3. The eigenstates at the first momentum $k_1 = 0$ are not transformed: $|\tilde{u}_{nk_1}\rangle = |u_{nk_1}\rangle$.
4. To find the correct transformation for the states at momentum k_{j+1} , a singular value decomposition (SVD) of the overlap matrix with the already transformed state at k_j is performed:

$$M_{mn}^{(k_j, k_{j+1})} = \langle \tilde{u}_{mk_j} | u_{nk_{j+1}} \rangle \quad (1.63)$$

$$\text{SVD: } M = V S W^\dagger \quad (1.64)$$

5. The correct transformation is given by

$$U(k_{j+1}) = (W V^\dagger)^T \quad (1.65)$$

$$|\tilde{u}_{mk_{j+1}}\rangle = \sum_n U_{mn}(k_{j+1}) |u_{nk_{j+1}}\rangle \quad (1.66)$$

and has the required property that $M_{mn}^{(k_j, k_{j+1})} = \langle \tilde{u}_{mk_j} | \tilde{u}_{nk_{j+1}} \rangle$, the transformed overlap matrix, is hermitian.

Now, given the correct gauge, it is easy to calculate the WCCs. Because of the periodicity of the lattice, $|\tilde{u}_{m0}\rangle$ and $|\tilde{u}_{m2\pi}\rangle$ are connected by a unitary matrix Λ ,

$$|\tilde{u}_{m2\pi}\rangle = \sum_n \Lambda_{mn} |\tilde{u}_{n0}\rangle. \quad (1.67)$$

The eigenvalues λ_n of Λ have an absolute value of 1 since Λ is unitary. Hence, they can be written as complex phases ϕ_n , i.e. $\lambda_n = e^{-i\phi_n}$. ϕ_n can be seen as a total phase accumulated while evolving $|\tilde{u}_n\rangle$ continuously from $k_x = 0$ to

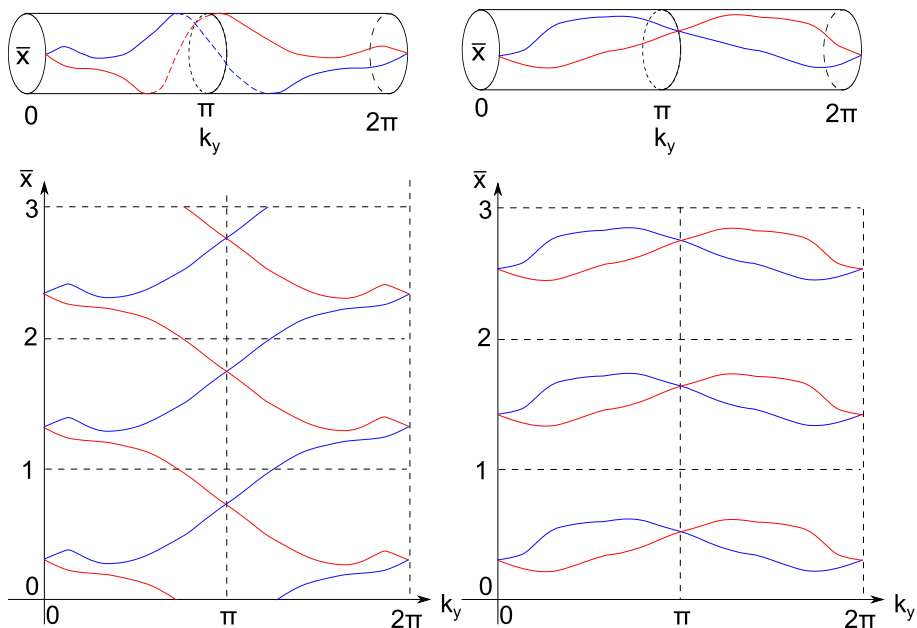


Figure 1.4: Examples for Wannier charge centers of a system with two bands, on the left in the case of a quantum spin Hall state and on the right for a trivial insulator. The two upper pictures show the WCC on a cylinder, the lower uncoiled over three periods.

$k_x = 2\pi$ while k_y remains constant. This phase determines the Wannier charge center \bar{x}_n via the relation [19, 23]

$$\bar{x}_n(k_y) = \phi_n/2\pi = -(\Im \log \lambda_n)/2\pi. \quad (1.68)$$

The topological properties of the band structure are given by the properties of the curves $\bar{x}_n(k_y)$. Let me summarize again the constraints due to time reversal symmetry:

- The WCC is defined modulo the lattice constant a which is set to be 1, since different gauges add a multiple of the lattice constant, see section 1.5.
- Since k_y is periodic with period 2π , $\bar{x}_n(k_y)$ is defined on a torus, see figure 1.4.
- On the torus the WCC are continuous. Uncoiling the torus to a strip one has to be aware that steps of magnitude $a = 1$ can appear which just means that a switch to another branch has happened, see figure 1.4.
- Because of Kramers degeneracy, $\bar{x}_\alpha^I(k_y) = \bar{x}_\alpha^{II}(-k_y)$
- Especially, the two WCC curves belonging to the same Kramers pair intersect at $k_y = 0$ and $k_y = \pi$.
- According to definition (1.60), the Kramers pair α is topologically non-trivial if the WCC curves at $k_y = 0$ and $k_y = \pi$ belong to a different branch, see figure 1.4.

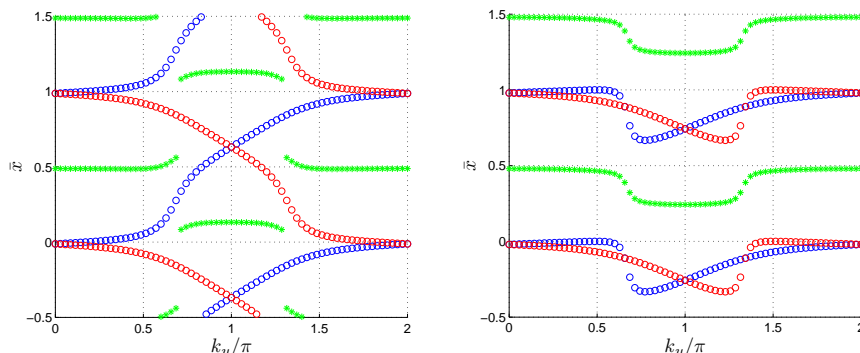


Figure 1.5: Determination of the \mathbb{Z}_2 invariant using Wannier charge centers $\bar{x} = \phi/2\pi$. The red and blue circles, respectively, are the WCC, the green stars are located in the middle of the larger of the two interspaces between the two WCC. In the left picture, one jump of the green curve $z(k_y)$ between 0 and π is larger than $1/4$, hence $\nu = 1$. Here, two periods of \bar{x} are shown.

To sum up, for all Kramers pairs one has to follow the WCC from $k_y = 0$ to $k_y = \pi$ continuously to see if the same branches intersect again. However, following the WCC is not so easy since they have been calculated only at discrete values for k_y . In the case of conserved quantities, for example Spin in z direction, the two WCC within a Kramers pair can easily be labelled, but without there is no other way as to track the WCC.

Soluyanov and Vanderbilt suggested in [23] to follow the maximum interspace between the WCCs instead of the curves itself. In the simplest case of two occupied bands the two WCC divide the torus in two regions. The sum of the two gaps is of course the period 1. In figure 1.5, the larger gap is marked by a green star in the center of the interspaces and is subsequently called $z(k_y)$. The \mathbb{Z}_2 invariant is given by the number of discontinuities of $z(k_y)$ between 0 and π ,

$$\nu = \# \text{ discontinuities of } z(k_y) \text{ in } [0, \pi] \quad \text{mod } 2. \quad (1.69)$$

It is much easier to determine the discontinuities of z than tracking \bar{x} since the jump of z at a discontinuity is for two bands exactly $1/2$, whereas a possible crossing of \bar{x}^I and \bar{x}^{II} needs a much higher resolution. In the following sections, I considered discrete jumps of z larger than $1/4$ as physical jumps which are not due to numerical artefacts. An example is given in figure 1.5.

1.8 Topological invariants for interacting systems

The definition of the Chern number (1.9) is not applicable for interacting systems since Bloch states are used. The first definition for interacting systems was introduced by Niu, Thouless and Wu in 1985 [24] and uses the change of the many body ground state $|\Psi_0\rangle$ as boundary conditions change. Suppose a 2D many body system obeys general boundary conditions defined by phase

shifts ϕ_x, ϕ_y which impose

$$\Psi_0(\dots, \{x_i + n_x L_x, y_i + n_y L_y\}, \dots) = e^{i(n_x \phi_x + n_y \phi_y)} \Psi_0(\dots, \{x_i, y_i\}, \dots).$$

The Chern number of the system is then given by [13, 24]

$$C = \int_0^{2\pi} \int_0^{2\pi} \frac{d\phi_x d\phi_y}{2\pi i} \left(\left\langle \frac{\partial \Psi_0}{\partial \phi_y} \middle| \frac{\partial \Psi_0}{\partial \phi_x} \right\rangle - \left\langle \frac{\partial \Psi_0}{\partial \phi_x} \middle| \frac{\partial \Psi_0}{\partial \phi_y} \right\rangle \right). \quad (1.70)$$

For a \mathbb{Z}_2 invariant or a spin Chern number, the phase shift might be different for spin up and spin down variables. Thus, the Chern number for each combination has to be calculated via [13, 15]

$$C^{\sigma\sigma'} = \int_0^{2\pi} \int_0^{2\pi} \frac{d\phi_x^\sigma d\phi_y^{\sigma'}}{2\pi i} \left(\left\langle \frac{\partial \Psi_0}{\partial \phi_y^{\sigma'}} \middle| \frac{\partial \Psi_0}{\partial \phi_x^\sigma} \right\rangle - \left\langle \frac{\partial \Psi_0}{\partial \phi_x^\sigma} \middle| \frac{\partial \Psi_0}{\partial \phi_y^{\sigma'}} \right\rangle \right). \quad (1.71)$$

The total Chern number is given by $C = \sum_{\sigma\sigma'} C^{\sigma\sigma'}$ and the spin Chern number in analogy to (1.27) by $C = \sum_{\sigma\sigma'} \sigma C^{\sigma\sigma'}$ [13, 15].

In most cases, these expressions are difficult to evaluate. However, information about some quantum mechanical many body system is not only given by the many body ground state, but also by the Green's function. Fortunately, it is possible to reformulate equation (1.70) in terms of the single particle Green's function [24–26]

$$C = \frac{\epsilon^{\mu\nu\rho}}{24\pi^2} \int dk_0 \int d^2k \operatorname{Tr} [G \partial_\mu G^{-1} G \partial_\nu G^{-1} G \partial_\rho G^{-1}] \quad (1.72)$$

where k_0 is the real frequency $k_0 \equiv \omega \in \mathbb{R}$ and $G = G(i\omega, \mathbf{k})$ the Green's function in Matsubara representation. G is a matrix whose indices are the remaining degrees of freedom after translational invariance has been used to transform to momentum space \mathbf{k} , as for example spin and different sites within a unit cell, and G^{-1} denotes the matrix inverse of G . Furthermore, $\partial_\mu \equiv \frac{\partial}{\partial k_\mu}$ and Greek letters are looping from 0 to 3, i.e. $\mu = 0, 1, 2, 3$, where the Einstein convention of implicit summation is used. This formulation using Green's functions gives qualitative information about topology, for example, a change of the topological invariant can only happen if a singularity appears in G or G^{-1} [25, 27]. However, the numerical evaluation of (1.72) is demanding since a good knowledge of the derivatives of the Green's function is necessary to compute the triple integral accurately.

A huge simplification could be achieved by Zhong Wang *et al.* developing a new method where the Green's function is only needed at frequency $\omega = 0$ [28–30]. We can introduce an equation of the Green's function at $\omega = 0$ which reads

$$G^{-1}(\omega = 0, \mathbf{k}) |\alpha(\omega = 0, \mathbf{k})\rangle = \mu_\alpha(\omega = 0, \mathbf{k}) |\alpha(\omega = 0, \mathbf{k})\rangle. \quad (1.73)$$

It is possible to calculate a quantity

$$C_\alpha = \frac{1}{2\pi} \int_{BZ} d^2\mathbf{k} \cdot \mathcal{F}_\alpha(\mathbf{k}) = \frac{1}{2\pi} \oint_{\partial BZ} d\mathbf{k} \cdot \mathcal{A}_\alpha(\mathbf{k}), \quad (1.74)$$

with $\mathcal{F}_\alpha(\mathbf{k}) = \nabla_{\mathbf{k}} \times \mathcal{A}_\alpha(\mathbf{k})$ and $\mathcal{A}_\alpha(\mathbf{k}) = -i \langle \alpha(0, \mathbf{k}) | \nabla_{\mathbf{k}} | \alpha(0, \mathbf{k}) \rangle$, directly from the eigenvectors of G^{-1} . These quantities are Chern numbers and thus integer valued since they have the same structure as the Chern number defined for noninteracting systems (1.9). The difference is that another vector bundle is used: Instead of Bloch states $|u(\mathbf{k})\rangle$ which define the topology of the band Chern numbers through Berry connections $\mathcal{A}_m(\mathbf{k}) = i \langle u_{m\mathbf{k}} | \nabla_{\mathbf{k}} | u_{m\mathbf{k}} \rangle$, eigenfunctions $|\alpha(\mathbf{k})\rangle$ of $G^{-1}(\omega = 0, \mathbf{k})$ define the topology of these different Chern numbers through Berry connections $\mathcal{A}_\alpha(\mathbf{k}) = -i \langle \alpha(0, \mathbf{k}) | \nabla_{\mathbf{k}} | \alpha(0, \mathbf{k}) \rangle$. On the first sight, invariants defined on different bundles may not be connected in any way, but it is the remarkable work of Wang *et al.* to show that summing over all C_α belonging to positive eigenvalues $\mu_\alpha > 0$ (usually called R-space in contrast to L-space which is the space of vectors with negative eigenvalues) gives exactly the same total Chern invariant as defined by (1.72),

$$C = \sum_{\alpha \in \text{R-space}} C_\alpha. \quad (1.75)$$

If the system obeys inversion symmetry, $G^{-1}(\omega, \mathbf{k})$ commutes at the TRIM $\mathbf{k} = \mathbf{\Gamma}_i$ with the parity transformation matrix P (see also section 1.6.1) wherefore $|\alpha(\omega, \mathbf{\Gamma}_i)\rangle$ are simultaneous eigenstates of G and P :

$$P |\alpha(\omega = 0, \mathbf{\Gamma}_i)\rangle = \eta_\alpha |\alpha(\omega = 0, \mathbf{\Gamma}_i)\rangle. \quad (1.76)$$

In [28] it is shown that the topological invariant can be calculated from these eigenvalues through

$$(-1)^\nu = \sum_{\text{R zeros}} \eta_\alpha^{1/2} \quad (1.77)$$

and that it reduces to the Fu-Kane formula (1.56) in the noninteracting case. Here, the convention $(-1)^{1/2} = i$ is used.

To sum up, one can calculate the desired Chern invariant by evaluating Berry phases related to eigenvectors with positive eigenvalues of the inverse Green's function matrix $G^{-1}(\omega = 0, \mathbf{k})$. On the other hand, for noninteracting systems, the Chern invariant is calculated using eigenvectors with negative eigenvalues of a matrix $H(\mathbf{k})$. Hence, the topological properties of an interacting system are the same as for an artificial noninteracting Bloch Hamiltonian which is minus the inverse Green's function at $\omega = 0$. This defines the so called *topological Hamiltonian*

$$H_t(\mathbf{k}) = -G^{-1}(\omega = 0, \mathbf{k}). \quad (1.78)$$

Thus, all topological properties are encoded in an artificial system. Since this is interactionless, all methods described in the previous sections can be used to calculate the Chern invariant. However, it is prudent to mention that only the topological properties are encoded in $H_t(\mathbf{k})$, it is not suitable to use it for estimates of any other quantities.

1.9 Bulk boundary correspondence

A fundamental aspect of finite topological systems is the appearance of gapless states at the boundary, for example 1D states at the edge of a 2D ribbon. The

basic idea behind this correspondence between the topologically nontrivial bulk and the existence of gapless states at the boundary is the stability of topological invariants with respect to minor modifications of the bands. As mentioned in section 1.2, the Chern number can only change if a gap closes and a quantum phase transition happens. A boundary can be seen now as a sharp change of the Hamiltonian from a topologically nontrivial system to the vacuum, which is topologically trivial (the bands are the dispersions of free electrons and positrons as conduction band and valence band, respectively). The change of a topological invariant involves, as mentioned above, a gap closing which has to happen exactly at the boundary.

Such edge states have already been found by Jackiw and Rebbi in 1976 [31] and reappear in the model by Su, Schrieffer and Heeger [32]. The idea from Jackiw and Rebbi of an 1D field theory with edge states is used in the review by Hasan and Kane [7] as an introductory example to bulk boundary correspondence. The model is a Hamiltonian of massive Dirac particles living on a honeycomb lattice (Details on that lattice are explained later in section 2.1). For small momenta around the K points, $\mathbf{q} \equiv \mathbf{k} - \mathbf{K}$ and mass m the Hamiltonian reads

$$H(\mathbf{q}) = \hbar v_F \mathbf{q} \cdot \boldsymbol{\sigma} + m\sigma_z \quad (1.79)$$

and has the energies $E(\mathbf{q}) = \pm \sqrt{|\hbar v_F \mathbf{q}|^2 + m^2}$ with a gap of $2|m|$. If m has a different sign at the two K points K and K' , the system is a topological insulator, otherwise a trivial insulator. Consider now an interface where the sign of m at K' is changing as a function of y as $m(y) = |m| \Theta(y)$ (Θ is the Heaviside step function), but remains positive at K . The Schrödinger equation has then the simple solution

$$\psi_{q_x}(x, y) \propto e^{iq_x x - \int_0^y dy' m(y')/v_F} \begin{pmatrix} 1 \\ 1 \end{pmatrix} \quad (1.80)$$

with the linear dispersion $E(q_x) = \hbar v_F q_x$. Hence, there exists a gapless edge state exponentially localized at the interface.

Analysing the eigenfunctions of a Hamiltonian has been also considered at quantum Hall insulators by Halperin [33] shortly after the experimental discovery of the QH effect even before TKNN published their theoretical description. Halperin's paper is based on the idea of Laughlin, who has shown the quantisation of Hall conductivity by using gauge invariance and a mobility gap [34]. The geometry used by Laughlin is a metal ring pierced by a magnetic field H_0 . Through the ring flows a variable magnetic flux Φ , see figure 1.6. The Hamiltonian of that system with charge carriers of mass m^* is

$$H = \frac{\hbar^2}{2m^*} \left(\mathbf{P} - \frac{e}{c} \mathbf{A} \right)^2 + eE_0 y. \quad (1.81)$$

With a Landau gauge for the magnetic field $\mathbf{A} = H_0 y \hat{x}$ the Landau levels $E_n = (n + \frac{1}{2}) \hbar \omega_c$ with the cyclotron frequency $\omega_c = |eB_0|/m^*c$ can be proven. In his gedankenexperiment, Laughlin changed the vector potential to $\mathbf{A} \rightarrow \mathbf{A} + A_0 \hat{x}$ which physically means turning on a magnetic flux $\Phi = A_0 L_x$ through the loop

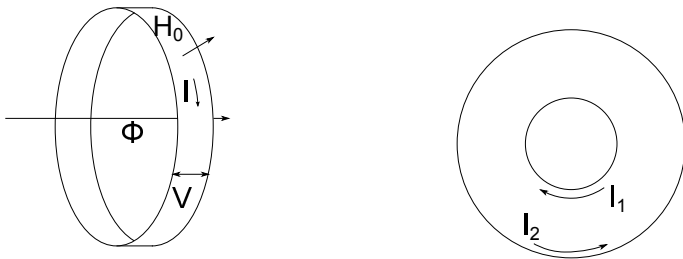


Figure 1.6: The left picture shows the geometry of the Laughlin gedankenexperiment, the right picture the modified version from Halperin.

which causes a current in y direction given by

$$I = \frac{c}{L_x} \frac{\partial \langle H \rangle}{\partial A_0} = c \frac{\partial \langle H \rangle}{\partial \Phi}. \quad (1.82)$$

This relation can be proven directly from Hamiltonian (1.81). A detailed derivation is given in Laughlin's Nobel lecture [35]. The idea of this loop geometry is now that increasing Φ by a flux quantum $\Delta\Phi = hc/e$ maps the system back to itself since it is a legit gauge transformation. This means that the energy levels have to be the same as before, but the population of each level may change. Laughlin showed that n electrons are shifted from the left to the right of the sample which gives the correct Hall current calculated from (1.82)

$$I = n \frac{e^2}{h} V. \quad (1.83)$$

Halperin modified the model to a flat geometry, see figure 1.6. He considered a vector potential in azimuthal direction with magnitude

$$A = \frac{1}{2} B_0 r + \frac{\Phi}{2\pi r} \quad (1.84)$$

and looked at the eigenstates, which are due to the Landau levels proportional to harmonic oscillators

$$\psi_{m\nu}(r, \theta) \propto e^{im\theta} f_\nu(r - r_m). \quad (1.85)$$

Here, f_ν are the eigenfunctions of a harmonic oscillator. They are centered at r_m and have a spread which is in the order of magnitude of the cyclotron radius r_c . However, because of boundary conditions, this structure of the eigenstates is only true if $r_1 < r_m < r_2$ and $r_m - r_1$ and $r_2 - r_m$ are large compared to r_c . Halperin looked more closely to these eigenstates and concluded [33] that the eigenstates of structure (1.85) do not contribute to a current. In fact, all the current density is nonzero only in a region of $\approx r_c$ near the edge. If no voltage is applied, the currents at the two edges cancel to give a zero net current $I_1 = -I_2$. If a voltage is applied, the Fermi levels $E_F^{(1)}$ and $E_F^{(2)}$ are different and give a net current $I_{\text{edges}} = (E_F^{(2)} - E_F^{(1)}) ne/h$ carried by the edge states.

These examples of a field theory with massive Dirac particles and the considerations of a Quantum Hall system are strong indications for the assumption

stated at the beginning of this section that a surface or an interface between two materials with different topological properties accompanies edge states. For many systems, rigorous proofs exist. Essin and Gurarie have shown in [27] that the existence of edge states follows from the a nonzero topological invariant given in terms of Green's functions (see equation (1.72)). This approach is very general and valid for all 10 topological classes in all dimensions and uses the fact that a Chern integer defined by (1.72) can only change if the Green's function has a pole or a zero. The proof presumes that no Green's function zeros appear, which is true if the system is noninteracting. For interacting systems, Green's function zeros can appear and hence it is in principle possible that no edge states are at an interface between two interacting topological insulators, which hence can be continuously deformed from one to another without ever closing the bulk gap [25]. The Chern number in terms of Green's functions (1.72) is designed such that it adiabatically connected to Chern numbers of noninteracting systems calculated from Bloch functions. It thus has the right properties in the limit of vanishing interaction, but its meaning for strongly interacting systems is still not clear [13].

Another interesting proof is from Schulz-Baldes [36] who has shown for 2D systems with time-reversal symmetry breaking terms, as for example Rashba spin-orbit, that the spin edge currents persist provided there is a spectral gap and the spin Chern numbers (1.27) are nontrivial. Graf and Porta [37], on the other hand, give a new definition of the \mathbb{Z}_2 invariant for both bulk and edge and show that these are equivalent.

Chapter 2

The Kane-Mele model

2.1 Graphene

In nature, carbon appears in two different crystal structures. One is diamond, which is due to the fcc lattice with two atoms per primitive unit cell a very hard insulating material. The second is graphite, where two-dimensional sheets with hexagonal symmetry are stacked onto each other. In contrast to diamond, graphite is conducting, opaque (black) and very soft. Graphene is the name of the two-dimensional material which consists of exactly one sheet of graphite. This material is stable and has been experimentally realized by Novoselov *et al.* in 2004 [38].

The crystal structure is hexagonal with two atoms per unit cell (called sublattices A and B , respectively) and is usually called *honeycomb lattice*, see figure 2.1. Since there are several ways to define the orientation, the reference length and the unit cell, I will define here all relevant quantities which are used later in this thesis. The hexagon is oriented such that corners with sites of type A point in negative y direction and opposing corners with B sites in positive. The lattice vectors are called \mathbf{a}_1 and \mathbf{a}_2 , respectively, and their length is the lattice parameter a which is set to be 1 throughout this thesis, but it is kept as a parameter in this section for completeness. As shown in figure 2.1, the numerical values of the lattice vectors are

$$\mathbf{a}_1 = \frac{a}{2} \begin{pmatrix} 1 \\ \sqrt{3} \end{pmatrix} \quad \mathbf{a}_2 = \frac{a}{2} \begin{pmatrix} -1 \\ \sqrt{3} \end{pmatrix}. \quad (2.1)$$

The nearest-neighbor distance is $\delta = a/\sqrt{3}$ and the corresponding vectors δ_i are defined to point from sites A to sites B :

$$\delta_1 = \frac{a}{\sqrt{3}} \begin{pmatrix} 0 \\ -1 \end{pmatrix} \quad \delta_2 = \frac{a}{2\sqrt{3}} \begin{pmatrix} \sqrt{3} \\ 1 \end{pmatrix} \quad \delta_3 = \frac{a}{2\sqrt{3}} \begin{pmatrix} -\sqrt{3} \\ 1 \end{pmatrix}. \quad (2.2)$$

In the case of graphene, $a = 2.46 \pm 0.02 \text{ \AA}$ and hence $\delta \approx 1.42 \text{ \AA}$ [39]. The basis vectors (2.1) determine the reciprocal lattice vectors

$$\mathbf{b}_1 = \frac{2\pi}{a\sqrt{3}} \begin{pmatrix} -\sqrt{3} \\ 1 \end{pmatrix} \quad \mathbf{b}_2 = \frac{2\pi}{a\sqrt{3}} \begin{pmatrix} \sqrt{3} \\ 1 \end{pmatrix}. \quad (2.3)$$

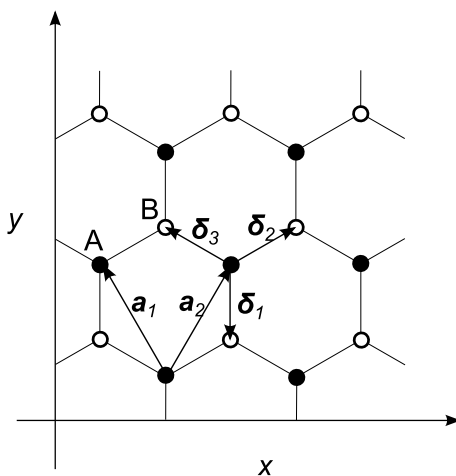


Figure 2.1: Honeycomb lattice in real space. Full circles represent sublattice A , empty circles sublattice B . The primitive lattice vectors \mathbf{a}_i are defined in equation (2.1), the nearest-neighbor vectors δ_i in equation (2.2).

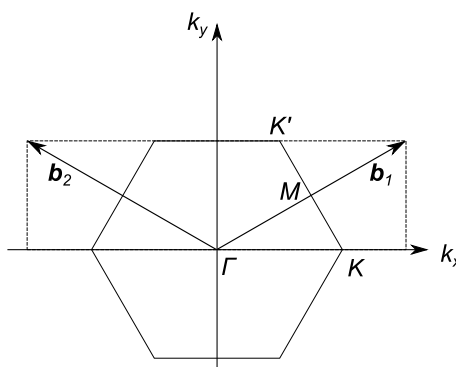


Figure 2.2: Brillouin zone and reciprocal lattice vectors of the honeycomb lattice.

The first Brillouin zone is hexagonal and shown in figure 2.2. Special points are Γ , K , K' and M ,

$$\mathbf{\Gamma} = \begin{pmatrix} 0 \\ 0 \end{pmatrix} \quad \mathbf{K} = \frac{2\pi}{3a} \begin{pmatrix} -1 \\ \sqrt{3} \end{pmatrix} \quad \mathbf{K}' = \frac{2\pi}{3a} \begin{pmatrix} 1 \\ \sqrt{3} \end{pmatrix} \quad \mathbf{M} = \frac{2\pi}{a\sqrt{3}} \begin{pmatrix} 0 \\ 1 \end{pmatrix}. \quad (2.4)$$

Their location in the Brillouin zone is shown in figure 2.2.

The easiest model for graphene is a nearest-neighbor tight-binding model so that hopping to another site gains energy t . The corresponding Hamiltonian in second quantisation is

$$H = -t \sum_{\langle i,j \rangle \sigma} c_{i\sigma}^\dagger c_{j\sigma}. \quad (2.5)$$

The energy levels can be easily found by transforming to momentum space, as

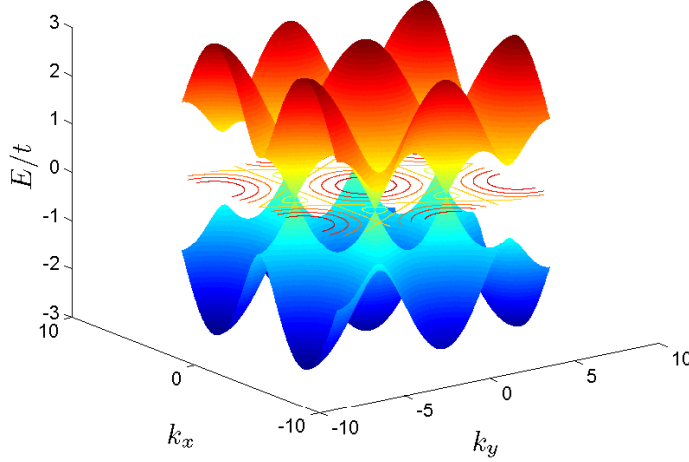


Figure 2.3: Energy bands of the nearest-neighbor tight-binding model on the honeycomb lattice. The Dirac cones touch at the corners of the Brillouin zone called K and K' , see figure 2.2.

shown in appendix A.1. The resulting dispersion relation with $a = 1$ is [40, 41]

$$E(\mathbf{k}) = \pm |g(\mathbf{k})| = \pm t \sqrt{1 + 4 \cos\left(\frac{k_x}{2}\right) \cos\left(\frac{\sqrt{3}k_y}{2}\right) + 4 \cos^2\left(\frac{k_x}{2}\right)}. \quad (2.6)$$

As shown in figure 2.3, the dispersion is linear around K and K' . Expanding the momentum around the K points $\mathbf{k} = \mathbf{K} + \mathbf{q}$, the energies of these so called *Dirac cones* are [41]

$$E(\mathbf{q}) = \pm v_F |\mathbf{q}| + \mathcal{O}[(q/K)^2] \quad (2.7)$$

with the Fermi velocity $v_F = -\frac{3}{2}t$. Hence, around the K points, the Hamiltonian can be written effectively as the Dirac Hamiltonian of a massless particle

$$H_{\text{eff}}(\mathbf{q}) = v_F \boldsymbol{\sigma} \cdot \mathbf{q}. \quad (2.8)$$

Comparing to experimental data, a much better result is achieved if a hopping to second nearest-neighbors is considered as well. The Hamiltonian has then the form

$$H = -t \sum_{\langle i,j \rangle \sigma} c_{i\sigma}^\dagger c_{j\sigma} - t' \sum_{\langle\langle i,j \rangle\rangle \sigma} c_{i\sigma}^\dagger c_{j\sigma}. \quad (2.9)$$

The energies change to [40, 41]

$$E(\mathbf{k}) = \pm |g(\mathbf{k})| - t' \left[4 \cos\left(\frac{k_x}{2}\right) \cos\left(\frac{\sqrt{3}k_y}{2}\right) + 4 \cos^2\left(\frac{k_x}{2}\right) - 2 \right], \quad (2.10)$$

with $g(\mathbf{k})$ the same as in equation (2.1). The second nearest-neighbor hopping breaks particle hole symmetry, but near the K points it causes, up to order q^2 , just a constant shift in Energy. This means that the Dirac cones, which only consider linear order in q , remain the same with a Fermi velocity $v_F = -\frac{3}{2}t$.

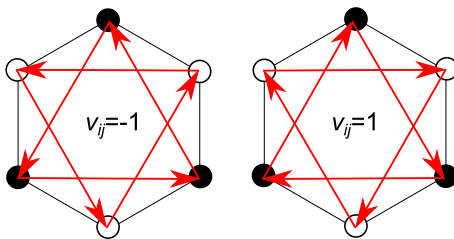


Figure 2.4: Illustration of the sign of ν_{ij} . The left picture shows all left turns to next-nearest-neighbors within a hexagon with $\nu_{ij} = -1$, the right picture all right turns with $\nu_{ij} = 1$.

2.2 Haldane model

Haldane considered in [42] a model of spinless fermions aiming at a nonzero quantum Hall conductance σ_{xy} in the absence of an external magnetic field. The Hamiltonian is defined on a honeycomb lattice and is identical to the next-nearest-neighbor tight-binding model for graphene (2.9), but with the generalisation that the next-nearest-neighbor hopping is modified by a site dependent phase $e^{i\nu_{ij}\phi}$. Here, $\nu_{ij} \equiv \text{sgn}(\mathbf{d}_{ik} \times \mathbf{d}_{kj})_z = \pm 1$ where \mathbf{d}_{ik} is the vector pointing from site i to its nearest-neighbor site k and is hence equal to $\pm\delta_i$ defined in (2.2). This means that the phase is $+\phi$ if the electron makes a left turn while travelling to the next-nearest-neighbor and $-\phi$ in the case of a right turn, see figure 2.4. Furthermore, Haldane considered an energy difference between the sublattices A and B , controlled by a parameter M . The total Hamiltonian is

$$H_{\text{Haldane}} = -t \sum_{\langle i,j \rangle} c_i^\dagger c_j - t' \sum_{\langle\langle i,j \rangle\rangle} e^{i\nu_{ij}\phi} c_i^\dagger c_j + M \sum_i \xi_i c_i^\dagger c_i, \quad (2.11)$$

where $\xi_i = 1$ for $i \in A$ and $\xi_i = -1$ for $i \in B$.

Although looking pretty similar to the graphene model (2.9), fundamental differences arise due to the complex phase. If $\phi \neq 0$ and $\phi \neq \pi$, time reversal symmetry is broken, which is necessary for the Chern invariant to be nontrivial. Furthermore, if $M \neq 0$ the inversion symmetry is broken. In contrast to graphene, the energy bands are gapped. As presented in [42], the gap closes in the case of $M = \pm 3\sqrt{3}t_2 \sin \phi$. The interesting property of this Hamiltonian is that the Chern number changes with the parameters. The only case, where C is easy to evaluate, is the time reversal invariant with $\phi = 0$ or π since there it is known that $C = 0$ (see section 1.2). In the case of a nontrivial ϕ it is easier to calculate changes in the Chern number rather than the Chern number itself. In [42] it is shown that the Chern number changes when the band gap closes at the K points, namely $\Delta C = 1$ if M is increased over $3\sqrt{3}t_2 \sin \phi$ and $\Delta C = -1$ if M is increased over $-3\sqrt{3}t_2 \sin \phi$. Together with $C = 0$ for $\phi = 0$, the phase diagram is completely determined (see figure 2.5) [42, 43].

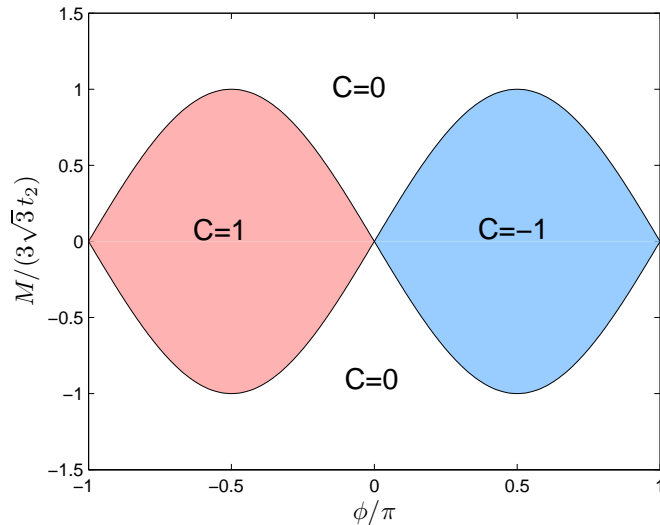


Figure 2.5: Phase diagram of the Haldane model. The Chern invariant C is shown as a function of the next-nearest-neighbor phase shift ϕ and the energy difference between the sublattices.

2.3 Kane-Mele model

In 2005, two remarkable papers [12,44] by Kane and Mele were published which set the starting point of the wide field of topological insulators. Their model consists of electrons on a honeycomb lattice including, along a nearest-neighbor tight-binding term, at least a spin-orbit interaction. This term causes a sign difference between spin up and spin down electrons in the Hamiltonian. Hence, to avoid expressions with several spin indices, a spinor notation $c^\dagger \equiv (c_\uparrow^\dagger, c_\downarrow^\dagger)$ is conveniently used. In some papers or reviews, an additional mark like a hat (for example in [13]) or a tilde are used to distinguish a spinor operator from a one particle operator but I will stick to the original notation [12] that a creation or annihilation operator in a spinful system always denotes the spinor if no explicit spin index is added. The total Kane-Mele Hamiltonian is

$$\begin{aligned}
 H_{\text{KM}} = & -t \sum_{\langle i,j \rangle} c_i^\dagger c_j + i\lambda_{\text{SO}} \sum_{\langle\langle i,j \rangle\rangle} \nu_{ij} c_i^\dagger \sigma^z c_j \\
 & + i\lambda_{\text{R}} \sum_{\langle i,j \rangle} c_i^\dagger (\boldsymbol{\sigma} \times \hat{\mathbf{d}}_{ij})_z c_j + \lambda_{\nu} \sum_i \xi_i c_i^\dagger c_j.
 \end{aligned} \tag{2.12}$$

The first term is the tight-binding term which already appears in the graphene and the Haldane model. The second is a spin-orbit interaction. It is a next-nearest-neighbor hopping that depends on spin (additional minus sign for \downarrow due to σ_z) and on the hopping, $\nu_{ij} \equiv \text{sgn}(\mathbf{d}_{ik} \times \mathbf{d}_{jk})_z = \pm 1$ is defined as in the case of the Haldane model, see figure 2.4. Comparing with the next-nearest-neighbor hopping term of the Haldane model, one sees that the spin-orbit interaction corresponds to $\phi = -\pi/2$ for spin up electrons and to $\phi = \pi/2$ for spin down electrons. The third term is a nearest-neighbor Rashba interaction. $\boldsymbol{\sigma}$ denotes

here the vector of Pauli matrices $\boldsymbol{\sigma} = (\sigma_x, \sigma_y, \sigma_z)$ and $\hat{\mathbf{d}}_{ij}$ the unit vector of the nearest-neighbor vector \mathbf{d}_{ij} pointing from site i to site j . This term breaks the $z \mapsto -z$ mirror symmetry and hence the spin in z direction S_z is no longer conserved. The last term is, as in the Haldane model, a sublattice potential causing due to $\xi_i = \pm 1$ an energy difference between A and B sites.

To sum up, the only term that did not appear already in the Haldane model is the Rashba coupling, wherefore the Kane-Mele Hamiltonian with $\lambda_R = 0$ can be written as a sum of Haldane models [43]

$$H_{\text{KM}}(\lambda_R = 0) = H_{\text{Haldane}}^\uparrow(\phi = -\pi/2) + H_{\text{Haldane}}^\downarrow(\phi = \pi/2). \quad (2.13)$$

The corresponding parameters of the Haldane model (2.13) are $t' = \lambda_{\text{SO}}$ and $M = \lambda_\nu$. The Kane-Mele Hamiltonian is, in contrast to the Haldane Hamiltonian, time reversal invariant, which has the direct consequence that the Chern number is zero. In other words, Hall conductivity violates \mathcal{T} symmetry and must therefore vanish. However, the Chern invariant for each spin is for $|\lambda_\nu| < 3\sqrt{3}|t|$ nontrivial (see figure 2.5).

$$C^\uparrow = C \left[H_{\text{Haldane}}^\uparrow(\phi = -\pi/2) \right] = 1 \quad (2.14)$$

$$C^\downarrow = C \left[H_{\text{Haldane}}^\downarrow(\phi = \pi/2) \right] = -1 \quad (2.15)$$

$$C = C^\uparrow + C^\downarrow = 0 \quad (2.16)$$

$$C^s = (C^\uparrow - C^\downarrow)/2 = 1 \quad (2.17)$$

$$\nu = C^s \pmod{2} = 1 \quad (2.18)$$

In a historical view, it was this model with its structure of two opposing quantum Hall systems that induced Kane and Mele to define a \mathbb{Z}_2 invariant.

2.3.1 Bloch Hamiltonian

From the Haldane model it is already known that that the topological structure will break down at $\lambda_\nu = 3\sqrt{3}\lambda_{\text{SO}}$ (see figure 2.5) as mentioned without complete proof in section 2.2. Considering the full Kane-Mele model, this section is aiming to describe the properties of the Bloch Hamiltonian in order to discuss rigorously the topological properties.

The eigenenergies of H_{KM} can be evaluated, as usual for tight-binding systems, by using the translational symmetry of the lattice. Hence, a Fourier transformation from real space coordinates \mathbf{R}_i with lattice indices i to momentum \mathbf{k} leads to a block diagonal structure. Next to \mathbf{k} , the remaining degrees of freedom are the two sublattices and the spin. The basis used here is, like in [13], $\Psi_{\mathbf{k}}^\dagger = (a_{\mathbf{k}\uparrow}^\dagger, b_{\mathbf{k}\uparrow}^\dagger, a_{\mathbf{k}\downarrow}^\dagger, b_{\mathbf{k}\downarrow}^\dagger)$. In this basis, the Hamiltonian is of the form

$$H_{\text{KM}} = \sum_{\mathbf{k}} \Psi_{\mathbf{k}}^\dagger H(\mathbf{k}) \Psi_{\mathbf{k}}. \quad (2.19)$$

The Bloch Hamilton matrix is, as shown in appendix A.1,

$$H(\mathbf{k}) = \begin{pmatrix} \gamma_{\mathbf{k}} + \lambda_{\nu} & -g_{\mathbf{k}} & 0 & \rho_{\mathbf{k}} \\ -g_{\mathbf{k}}^* & -\gamma_{\mathbf{k}} - \lambda_{\nu} & -\rho_{-\mathbf{k}} & 0 \\ 0 & -\rho_{-\mathbf{k}}^* & -\gamma_{\mathbf{k}} + \lambda_{\nu} & -g_{\mathbf{k}} \\ \rho_{\mathbf{k}}^* & 0 & -g_{\mathbf{k}}^* & \gamma_{\mathbf{k}} - \lambda_{\nu} \end{pmatrix} \quad (2.20)$$

with

$$g_{\mathbf{k}} = t \left[e^{-i\frac{k_y}{\sqrt{3}}} + 2e^{i\frac{k_y}{2\sqrt{3}}} \cos\left(\frac{k_x}{2}\right) \right] \quad (2.21)$$

$$\gamma_{\mathbf{k}} = 2\lambda_{\text{SO}} \left[2 \sin\left(\frac{k_x}{2}\right) \cos\left(\frac{\sqrt{3}k_y}{2}\right) - \sin(k_x) \right] \quad (2.22)$$

$$\rho_{\mathbf{k}} = i\lambda_{\text{R}} \left[-e^{-i\frac{k_y}{\sqrt{3}}} + e^{i\frac{k_y}{2\sqrt{3}}} \left(\cos\left(\frac{k_x}{2}\right) - \sqrt{3} \sin\left(\frac{k_x}{2}\right) \right) \right]. \quad (2.23)$$

To analyse the behaviour of $H(\mathbf{k})$ under certain transformations, it is helpful to expand the matrix in terms of Dirac matrices [12]. The vector space of 4×4 matrices is 16 dimensional and a proper basis consists of the identity $\Gamma^0 \equiv \mathbb{1}$, five Dirac matrices Γ^a and their 10 commutators $\Gamma^{ab} = [\Gamma^a, \Gamma^b]/(2i)$. The Bloch Hamiltonian can be written as

$$H(\mathbf{k}) = \sum_{a=0}^5 d_a(\mathbf{k})\Gamma^a + \sum_{a<b=1}^5 d_{ab}(\mathbf{k})\Gamma^{ab} \quad (2.24)$$

There are many ways to define the Γ^a , the definition from [12] is used here: $\Gamma^{(1,2,3,4,5)} = (\mathbb{1} \otimes \sigma^x, \mathbb{1} \otimes \sigma^z, \sigma^x \otimes \sigma^y, \sigma^y \otimes \sigma^y, \sigma^z \otimes \sigma^y)$. The first matrix is related to spin, the second to the sublattice (Hilbertspace = spin \otimes sublattice) to be consistent with matrix representation (2.20). Note that in [12] the definition is contrary (Hilbertspace = sublattice \otimes spin) what gives the same expansion (2.24), but another matrix representation of $H(\mathbf{k})$ which is a rearrangement of the elements of (2.20). The reason for the definition of Γ^a used here and in [12] is that Γ^a are even under time reversal $\Theta\Gamma^a\Theta^{-1} = \Gamma^a$ while Γ^{ab} are odd $\Theta\Gamma^{ab}\Theta^{-1} = -\Gamma^{ab}$. Within this representation, the non vanishing coefficients $d(\mathbf{k})$ in equation (2.24) are [12]

$$\begin{aligned} d_1 &= -\Re(g_{\mathbf{k}}) = -t(1 + 2 \cos x \cos y) \\ d_2 &= \lambda_{\nu} \\ d_3 &= \lambda_{\text{R}}(1 - \cos x \cos y) \\ d_4 &= -\sqrt{3}\lambda_{\text{R}} \sin x \sin y \\ d_{12} &= -\Im(g_{\mathbf{k}}) = 2t \cos x \sin y \\ d_{15} &= \gamma_{\mathbf{k}} = 2\lambda_{\text{SO}}(2 \sin x \cos y - \sin 2x) \\ d_{23} &= -\lambda_{\text{R}} \cos x \sin y \\ d_{24} &= \lambda_{\text{R}} \sin x \cos y \end{aligned} \quad (2.25)$$

with $x \equiv k_x/2$ and $y \equiv k_y\sqrt{3}/2$. The time reversal invariance of $H(\mathbf{k})$ can be proven easily: Since Γ^a is even and Γ^{ab} odd under \mathcal{T} , and furthermore $d(\mathbf{k})$ fulfil $d_a(\mathbf{k}) = d_a(-\mathbf{k})$ and $d_{ab}(\mathbf{k}) = -d_{ab}(-\mathbf{k})$, it follows from (2.24) that $\Theta H(\mathbf{k})\Theta^{-1} = H(-\mathbf{k})$.

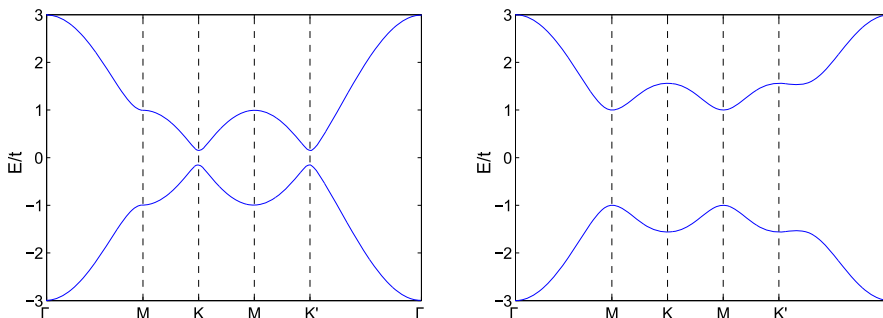


Figure 2.6: Bands of the Kane-Mele Model with $\lambda_\nu = \lambda_R = 0$. The left picture shows bands for $\lambda_{SO} = 0.03t$. The smallest gap is at K and K' with a gap size of $\Delta = 3\sqrt{3}\lambda_{SO}$. In the right picture, $\lambda_{SO} = 0.3t$ where the smallest gap is now at M with $\Delta = 2t$.

2.3.2 Topology in inversion symmetric case

In the simple inversion symmetric case of $\lambda_\nu = \lambda_R = 0$, matrix (2.20) is decomposed into two, up to a factor of -1 in the diagonal, identical matrices. These are related to spin up and spin down, respectively. Hence, the energy bands

$$E_\pm(\mathbf{k}) = \pm\sqrt{|g\mathbf{k}|^2 + \gamma_{\mathbf{k}}^2} \quad (2.26)$$

are two fold degenerate, which can be seen as an interplay of inversion symmetry together with \mathcal{T} symmetry which causes Kramers degeneracy. The most important qualitative change in comparison with bare tight-binding models is the appearance of a gap at the K points of size

$$\Delta_K = 2\gamma_K = 6\sqrt{3}\lambda_{SO}. \quad (2.27)$$

For large spin-orbit couplings $\lambda_{SO}/t > 1/(3\sqrt{3}) \approx 0.19$, the minimal gap is at the M point and is of size $\Delta = 2t$ [13]. The bands for $\lambda_{SO} = 0.03t$ and $\lambda_{SO} = 0.3t$ are shown in figure 2.6.

From the relation to the Haldane model (2.13) it is known that the spin Chern number is 1 (see eq. (2.17)) and that the \mathbb{Z}_2 invariant defined by $C_s \bmod 2$ (1.28) is nontrivial. Since spin in z direction is conserved because of $\lambda_R = 0$, the definition of ν is identical to the definition introduced by Fu and Kane (1.53). For the latter definition, it is easier to calculate ν directly using equation (1.56), than calculating the changes of Chern invariants as done for the Haldane system in section 2.2. This has been already done in the paper where the method is presented [22]. The time reversal invariant momenta Γ_i of the honeycomb lattice are Γ and three M points, see figure 2.7:

$$\begin{aligned} \Gamma_1 = \Gamma &= \begin{pmatrix} 0 \\ 0 \end{pmatrix} & \Gamma_2 = M_1 &= \frac{2\pi}{a\sqrt{3}} \begin{pmatrix} \sqrt{3} \\ 1 \end{pmatrix} \\ \Gamma_3 = M_2 &= \frac{2\pi}{a\sqrt{3}} \begin{pmatrix} -\sqrt{3} \\ 1 \end{pmatrix} & \Gamma_4 = M_3 &= \frac{2\pi}{\sqrt{3}} \begin{pmatrix} 0 \\ 1 \end{pmatrix} \end{aligned} \quad (2.28)$$

To calculate the topological invariant, the eigenvalues of the inversion operator at these momenta are needed. This problem can be simplified using the

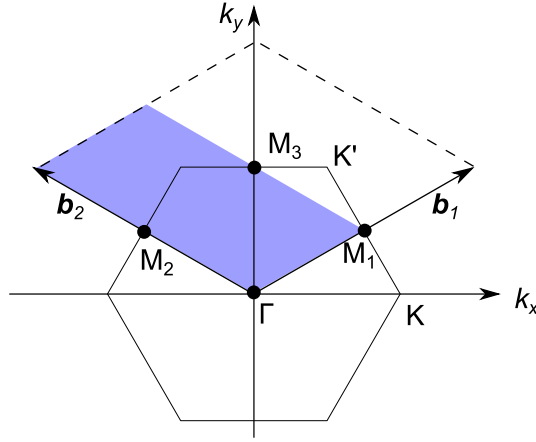


Figure 2.7: Topologically relevant points of the honeycomb lattice in reciprocal space. The four TRIM (Γ and three M points) are marked as circles. The blue area shows the region used to calculate $\bar{x}(k_2)$.

fact that inversion symmetry (matrix representation: $P = \mathbb{K} \otimes \sigma^x = \Gamma^1$) is assumed. For time reversal invariant Hamiltonians which additionally obey inversion symmetry, $P\Theta H(\mathbf{k})\Theta^{-1}P^{-1} = PH(-\mathbf{k})P^{-1} = H(\mathbf{k})$ holds. Since only $\Gamma^1, \Gamma^{12}, \Gamma^{13}, \Gamma^{14}, \Gamma^{15}$ are even under \mathcal{PT} while the other basis matrices are odd, equation 2.24 simplifies to

$$H(\mathbf{k}) = d_0(\mathbf{k})\mathbb{K} + d_1(\mathbf{k})\Gamma^1 + \sum_{b=2}^5 d_{1b}(\mathbf{k})\Gamma^{1b}. \quad (2.29)$$

At the time reversal invariant momenta (TRIM), $H(\Gamma_i) = H(-\Gamma_i)$. Hence, in addition to the constraint that H is even under \mathcal{PT} it must be even under both \mathcal{P} and \mathcal{T} . This is only true for $\Gamma^1 = P$, wherefore the Bloch Hamiltonian of inversion symmetric systems has at the TRIM the form

$$H(\mathbf{k} = \Gamma_i) = d_0(\mathbf{k} = \Gamma_i)\mathbb{K} + d_1(\mathbf{k} = \Gamma_i)P. \quad (2.30)$$

Because of this simple structure, the eigenvalues of P are related to the eigenvalues of H . The coefficients δ_i defined in section 1.6.1 are given by [22]

$$\delta_i = -\text{sgn}(d_1(\mathbf{k} = \Gamma_i)). \quad (2.31)$$

Inserting the TRIM (2.28) in d_1 (2.25), the results are $\delta_1 = -1$, $\delta_2 = 1$, $\delta_3 = -1$, $\delta_4 = -1$, and hence

$$\prod_{i=1}^4 \delta_i = (-1)^1 \Rightarrow \nu = 1. \quad (2.32)$$

Interestingly, only d_1 , a term originating from the tight-binding term, has an impact on the result. The spin-orbit term seems to have no influence, since it is odd under \mathcal{P} . However, the term is needed to gap the system because only for insulators the description above is valid.

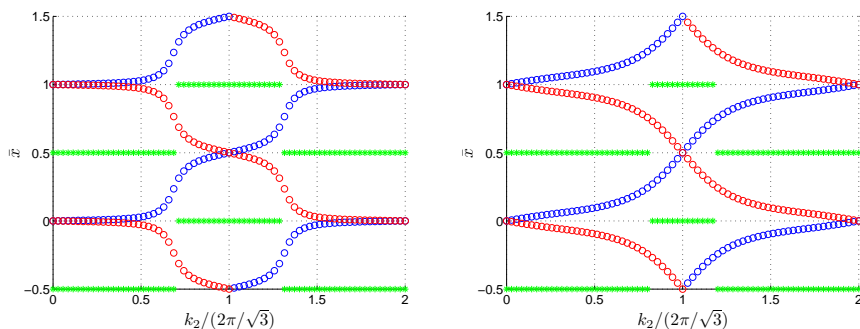


Figure 2.8: Wannier charge centers of the inversion symmetric Kane-Mele model. The spin-orbit coupling is $\lambda_{\text{SO}} = 0.03t$ in the left figure and $\lambda_{\text{SO}} = 0.3t$ in the right. Blue and red circles denote $\bar{x}_{\uparrow}(k_2)$ and $\bar{x}_{\downarrow}(k_2)$, respectively. Since the maximum interval curve $z(k_2)$ shown in green jumps once between 0 and $2\pi/\sqrt{3}$, we have $\nu = 1$ in both cases.

2.3.3 Topology in general case

The approach of the last section is only suitable for the inversion symmetric case, i.e. $\lambda_{\nu} = \lambda_{\text{R}} = 0$. In the general case, the Soluyanov-Vanderbilt method can be used. This method is explained in section 1.7, but with the restriction that a rectangular lattice is assumed. It can be easily adopted by using the non-orthogonal basis of the reciprocal lattice $\mathbf{k} = k_1\hat{\mathbf{b}}_1 + k_2\hat{\mathbf{b}}_2$ instead of Cartesian coordinates $\mathbf{k} = k_x\hat{\mathbf{x}} + k_y\hat{\mathbf{y}}$. The hybrid Wannier transformation is performed along k_1 to give Wannier Charge centers as a function of k_2 . The half Brillouin zone used to calculate $\bar{x}(k_2)$ is shown in figure 2.7 as a bluish shaded region. The quantity k_2 used as abscissa variable has a periodicity of $4\pi/\sqrt{3}$ since this is the length of the reciprocal lattice vector \mathbf{b}_2 .

In the following, the hopping t defining the energy scale is set to be one in order to keep a clear focus on the interplay of the other parameters λ_{SO} , λ_{ν} and λ_{R} . This is equivalent to a rescaling $\lambda_i \rightarrow \lambda_i/t$. The Wannier charge centers (WCC) belonging to the bands shown in figure 2.6 ($\lambda_{\text{SO}} = 0.03$ and 0.3 , $\lambda_{\nu} = \lambda_{\text{R}} = 0$) are shown in figure 2.8. Since $\lambda_{\text{R}} = 0$, the spin in z direction is conserved, wherefore the individual WCC can be traced. \bar{x}_{I} is defined to the WCC of spin up states and colored blue, \bar{x}_{II} the WCC of spin down and colored red. In figure 2.8, one can directly read off the topological quantities that had been determined for the Haldane model in equation (2.14). $\bar{x}_{\text{I}}(4\pi/\sqrt{3}) - \bar{x}_{\text{I}}(0) = 1$, hence $C^{\uparrow} = 1$. In analogy, $C^{\downarrow} = -1$. The \mathbb{Z}_2 invariant ν has been calculated using the definition $\nu = C^{\text{s}} \bmod 2$, but using the Soluyanov-Vanderbilt approach of counting the discontinuities of the maximum interval curve $z(k_2)$ (see section 1.7 and equation (1.60) in particular) it can also be determined in the sense of Fu and Kane (1.53). Once again, it should be mentioned that for S_z conserving Hamiltonians that obey \mathcal{T} symmetry the two ways to define ν are identical.

One symmetry of these curves is $\bar{x}_{\text{I}}(k_2) = \bar{x}_{\text{II}}(-k_2)$ which is a direct consequence of Kramers degeneracy due to time reversal symmetry. Another symmetry is $\bar{x}_{\text{I}}(k_2) = -\bar{x}_{\text{II}}(k_2)$ which is caused by the degeneracy of the bands due

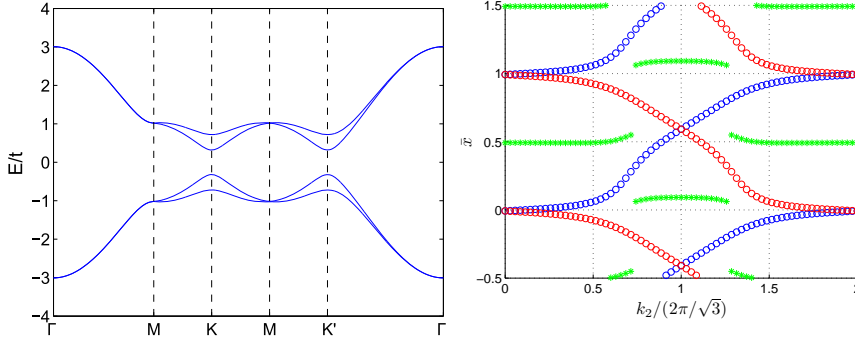


Figure 2.9: The left picture shows the bands, the right picture the Wannier charge center of the Kane-Mele model with $\lambda_{\text{SO}} = 0.1 t$, $\lambda_{\nu} = 0.2 t$ and $\lambda_{\text{R}} = 0$.

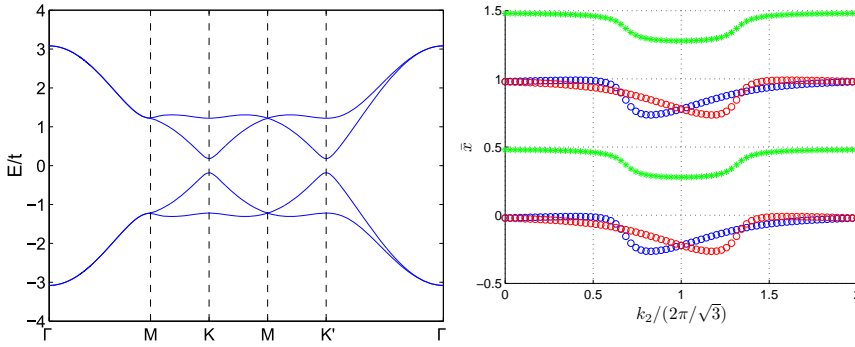


Figure 2.10: The left picture shows the bands, the right picture the Wannier charge center of the Kane-Mele model with $\lambda_{\text{SO}} = 0.1 t$, $\lambda_{\nu} = 0.7 t$ and $\lambda_{\text{R}} = 0$.

to inversion symmetry. The latter symmetry is broken if an energy difference between the sublattices is applied by $\lambda_{\nu} \neq 0$. The eigenvalues can be easily calculated from matrix (2.20):

$$E_{\pm}^{\uparrow}(\mathbf{k}) = \pm \sqrt{|g_{\mathbf{k}}|^2 + (\gamma_{\mathbf{k}} + \lambda_{\nu})^2}, \quad (2.33)$$

$$E_{\pm}^{\downarrow}(\mathbf{k}) = \pm \sqrt{|g_{\mathbf{k}}|^2 + (\gamma_{\mathbf{k}} - \lambda_{\nu})^2}. \quad (2.34)$$

The corresponding bands and the WCC are shown in figure 2.9. The degeneracy of the bands is lifted in most regions of the Brillouin zone, the spin symmetry remains only between Γ and M since $\gamma(k_x = 0) = 0$ follows from equation (2.22). The system is still a topological insulator, the Chern invariants $C^{\uparrow} = 1$ and $C^{\downarrow} = -1$ are the same as in the case of $\lambda_{\nu} = 0$. If λ_{ν} is increased further, the gap closes at $\lambda_{\nu}^c = 3\sqrt{3}\lambda_{\text{SO}}$ as known from the Haldane model (see section 2.2). If the gap reopens for $\lambda_{\nu} > \lambda_{\nu}^c$, the system changes to an trivial band insulator. The corresponding bands and WCC are shown in figure 2.10. Note that the band structures on the left look similar in figure 2.9 and 2.10, although they belong to topologically distinct classes.

If $\lambda_{\text{R}} \neq 0$, the degeneracy of the bands is lifted everywhere except at the

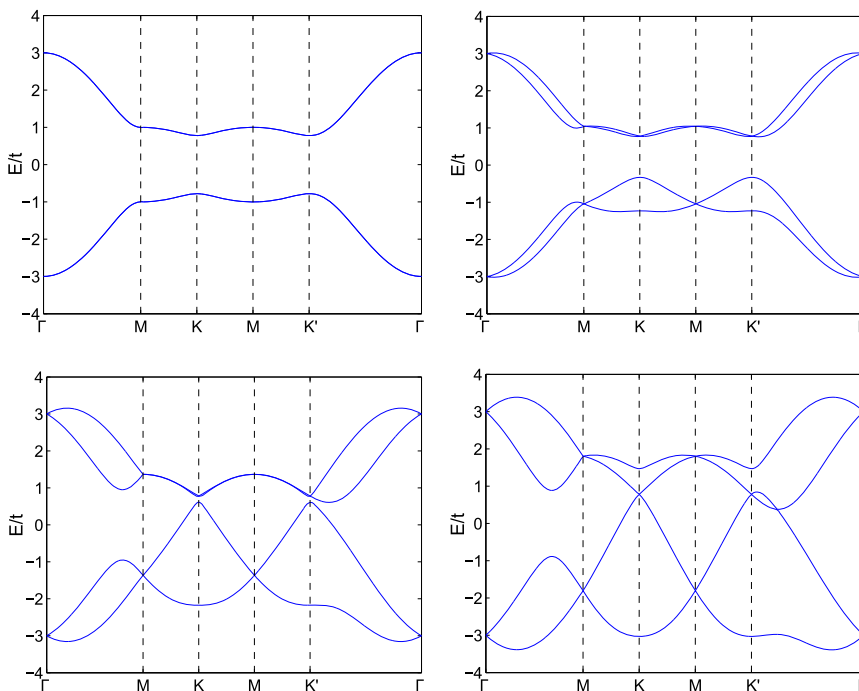


Figure 2.11: Bands of the Kane-Mele model with $\lambda_{\text{SO}} = 0.15t$ and $\lambda_{\nu} = 0$ for different values of λ_{R} . The Rashba coupling is $\lambda_{\text{R}} = 0$ in the upper left picture, $\lambda_{\text{R}} = \lambda_{\text{SO}}$ in the upper right, $\lambda_{\text{R}} = 3.1\lambda_{\text{SO}}$ in the lower left and $\lambda_{\text{R}} = 5\lambda_{\text{SO}}$ in the lower right.

time reversal invariant momenta (Kramers degeneracy). Furthermore, the minimum of the conduction bands shifts with increasing λ_{SO} and with increasing λ_{R} away from K and K' closer to Γ . An example is given in figure 2.11. If λ_{R} is increased further, the indirect band gap closes and the system becomes metallic. For instance, for $\lambda_{\text{SO}} = 0.15$ the gap closes at $\lambda_{\text{R}} = 3.09\lambda_{\text{SO}}$, as shown in figure 2.12. The corresponding bands are shown in the third picture of figure 2.11, where $\lambda_{\text{R}} = 3.1\lambda_{\text{SO}}$. However, the bands do not intersect until another critical value is exceeded. At the K point, this value only depends on the ratio $\lambda_{\text{R}}/\lambda_{\text{SO}}$ with the critical value $\lambda_{\text{R}}^{\text{c}}/\lambda_{\text{SO}} \approx 3.465$.

The Hamiltonian is not a combination of two Haldane Hamiltonians any more. Furthermore, the spin in z direction S_z is not conserved, which means that a topological analysis as in equation (2.14) is no longer possible, so only the definition of Fu and Kane can be taken into account. An example for the Wannier charge centers are given in figure 2.13. Because of $\lambda_{\nu} = 0$, the symmetry $\bar{x}_{\text{I}}(k_2) = -\bar{x}_{\text{II}}(k_2)$ is obeyed. Note that the colors in fig. 2.13 are chosen by the sign of $\langle u_{2\pi}(k_2) | S_z | u_{2\pi}(k_2) \rangle$. If $\lambda_{\text{R}} = 0$, S_z is conserved and hence the matrix element is ± 1 . If the spin symmetry is broken, the absolute value of the matrix element can be smaller than one. If the sign of $\langle u_{2\pi}^{\text{I}}(k_2) | S_z | u_{2\pi}^{\text{I}}(k_2) \rangle$ changes, the color changes, as for example in figure 2.15. Therefore, although it seems easy to trace the two WCC in figure 2.13, one cannot be sure if \bar{x}^{I} and

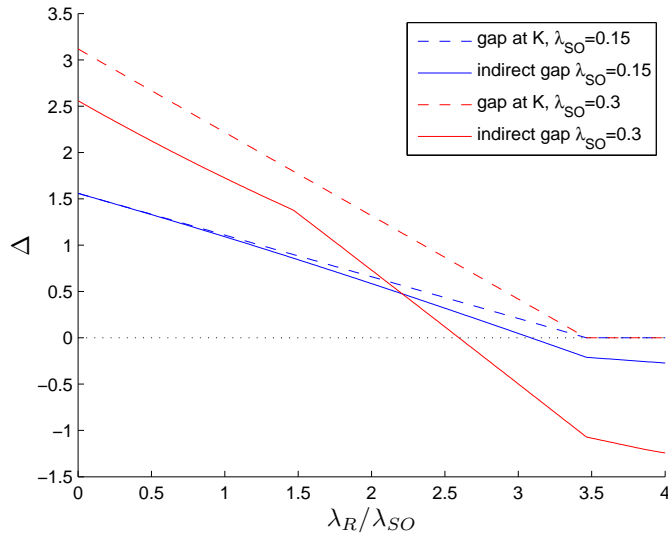


Figure 2.12: Band gap of the Kane-Mele model as a function of λ_R with $\lambda_\nu = 0$, and two different spin-orbit couplings $\lambda_\nu = 0$. The full curves are defined by the the minimum of the second highest energy band minus the maximum of the third highest. If this value is negative, the system is metallic. The dashed lines are the band gaps at the K points. The energy scale is fixed by $t = 1$.

\bar{x}^{II} have been assigned correctly. In contrast to the WCC without λ_R shown in figure 2.9, tracing \bar{x}^s is not possible and thus C_\uparrow and C_\downarrow are not defined. However, the \mathbb{Z}_2 invariant can be determined via the discontinuities of the maximum interspace function $z(k_2)$, as explained in section 1.7. If $\lambda_\nu = 0$, as in the analysis for the bands above, the Hamiltonian remains topological as long as the band gap persists. An example for the Wannier charge centers is given in figure 2.13. On the other hand, for metallic systems the topological classification is no longer valid (see section 1.6). In the limit $\lambda_{SO} \rightarrow 0$ the band gap closes only at the K point, wherefore the system is a topological insulator if $\lambda_R < \lambda_R^c \approx 3.465 \lambda_{SO}$ and metallic if $\lambda_R \geq \lambda_R^c$. For finite λ_{SO} , the metallic phase extends to smaller values of λ_R/λ_{SO} , as explained above and in figure 2.12.

If $\lambda_\nu \neq 0$ as well, the system remains in the Quantum Spin Hall phase until a critical value $\lambda_\nu^c(\lambda_R)$ is reached, where the band gap closes at the K points. $\lambda_\nu^c(\lambda_R)$ only depends on the ratios λ_ν/λ_{SO} and λ_R/λ_{SO} , but not on the magnitude of λ_{SO} . The phase boundary was calculated by determining the zeros of the band gap at the K points and is shown in figure 2.14. Note that it is symmetric in λ_ν and λ_R . As already described above, $\lambda_\nu^c = 0$ if $\lambda_R > \lambda_R^c \approx 3.465 \lambda_{SO}$. If $\lambda_R < \lambda_R^c$, $\lambda_\nu^c(\lambda_R)$ smoothly connects the point $(\lambda_R = \lambda_R^c, \lambda_\nu = 0)$ to the already analytically calculated critical point $(\lambda_R = 0, \lambda_\nu = 3\sqrt{3} \lambda_{SO})$. In the limit $\lambda_{SO} \rightarrow 0$, any $\lambda_\nu \neq \lambda_\nu^c$ gaps the system. The \mathbb{Z}_2 invariant ν is easily calculated for each phase using again the Soluyanov-Vanderbilt method. The phase diagram is shown in figure 2.14 [12], example Wannier charge centers are shown in figure 2.15. For finite λ_{SO} , the metallic phase is extended to smaller

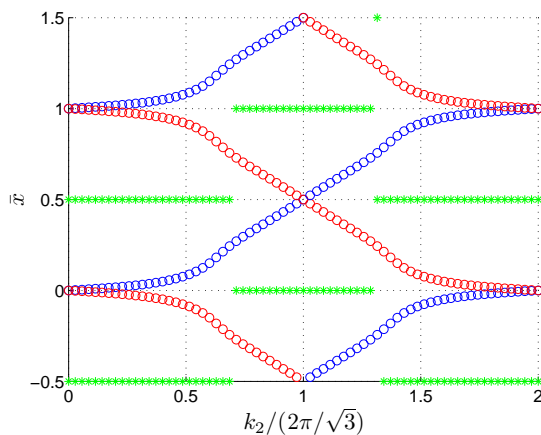


Figure 2.13: Wannier charge center for $\lambda_{\text{SO}} = 0.15$, $\lambda_{\text{R}} = 3\lambda_{\text{SO}}$ and $\lambda_{\nu} = 0$.

values of λ_{R} (see figure 2.12) and persists also for nonzero λ_{ν} . The corresponding phase diagram is exemplary shown for $\lambda_{\text{SO}} = 0.5$ in figure 2.16.

2.4 Ribbon

In section 1.9 the bulk boundary correspondence has been discussed. The aim of this section is to verify the correspondence for the Kane-Mele model and to analyse the transition as well as the properties of the edge states.

2.4.1 Geometry

In principle, the bulk boundary correspondence can be analyzed on any geometry that includes a region where the Chern number changes. In order to keep matrix dimensions low, it is preferable to retain translational invariance in one direction. Such a ribbon can appear in various forms depending on the orientation of the hexagon with respect to the boundary. In usual notation, the orientation is encoded in the primitive lattice vector \mathbf{R} of the ribbon which is expressed in terms of the primitive lattice vectors of graphene \mathbf{a}_1 and \mathbf{a}_2 , i.e. $\mathbf{R} = n\mathbf{a}_1 + m\mathbf{a}_2$ (see section 2.1). Because of the C_3 rotation symmetry of the lattice, only angles between $\theta = 0$ and $\theta = 30^\circ$ between x axis and boundary line of the ribbon have to be considered. The primitive lattice vectors can be chosen such that (n, m) are within this region $n > 0$ and $n > m > 0$. The ribbon $(n, m) = (1, 0)$ is called *zigzag* ribbon ($\theta = 0$), $(n, m) = (1, 1)$ called *armchair* ribbon ($\theta = 30^\circ$) due to the shape of their edges. The others are *chiral* ribbons, see figure 2.17. This notation is also applicable for nanotubes, but with the difference that lines illustrating the edges of ribbons shown in figure 2.17 represent the circumferences of the tubes. Since the primitive lattice vector of a tube is orthogonal to its circumference, the primitive lattice vector of a (n, m) nanotube is orthogonal to the primitive lattice vector of a (n, m) nanoribbon. Therefore, an armchair ribbon corresponds to a zigzag tube. The only difference between these two are boundary conditions which are open and

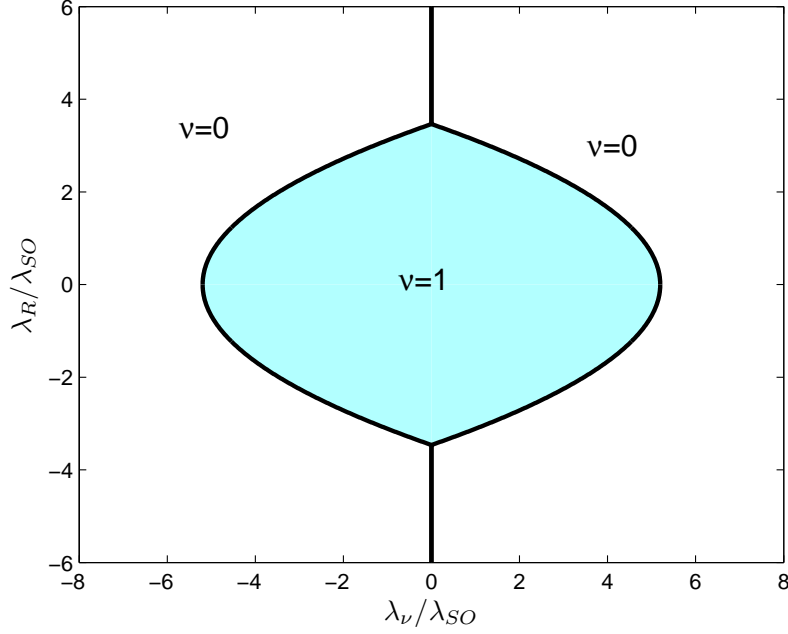


Figure 2.14: Phase diagram of the Kane-Mele model in the limit $\lambda_{SO} \rightarrow 0$. The black line denotes the metallic phase where the band gap at the K points closes. The topological trivial phase with \mathbb{Z}_2 invariant $\nu = 0$ is obtained if Rashba coupling λ_R or sublattice potential λ_ν are increased relative to spin-orbit coupling λ_{SO} [12].

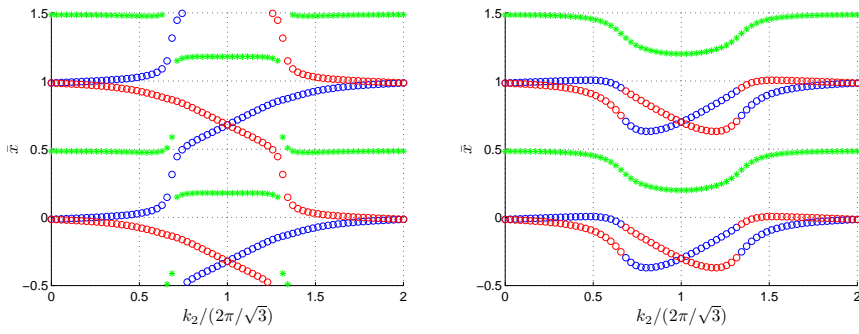


Figure 2.15: Quantum transition as a function of λ_R . For both WCC curves, $\lambda_{SO} = 0.1$ and $\lambda_\nu = 0.4$. In the left picture, $\lambda_R = 0.1$ ($\nu = 1$) and in the right $\lambda_R = 0.3$ ($\nu = 0$). Here one can see that ordering the WCC according to the sign of spin in z direction (red or blue, respectively) is not necessarily the correct order.

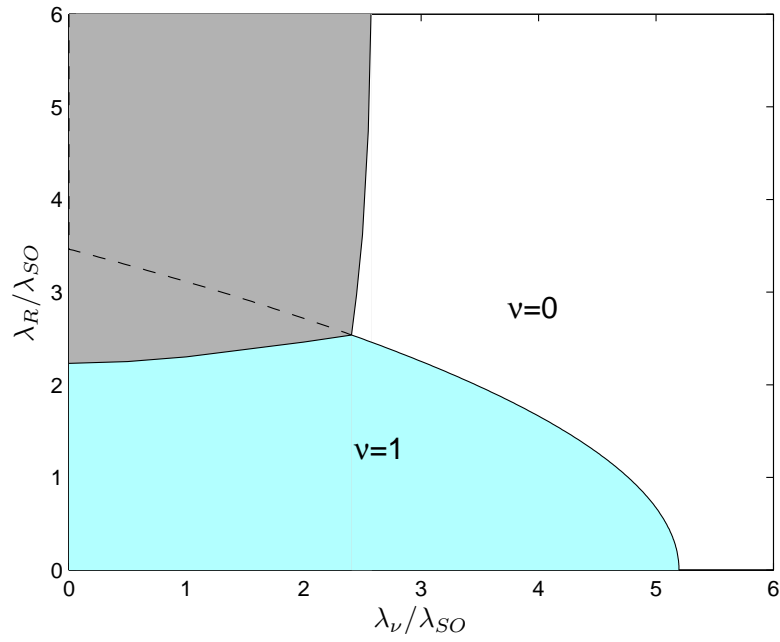


Figure 2.16: Phase diagram of the Kane-Mele model with a large spin-orbit coupling of $\lambda_{SO} = 0.5$. in contrast to figure 2.14, a metallic phase shown in grey appears. As a dashed line, the gap close at K is denoted, which is the only phase boundary in the limit $\lambda_{SO} \rightarrow 0$.

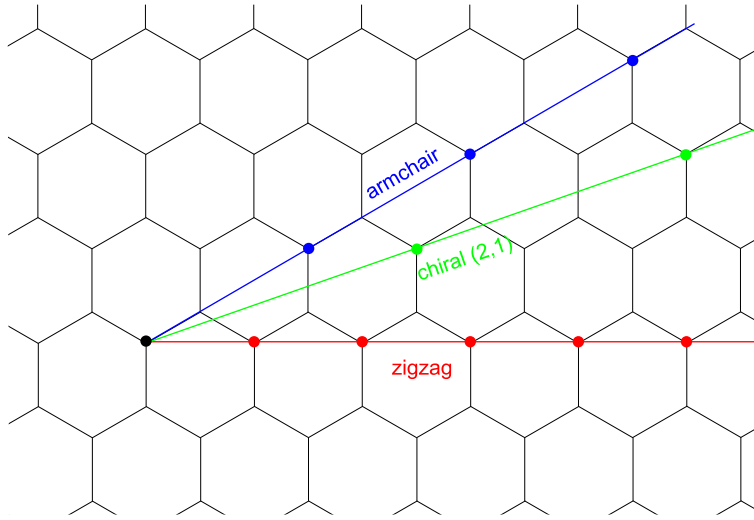


Figure 2.17: Edge orientation of a zigzag, an armchair and a chiral $(n,m)=(2,1)$ ribbon. The colored dots denote the respective equivalent lattice points to the black one.

periodic, respectively.

Comparing ribbons to tubes is helpful since the dispersion relation is easier to calculate using periodic boundary conditions since it can be determined from the bulk properties. The only difference between a tube and the extended sheet is that the values of the momentum around the circumference are quantised to $k_{\perp} = l/r$ where l is an integer and r the radius of the tube. Hence, the dispersion of nanotubes can be viewed as slices through the two-dimensional dispersion of a graphene sheet, see figure 2.18 [45]. Detailed analysis shows that the K point is an allowed momentum if $n - m$ is a multiple of 3 [45]. This has the consequence, that all armchair carbon nanotubes are metallic whereas two thirds of zigzag carbon nanotubes are semiconducting. Because of the similarity between armchair tubes and zigzag ribbons, all zigzag carbon nanoribbons are metallic whereas the properties of armchair ribbons depend on their width.

These general considerations are of course not sufficient to provide any qualitative information about edge states since those are emerging from open boundary conditions which are actually the only difference between armchair tubes and zigzag ribbons. However, regarding the results of the tubes, one can conclude that zigzag ribbons are preferable to armchair ribbons in order to analyse topological properties since the latter have a stronger dependence on the width. For example, an observed bandgap may not be due to spin-orbit coupling, but simply resulting from size effects. A further drawback of armchair ribbons is that both K and K' are mapped to $k_y = 0$, whereas they are mapped to $k_x = \pm 2\pi/3$ at zigzag ribbons. Therefore, possible differences between K and K' are easier identified at zigzag ribbons.

The geometry of a zigzag ribbon is shown in figure 2.19. If the number of

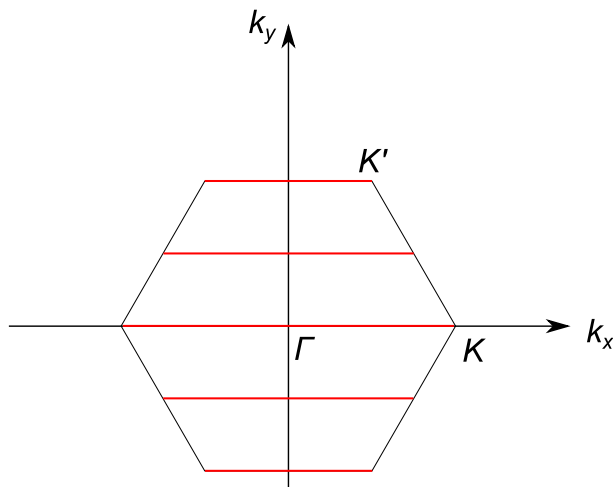


Figure 2.18: Allowed \mathbf{k} values in the Brillouin zone for an $(2, 2)$ armchair tube [45].

zigzag lines in x direction is called N , there are $N - 1$ rows of hexagons along the width of the ribbon. The periodicity along the x axis is the lattice constant of the 2D honeycomb lattice a , which is, as in the sections describing bulk properties, set to be 1. The primitive lattice vector is therefore $\mathbf{R} = (1, 0)$, see also figures 2.17 and 2.19. Each of the N zigzag lines contains one A and one B site within a unit cell, hence the total number of sites is $2N$.

2.4.2 Kane-Mele model on a zigzag ribbon

To calculate dispersion relations of the Kane-Mele model (2.12) on a zigzag ribbon, a Fourier transform is used. In contrast to the 2D bulk case examined in section 2.3.1, translational invariance is only valid in x , but not in y direction, wherefore Fourier transform can only be applied in one direction. The site indices in y direction remain as additional dimensions. The new basis is, similar to equation (2.19), $\Psi_{k_x}^\dagger \equiv (a_{k_x\uparrow}^\dagger, b_{k_x\uparrow}^\dagger, a_{k_x\downarrow}^\dagger, b_{k_x\downarrow}^\dagger)$. Here, however, $c_{k_x\sigma}^\dagger \equiv (c_{k_x1\sigma}^\dagger, c_{k_x2\sigma}^\dagger, \dots, c_{k_xN\sigma}^\dagger)$ is a vector of length N . In this basis the Hamiltonian has the form

$$H_{\text{KM}} = \sum_{k_x} \Psi_{k_x}^\dagger H(k_x) \Psi_{k_x}. \quad (2.35)$$

A derivation of the $4N \times 4N$ matrix $H(k_x)$ is given in appendix A.2.

Numerically calculating the eigenenergies as a function of k_x gives the results shown in figure 2.20 (see also [12, 44]). Because of the ribbon width of $N = 20$, the dimensionality is 80. Due to a degeneracy of 2 for all lines, each of the two bulk bands is represented by 38 lines and thus easily visible. Since the spin-orbit coupling is rather small ($\lambda_{\text{SO}} = 0.05$), the smallest bulk band gap is located at K and K' with a magnitude of $\Delta_{\mathbf{K}} = 6\sqrt{3}\lambda_{\text{SO}} \approx 0.52$ (see eq. (2.27)) which fits perfectly to the ribbon gap at $k_x = 2\pi/3$ and $k_x = 4\pi/3$, the momenta representing the K points in the zigzag ribbon. In addition to the

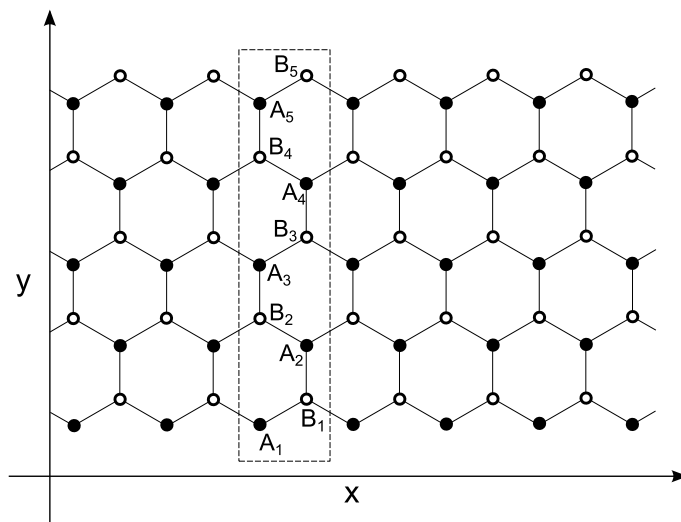


Figure 2.19: Zigzag ribbon of width $N = 5$. A unit cell is shown within the dashed rectangle and contains $2N = 10$ sites.

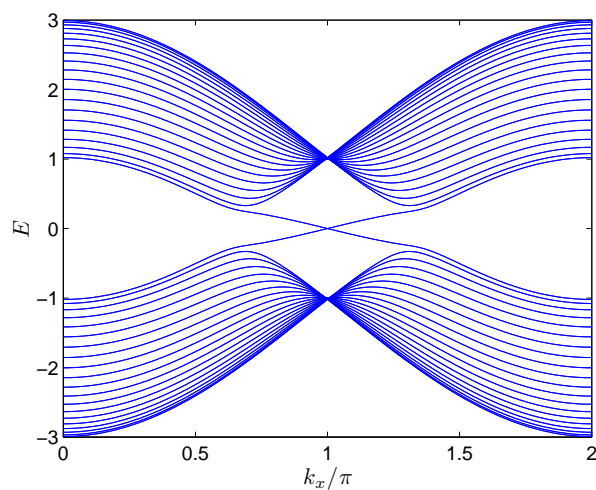


Figure 2.20: Eigenenergies of the Kane-Mele model for $\lambda_{SO} = 0.05$, $\lambda_\nu = \lambda_R = 0$ and $N = 20$ [12].

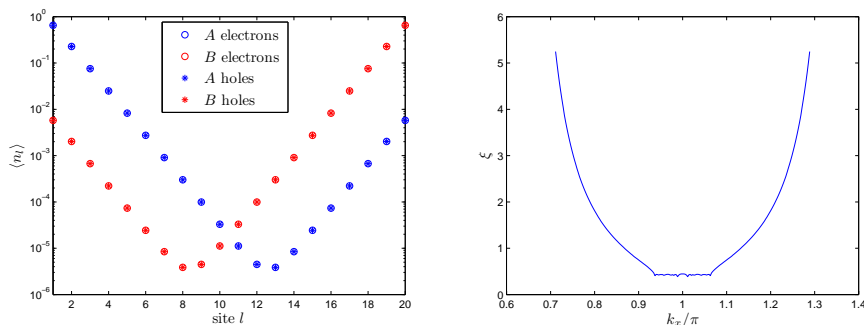


Figure 2.21: Localisation of the edge states at $\lambda_{\text{SO}} = 0.05$. The left picture shows the dependence on position of both electron and hole excitations. The right picture shows the correlation length ξ as a function of k_x .

dense lines representing the bulk bands, two additional excitations, each two fold degenerate, appear that close the gap at $k_x = \pi$. These excitations are the edge states caused by the change of topology at the boundary [44]. To check the level of localisation, the expectation value of the particle density as a function of the lattice sites is needed, which can be calculated from the eigenvectors of the Bloch matrix $H(k_x)$. For a certain k_x the eigenvectors $u_n(k_x)$ have $4N$ entries because of 2 spin, 2 sublattice and N position indices. The particle density as a function of sublattice $s \in \{A, B\}$, position l , Energy E and momentum k_x is given by summing the square of the eigenvectors over spin and degenerate energies, i.e.

$$\langle n_{sl}(E, k_x) \rangle = \sum_{n\sigma} \delta(E - E_n) |u_{n\sigma sl}(k_x)|^2. \quad (2.36)$$

The densities of both particle and hole like edge excitations for $\lambda_{\text{SO}} = 0.05$ and $k_x = 0.8\pi$ ($E(k_x) = \pm 0.173$) are shown in figure 2.21. One sees that densities of particle and hole like excitations are identical which is due to particle hole symmetry of the model. On the other hand, the densities on A and B sites differ strongly: The A sites are populated mostly at the lower edge whereas the B sites at the upper. The reason for that is that the ribbon starts with an A site and ends with a B site, see figure 2.19. All states are clearly localised exponentially at the edge with the same correlation length. This implies to fit the density at the first sites exponentially via $\langle n_l \rangle \propto e^{-l/\xi}$. The correlation length ξ does not depend on sublattice or edge, but only on the parameters of the Kane-Mele model and k_x . For $\lambda_{\text{SO}} = 0.05$, the correlation length of the lowest excitation is shown in figure 2.21 as a function of k_x . It diverges as k_x approaches $2\pi/3$ and $4\pi/3$, which means that the lowest excitation is indeed only an edge state when it splits off the bulk bands in order to close the gap in the region between the K points (see figure 2.20).

For a deeper analysis of the edge states, the degeneracy of the bands has to be lifted. This can be done for example by a sublattice potential λ_ν . The results are shown in the left picture of figure 2.22 for $\lambda_{\text{SO}} = 0.1$ and $\lambda_\nu = 0.2$. As in the case $\lambda_\nu = 0$, gap closing edge states exist, but the degeneracy is lifted. Considering the eigenvectors u_n of the edge states, it turns out that each

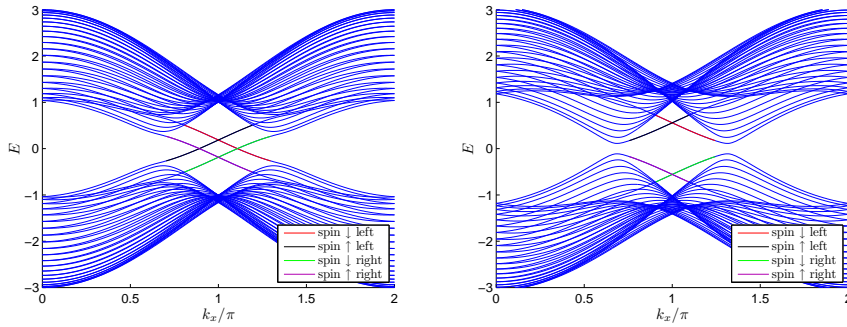


Figure 2.22: Dispersion relation of the Kane-Mele model on a zigzag ribbon for $\lambda_{\text{SO}} = 0.1$ and $\lambda_{\nu} = 0.2$ (left) and $\lambda_{\nu} = 0.6$ (right), respectively. Edge states localized more than 99% to a half of the ribbon are shown in different colors.

state is bound to only one edge and that it has a clearly defined spin. In the following I will use the notation right/left edge rather than upper/lower edge in order not to confuse with spin up/down. This corresponds to a rotation of 90° . Those eigenenergies corresponding to eigenvectors whose spin polarisation is over 99% and where over 99% of the weight is on the left/right half of the ribbon are displayed in a different color. It can be seen that all states with finite correlation length are polarised in spin and edge. If λ_{ν} is increased further, it is known from the bulk system that a quantum phase transition to a trivial band insulator happens at $\lambda_{\nu} = 3\sqrt{3}\lambda_{\text{SO}}$. An example for this phase is given in the right picture of figure 2.22. Localized edge states still persist, but they do not close the gap any more. This is expected because of bulk boundary correspondence. One interesting feature of the edge states is that all excitations at the left edges are particle like whereas all at the right hole like. The reason for that is that the left edge starts with an A site that has an higher onset energy than the B site on the right edge. If a Rashba coupling is added as well, the edge states are still bound to one edge, but the spin polarisation is destroyed.

Chapter 3

Kane-Mele-Hubbard model

The Kane-Mele model is a band theory that does not include any explicit electron-electron interaction. Coulomb repulsion is easiest added by using a Hubbard term $U \sum_i n_{i\uparrow} n_{i\downarrow}$ introduced by John Hubbard in 1963 to describe intra-atomic interaction which is important for narrow bands [46]. Here, $n_{i\sigma}$ are the number operators of site i and spin σ defined by $n_{i\sigma} \equiv c_{i\sigma}^\dagger c_{i\sigma}$. The parameter U controls the strength of the repulsion. The Hubbard term is frequently used to describe band magnetism and metal insulator transitions, so called Mott transitions [47]. The Kane-Mele-Hubbard model is an extended version of the Kane-Mele model that includes an on site Hubbard interaction controlled by a parameter U ,

$$H_{\text{KMH}} \equiv H_{\text{KM}} + U \sum_i n_{i\uparrow} n_{i\downarrow}. \quad (3.1)$$

This term was first considered by Rachel and Le Hur [13, 48], who did a mean-field approximation. As in many proceeding papers, in the original work the terminus Kane-Mele-Hubbard model denotes the minimal correlated model with a spin-orbit coupling and a Hubbard term, but without sublattice potential and Rashba coupling. In this chapter, the energy scale is set by $t = 1$.

The Kane-Mele model was an important milestone in the development of models featuring nontrivial topology giving an easy access to understand topological phase transitions. As a consequence, the KMH model with additional Hubbard interaction is supposed to be a toy model in order to understand the influence of interactions on topology. Therefore, it has been investigated by several methods after Rachel and Le Hur [48] first considered this model in mean-field approximation [13, 49–52]. Since in these methods beyond mean-field theory the picture of Bloch states breaks down, the topology has to be determined differently, as explained in section 1.8. In order to explain in principle how topology is affected by an interaction, in this chapter only the mean-field approximation is used since the same framework as for the noninteracting model (chapter 2) is applicable. The methods beyond mean-field are described in the next chapter 4. For the Hubbard model, the mean-field approximation reads:

$$U \sum_i n_{i\uparrow} n_{i\downarrow} \approx U \sum_i (\langle n_{i\uparrow} \rangle n_{i\downarrow} + \langle n_{i\downarrow} \rangle n_{i\uparrow} - \langle n_{i\uparrow} \rangle \langle n_{i\downarrow} \rangle). \quad (3.2)$$

Because of the periodicity of the lattice, it is assumed that the electron densities are identical in all unit cells. Therefore, 4 independent particle densities $\langle n_{A\uparrow} \rangle$, $\langle n_{B\uparrow} \rangle$, $\langle n_{A\downarrow} \rangle$ and $\langle n_{B\downarrow} \rangle$ remain because of two spins and two sublattices. Fixing the filling at one electron per site (half filling), three independent parameters that have to be determined self consistently define the system. One set of parameters is the ferromagnetic magnetisation M_F , the antiferromagnetic magnetisation M_{AF} and a sublattice difference ΔN_{AB} defined by

$$N = +\langle n_{A\uparrow} \rangle + \langle n_{B\uparrow} \rangle + \langle n_{A\downarrow} \rangle + \langle n_{B\downarrow} \rangle = 2 \quad (3.3)$$

$$M_F = +\langle n_{A\uparrow} \rangle + \langle n_{B\uparrow} \rangle - \langle n_{A\downarrow} \rangle - \langle n_{B\downarrow} \rangle \quad (3.4)$$

$$M_{AF} = -\langle n_{A\uparrow} \rangle + \langle n_{B\uparrow} \rangle + \langle n_{A\downarrow} \rangle - \langle n_{B\downarrow} \rangle \quad (3.5)$$

$$\Delta N_{AB} = -\langle n_{A\uparrow} \rangle + \langle n_{B\uparrow} \rangle - \langle n_{A\downarrow} \rangle + \langle n_{B\downarrow} \rangle \quad (3.6)$$

The mean-field Hamiltonian given by (3.1) and (3.2) is particle hole symmetric without the Rashba coupling. However, the energies are in general not symmetric around $E = 0$ any more. This could be fixed by a chemical potential μ . In the following all bands are shifted to be symmetric around 0, wherefore the constant $U \sum_i \langle n_{i\uparrow} \rangle \langle n_{i\downarrow} \rangle$ will not be mentioned any more since it might be included in the chemical potential. Writing the mean-field approximation $H_{MF} = U \sum_i (\langle n_{i\uparrow} \rangle n_{i\downarrow} + \langle n_{i\downarrow} \rangle n_{i\uparrow})$ in the same Bloch matrix representation as the noninteracting Kane-Mele model (2.20), one obtains

$$H_{MF} = U \begin{pmatrix} \langle n_{A\downarrow} \rangle & 0 & 0 & 0 \\ 0 & \langle n_{B\downarrow} \rangle & 0 & 0 \\ 0 & 0 & \langle n_{A\uparrow} \rangle & 0 \\ 0 & 0 & 0 & \langle n_{B\uparrow} \rangle \end{pmatrix} \quad (3.7)$$

Expanding this matrix to the basis of Dirac matrices (see section 2.3.1), the non-zero coefficients are proportional to the independent parameters N , M_F , M_{MF} and ΔN_{AB} defined in equations (3.3-3.6):

$$\begin{aligned} d_0 &= U/4 N \\ d_2 &= -U/4 \Delta N_{AB} \\ d_{15} &= U/4 M_{AF} \\ d_{34} &= -U/4 M_F \end{aligned} \quad (3.8)$$

Since $d_{ab}(\mathbf{k}) = -d_{ab}(-\mathbf{k})$ is necessary for time reversal invariance (see section 2.3.1), any kind of magnetisation breaks time reversal symmetry.

3.1 Magnetisation

The values of M_F , M_{MF} and ΔN_{AB} have to be determined self consistently. From a given set of $\langle n_r \rangle$ where r denotes both spin and sublattice variable $r \in \{A \uparrow, B \uparrow, A \downarrow, B \downarrow\}$, the eigenvalues and eigenvectors can be calculated. However, the occupied eigenstates u_l determine the occupation numbers $\langle n_r \rangle$ via

$$\langle n_r \rangle = \frac{1}{N_\Lambda} \sum_{\mathbf{k}} \sum_l \Theta(E - E_l) |u_{l\mathbf{k}}^r(\langle n_{A\uparrow} \rangle, \langle n_{B\uparrow} \rangle, \langle n_{A\downarrow} \rangle, \langle n_{B\downarrow} \rangle)|^2. \quad (3.9)$$

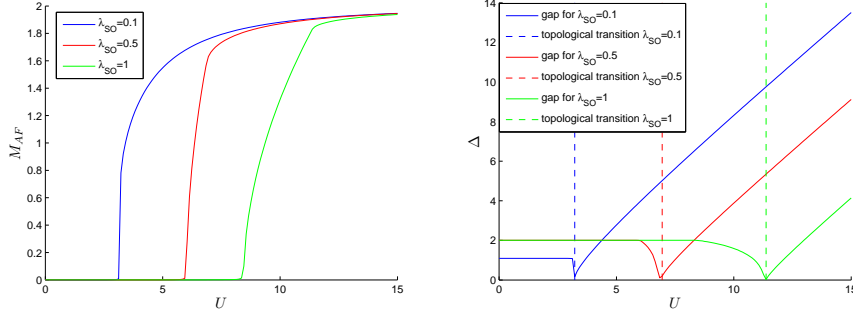


Figure 3.1: The left picture shows the antiferromagnetic moment of the mean-field KMH Hamiltonian as a function of U for three different λ_{SO} , the right the corresponding gaps. The dashed line indicates the topological transition.

The eigenvectors $u_{l\mathbf{k}}$ can be calculated by diagonalizing $H(\mathbf{k}) + H_{\text{MF}}$ given by the equations (2.20) and (3.7). If $\lambda_{\text{R}} = 0$ the matrix decouples into two 2×2 matrices and the eigenvectors can be easily determined analytically. The eigenenergies are given by

$$E_{\pm}^{\uparrow}(\mathbf{k}) = \pm \sqrt{|g\mathbf{k}|^2 + \left[\gamma\mathbf{k} + \lambda_{\nu} + \frac{U}{2} (\langle n_{A\downarrow} \rangle - \langle n_{B\downarrow} \rangle) \right]^2}, \quad (3.10)$$

$$E_{\pm}^{\downarrow}(\mathbf{k}) = \pm \sqrt{|g\mathbf{k}|^2 + \left[-\gamma\mathbf{k} + \lambda_{\nu} + \frac{U}{2} (\langle n_{A\uparrow} \rangle - \langle n_{B\uparrow} \rangle) \right]^2}. \quad (3.11)$$

With these eigenvalues, it is straight forward to calculate the eigenvectors. The four densities $\langle n_r \rangle$ have to be chosen such that the four self consistency equations (3.9) are satisfied. This can be done numerically by assuming initial values for $\langle n_r \rangle_0$ and iteratively calculating new densities $\langle n_r \rangle_{s+1}$ until a stationary point is reached. A mixing, i.e. $\widetilde{\langle n_r \rangle}_{s+1} = a \langle n_r \rangle_{s+1} + (1-a) \langle n_r \rangle_s$, improves the stability and avoids a divergent behaviour. Depending on the parameters, a was chosen between 0.3 and 0.7. If $\lambda_{\nu} = 0$, the Hamiltonian is symmetric in A and B wherefore ΔN_{AB} has to vanish. If furthermore the ferromagnetic magnetisation is assumed to vanish, the self consistency simplifies to [48]

$$M_{\text{AF}} = \frac{1}{N_{\Lambda}} \sum_{\mathbf{k}} \frac{M_{\text{AF}} U / 2 - \gamma\mathbf{k}}{\sqrt{|g\mathbf{k}|^2 + (\gamma\mathbf{k} - M_{\text{AF}} U / 2)^2}}. \quad (3.12)$$

If all 4 densities $\langle n_r \rangle$ are free to vary, it turns out that this assumption is indeed correct and that the ferromagnetic magnetisation M_{F} vanishes for all parameter sets.

Considering the Kane-Mele-Hubbard (KMH) model without sublattice potential and Rashba coupling, an antiferromagnetic ordering appears if U is above a critical value $U_1^c(\lambda_{\text{SO}})$. The order parameter rises continuously from 0 above U_1^c , wherefore the phase transition is of second order, see figure 3.1. In the limit $U \rightarrow \infty$ the antiferromagnetic moment approaches the saturation value 2, which

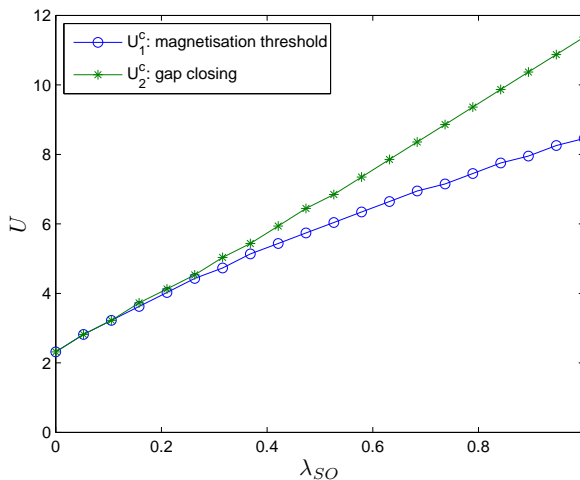


Figure 3.2: Phase diagram of the KMH model in mean-field approximation without sublattice potential and Rashba coupling. For $U < U_1^c$ the system is a topological Quantum Spin Hall insulator (QSH). For U larger than U_1^c an antiferromagnetic moment appears, but between U_1^c and U_2^c the QSH structure remains. See also [48].

corresponds to a fully polarized system. The dependence of U_1^c on λ_{SO} is shown in figure 3.2 [48]. As seen in section 2.3.3, another point in parameter space that possibly yields a phase transition is a closing of the band gap. Looking at the band gap $\Delta(U)$, it remains constant ($\Delta = 6\sqrt{3}\lambda_{SO}$ if $\lambda_{SO} < 1/(3\sqrt{3})$ and $\Delta = 2$ else, see section 2.3.2) as long as the antiferromagnetic moment vanishes. With increasing magnetic moment at $U > U_1^c$ the band gap decreases, closes at another critical interaction $U_2^c(\lambda_{SO})$ and reopens for larger values $U > U_2^c$. As a function of spin-orbit coupling, $U_2^c(\lambda_{SO})$ is shown in figure 3.2.

3.2 Topological transitions

As already seen in the noninteracting case, a band gap closing might be an indication for a topological transition. Furthermore, an antiferromagnetic moment changes symmetries and can thus change the topological structure as well. Hence, three different phases are possible as U varies. Wannier charge centers (WCC, see section 1.5) are used here in order to analyse topological properties since they give a detailed insight in both quantum spin Hall structure (1.28) and the Fu-Kane definition of the \mathbb{Z}_2 invariant (1.53).

As U increases from 0, bands and WCC do not change as long as the antiferromagnetic moment remains 0, as can be seen by comparing the first two rows of figure 3.3. For $U > U_1^c$, M_{AF} is non zero, which has important influence on topology. The magnetisation destroys time reversal symmetry, since d_{15} in equation (3.8) is even in \mathbf{k} instead of odd, as required for \mathcal{T} (see section 2.3.1).

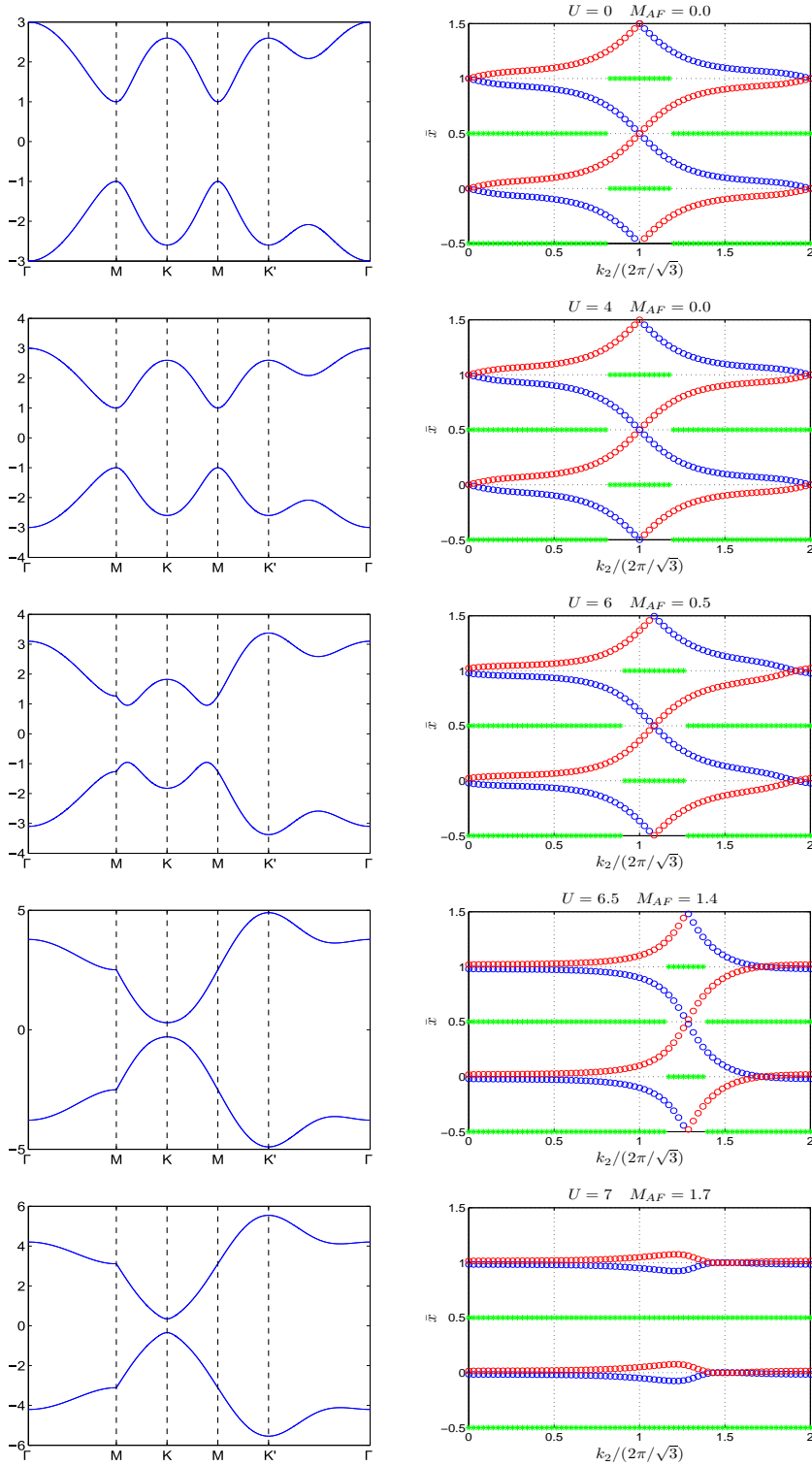


Figure 3.3: Bands and Wannier charge centers for $\lambda_{\text{SO}} = 0.5$, $\lambda_{\nu} = 0$ and λ_{R} for various values of U .

This has the consequence that the definition of the \mathbb{Z}_2 invariant by Fu and Kane (see section 1.6) cannot be used since time reversal is preconditioned. The absent \mathcal{T} symmetry can be seen as well from the bands since K and K' are no longer equivalent and from the WCC since $\bar{x}^I \neq \bar{x}^{II}$ at $k_2 = 0$ and $k_2 = 2\pi/\sqrt{3}$ as required by Kramers degeneracy. However, a definition via a spin Chern number is still possible since S_z is a conserved quantity as long as $\lambda_R = 0$. Hence, as long as no Rashba coupling is present, the spin Chern number is defined and can easily be used to calculate a topological invariant. The WCC related to spin up (red) still changes by 1 wherefore $C^\uparrow = 1$ and analogously $C^\downarrow = -1$. Hence, although a magnetisation is present and \mathcal{T} symmetry is broken, $C_s = 1$. To sum up, the first transition at $U = U_1^c$ is from a non magnetic quantum spin Hall phase to an antiferromagnetic QSH which has the same spin Chern structure. The second transition at $U = U_2^c$ is of a completely different kind. Looking at the bands one sees that with increasing M_{AF} the gap at K becomes smaller whereas it increases at K' . At U_2^c the antiferromagnetic field is strong enough that the bandgap closes. This becomes clear by looking at the energies at the K point. Using equation (3.10) with $g_K = 0$, $\gamma_K = 3\sqrt{3}$ and $\lambda_\nu = 0$, the band gaps at K and K' are

$$\Delta_{K',K} = \left| 6\sqrt{3} \pm \frac{U}{2} M_{AF} \right|. \quad (3.13)$$

It has been used that $\langle n_{A\uparrow} \rangle - \langle n_{B\uparrow} \rangle = \langle n_{A\downarrow} \rangle - \langle n_{B\downarrow} \rangle = -M_{AF}/2$ because of the symmetry of the sublattices. The plus sign is valid at K' , the minus sign at K . Note that from the symmetry it follows that there are always two equivalent solutions for the magnetisation, namely $+M_{AF}$ which corresponds to the structure $A \downarrow B \uparrow$ and $-M_{AF}$ which corresponds to the structure $A \uparrow B \downarrow$. A negative magnetisation is equivalent to exchanging K and K' . From equation (3.13) it follows that the gap closes at K or K' if $U |M_{AF}(U)| = 12\sqrt{3}$ which implicitly defines U_2^c . For larger interaction and hence larger magnetisation the bandgap reopens again, but the Chern numbers C^\uparrow and C^\downarrow become 0, as can be seen in the last row of figure 3.3. The transition from a QSH phase to a trivial insulator after a band gap close is similar to the quantum phase transition caused by λ_ν , see section 2.3.3. The only difference is that in both phases time reversal symmetry is broken due to the magnetic moment.

3.2.1 Generalisation of \mathbb{Z}_2 invariant definition

As already mentioned, the Fu-Kane definition of ν is not applicable if time reversal symmetry is broken, but it is possible to generalize it. Comparing the WCC with and without magnetisation ($U = 4$ and $U = 6$) in figure 3.3, they look similar despite the fact that the crossing points shift slightly away from $k_2 = 0$ and $k_2 = 2\pi/\sqrt{3}$. Hence it is promising to regard the whole period instead of just one half, but in order to get the same constant one has to divide by 2. Generalizing the Fu-Kane definition (1.53) with that purpose results in

$$\nu \equiv (P_\theta[T] - P_\theta[0]) / 2 \quad \text{mod } 2 \quad (3.14)$$

Here it should be stressed that the gauge has to be chosen such that P_θ is continuous, since $P_\theta[T] = P_\theta[0] \quad \text{mod } 1$ which means that the right side of equation

(3.14) always vanishes if the gauge is not fixed. Hence, one can calculate the topological invariant in the sense of Soluyanov and Vanderbilt which is equivalent to the Fu-Kane definition (see section 1.7) by counting the jumps in the maximum interspace function $z(k_2)$ within a full period and divide by 2 instead of just counting within a half period. However, one has to be aware that this only works if \bar{x}^I and \bar{x}^{II} intersect within each region where $z(k_2)$ is continuous. Consider a case that \bar{x}^I and \bar{x}^{II} just come close, but do not intersect, so that $z(k_2)$ jumps twice. Dividing by 2, as proposed, this would change the topological constant by 1. In the time reversal symmetric case this had not been a problem because of Kramers degeneracy: Intersection at the time reversal invariant momenta ($k_x = 0$ and $k_x = \pi/\sqrt{3}$ in the case of hexagonal lattices) is guaranteed. Furthermore a scenario as described above where \bar{x}^I and \bar{x}^{II} come close but do not intersect somewhere away from TRIM is doubled since k and $-k$ are equivalent. Modulo 2 the change in topological invariant is thus 0. If \mathcal{T} symmetry is broken, a numerical threshold can be used to figure out whether or not the curves intersect, but this is a possible source of inaccuracy. Thus, if \mathcal{T} symmetry is broken but spin is conserved, separating the WCC by spin and tracing them is preferable to the Fu-Kane definition. Therefore, this generalized Fu-Kane method will only be used when $\lambda_R \neq 0$ and time reversal symmetry is broken (see section 3.4). However, in the simple KMH model here, both methods have been used in order to check the reliability of the generalized Soluyanov-Vanderbilt method. The results gained were identical for all considered parameters.

To conclude, two definitions of a topological order exist: The Fu-Kane definition is suitable for time-reversal symmetric systems, the quantum spin Hall picture is applicable if the spin in z direction is conserved. The definition given here in this section combines the two definitions, including both kinds of topological systems. However, if both time-reversal symmetry and S_z conservation are violated, a phase with a nontrivial generalised invariant according to equation (3.14) may have different properties than topological systems obeying at least one of the two symmetries. For instance, the edge states do not necessarily close the gap, as observed later in section 3.5.2.

3.3 Influence of a sublattice potential

As mentioned in the previous section, the quantum phase transition that takes place as U is increased is similar to the phase transition obtained by high values of λ_ν . In this section it is discussed what happens if the two parameters act together. A qualitative difference to the case of $\lambda_\nu = 0$ is that ΔN_{AB} can be different from zero due to symmetry breaking. Hence, next to the antiferromagnetic moment a second parameter has to be determined self consistently. Since a positive λ_ν shifts lattice sites A to higher energies than sites B , the density at B will be higher and according to definition (3.5). The term originating from this additional mean-field parameter ΔN_{AB} has the same matrix form as the sublattice potential λ_ν . Comparing equations (3.8) and (2.25), the new effective sublattice potential is

$$\lambda_\nu^{\text{eff}} = \lambda_\nu - \frac{U}{4} \Delta N_{AB} \quad (3.15)$$

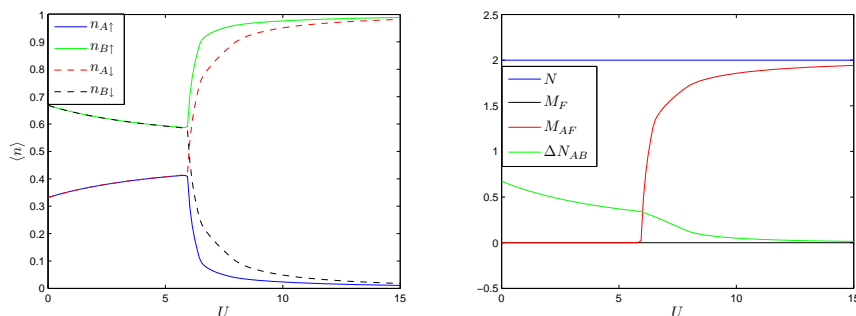


Figure 3.4: The left picture shows the electron densities $\langle n_r \rangle$ for $\lambda_{\text{SO}} = 0.5$ and $\lambda_\nu = 1$ as a function of U . On the right, the associated magnetisations and density variations are shown.

For fixed $\lambda_{\text{SO}} = 0.5$ and $\lambda_\nu = 2\lambda_{\text{SO}}$ the electron densities $\langle n_r \rangle$ as well as the parameters N , M_F , M_{AM} and ΔN_{AB} are shown as a function of U in figure 3.4. The total density N is fixed at 2 because of half filling. Because of particle-hole symmetry, the chemical potential is again chosen such that the energy bands are symmetric around zero. The magnetic moments behave similar to the case $\lambda_\nu = 0$ described in the last section. The ferromagnetic moment always remains zero whereas the antiferromagnetic moment is non zero for U larger than a threshold value U_1^c . In addition, λ_ν causes ΔN_{AB} to be different from zero. With increasing U this parameter decreases since $M_{AF} + \Delta N_{AB} = 2\langle n_{B\uparrow} \rangle - 2\langle n_{A\uparrow} \rangle \leq 2$ and in the limit $U \rightarrow \infty$ the system tends to a totally polarized state with $M_{AF} = 2$. The antiferromagnetic threshold value U_1^c is shown as a function of λ_ν for $\lambda_{\text{SO}} = 0.5$ in figure 3.5.

In order to analyse the topological properties, let me recapitulate the transitions known from the special cases $U = 0$ and $\lambda_\nu = 0$. In the noninteracting case it has been shown that the transition from a quantum spin Hall insulator to a trivial insulator takes place at $\lambda_\nu^c = 3\sqrt{3}\lambda_{\text{SO}}$. As long as the antiferromagnetic moment vanishes, i.e. $U < U_1^c$, the mean-field Hamiltonian is identical to the noninteracting Hamiltonian besides the renormalisation of λ_ν given by equation (3.15). Hence, for $0 < U < U_1^c$ the band gap closes at a critical value of λ_ν given by

$$\lambda_\nu^c(U)/\lambda_{\text{SO}} = 3\sqrt{3} + \frac{U}{4}\Delta N_{AB}(U, \lambda_\nu). \quad (3.16)$$

The numerical results of (3.16) are shown for $\lambda_{\text{SO}} = 0.5$ in figure 3.5. The curve $\lambda_\nu^c(U)$ seems to have a linear behaviour. For $\lambda_{\text{SO}} = 0.5$, a linear fit gives $\lambda_\nu^c(U)/\lambda_{\text{SO}} \approx 3\sqrt{3} + 0.78U$. As does the threshold interaction of magnetisation, the slope depends on λ_{SO} . For example, for $\lambda_{\text{SO}} = 0.1$ the result is $\lambda_\nu^c(U)/\lambda_{\text{SO}} \approx 3\sqrt{3} + 1.13U$. Because of the similarity to the noninteracting Hamiltonian it is expected that for larger values of λ_ν the topology becomes trivial. Using Wannier charge centers this is easily provable. When calculating $\lambda_\nu^c(U)$, next to the bandgap the topological invariant has been calculated as well using Soluyanov-Vanderbilt method. For $U = 4$ both bandgap and topological transition are shown in figure 3.6. Clearly, the close of the bandgap coincides

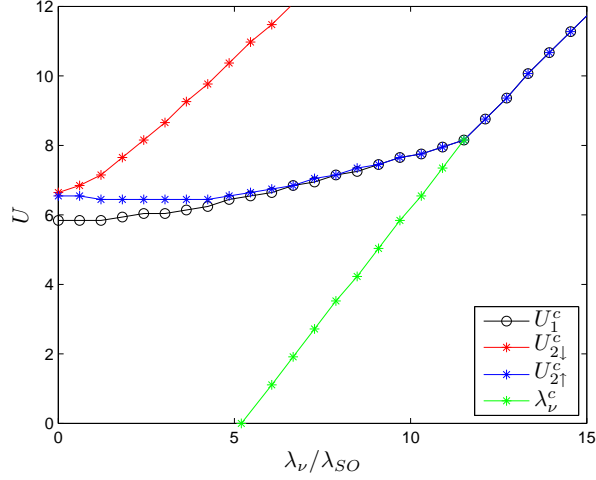


Figure 3.5: Transitions occurring in the Kane-Mele-Hubbard model varying λ_ν and U . U_1^c is the threshold for magnetisation,

with the transition, as expected.

A second topological transition is known from the special case $\lambda_\nu = 0$. In section 3.2 it has been analysed that a large antiferromagnetic moment destroys the topological order. The magnetisation threshold is called U_1^c , the slightly higher interaction that causes the topological transition U_2^c . With a sublattice potential different from zero, the degeneracy of spin up and spin down electrons is broken due to λ_ν and an unequal occupation of the sublattices $\Delta N_{AB} \neq 0$ is resulting. The effective energy difference is again given by equation (3.15). As a consequence, the gap size at K becomes spin dependent. The resulting generalisation of equation (3.13) is

$$\Delta_{\mathbf{K},\mathbf{K}'}^\uparrow = \left| 6\sqrt{3} \pm \left[\frac{U}{2} (M_{\text{AF}} - \Delta N_{AB}) + 2\lambda_\nu \right] \right|, \quad (3.17)$$

$$\Delta_{\mathbf{K},\mathbf{K}'}^\downarrow = \left| 6\sqrt{3} \pm \left[\frac{U}{2} (M_{\text{AF}} + \Delta N_{AB}) - 2\lambda_\nu \right] \right|. \quad (3.18)$$

The gap close $\Delta = 0$ defines a topological transition which leads to equations determining U_2^c implicitly:

$$4 \left(3\sqrt{3} - \lambda_\nu \right) = U_{2\uparrow}^c \left[M_{\text{AF}}(U_{2\uparrow}^c) - \Delta N_{AB}(U_{2\uparrow}^c) \right], \quad (3.19)$$

$$4 \left(3\sqrt{3} + \lambda_\nu \right) = U_{2\downarrow}^c \left[M_{\text{AF}}(U_{2\downarrow}^c) + \Delta N_{AB}(U_{2\downarrow}^c) \right]. \quad (3.20)$$

This means that the transition is different for spin up and spin down electrons. The gap size as a function of U for fixed λ_ν is shown in figure 3.7, the critical interactions $U_{2\uparrow}^c$ and $U_{2\downarrow}^c$ causing the gap close calculated numerically from equation (3.17) are shown as a function of λ_ν in figure 3.5. In addition, the Chern numbers have been determined separately for spin up and spin down electrons using Wannier charge centers. This is possible since spin is conserved

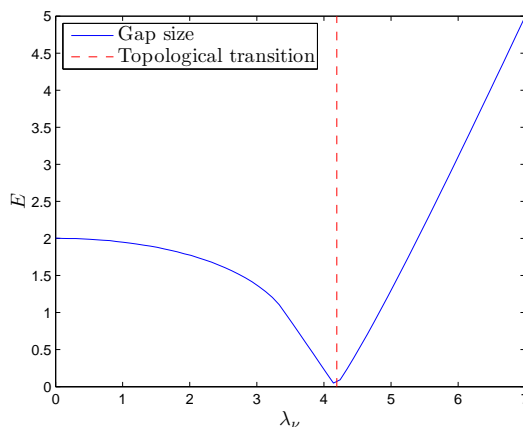


Figure 3.6: Gap size as a function of λ_ν for $\lambda_{\text{SO}} = 0.5$ and $U = 4$. The dashed line denotes the topological transition: To the left of the line, $\nu = 1$, to the right $\nu = 0$ according to the definition of Fu and Kane.

because of the absence of the Rashba coupling (see section 2.3.3). Example WCC curves are shown with the associated bands in figure 3.8. Changes in the Chern numbers are shown together with the band gap in figure 3.7. As already known, they coincide perfectly with the band gap closes.

Since all transitions of the Kane-Mele-Hubbard model have been described (see figure 3.5), the phase diagram can be analysed in detail. The different phases are labelled in figure 3.9. In the case $U < U_1^c$, the system is non-magnetic. If furthermore $\lambda_\nu < \lambda_\nu^c$, the \mathbb{Z}_2 invariant is nontrivial, i.e. $\nu = 1$. Note that the Fu-Kane definition (1.53) and the definition via the spin Chern number (1.28) are equivalent due to \mathcal{T} symmetry and conservation of S_z . This phase, in figure 3.9 colored in pink, is adiabatically connected to the most simple model of a topological insulator consisting only of a tight-binding and a spin-orbit term. Hence, this phase is still a combination of two Haldane models with opposing Chern number for each spin. If $\lambda_\nu > \lambda_\nu^c(U)$, the spin Hall structure is destroyed. Therefore, a trivial band insulator is realized as also known from the Haldane model (shown in light blue in figure 3.9).

For $U > U_1^c$, the antiferromagnetic moment does not vanish: This has the consequence that \mathcal{T} symmetry is broken, wherefore the Fu-Kane definition of ν cannot be used. The region $U < U_{2\downarrow}^c$ marks an antiferromagnetic quantum spin Hall insulator ($C^\uparrow = 1, C^\downarrow = -1 \Rightarrow C^s = 1$), for $U > U_{2\uparrow}^c$ the topological order is destroyed and a trivial antiferromagnetic state ($C^\uparrow = 0, C^\downarrow = 0 \Rightarrow C^s = 0$) is realized. These two regions, colored light red and blue in figure 3.9, are adiabatically connected to the two different magnetic phases existing for $\lambda_\nu = 0$. This can be seen by comparing bands and WCC shown in the figures 3.3 and 3.8. A detailed analysis of these phases is given in section 3.2. In addition, a new phase appears for $U_{2\downarrow}^c < U < U_{2\uparrow}^c$. In this region, one Chern number is trivial whereas the other is not. Therefore, the total Chern number is nontrivial

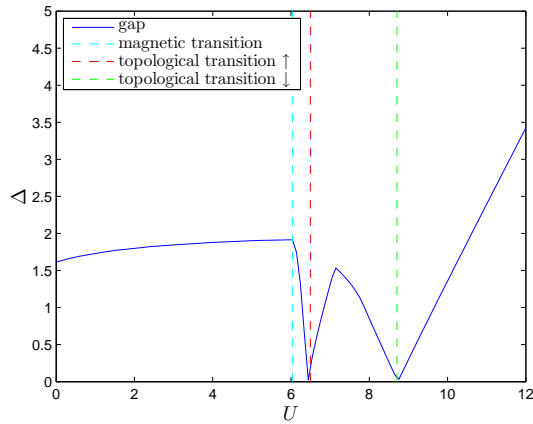


Figure 3.7: Gap size as a function of U for $\lambda_{\text{SO}} = 0.5$ and $\lambda_{\nu} = 1.5$. The dashed lines denote transitions: The cyan line is the onset of magnetisation, red and green lines mark changes in C^{\uparrow} and C^{\downarrow} , respectively.

$C = C^{\uparrow} + C^{\downarrow} = 1$. Since the Chern number is related to the Hall conductivity (see section 1.3), The Hall effect is non zero even without a magnetic field. Therefore, the desired phase is a quantum anomalous Hall state.

To conclude, I will briefly recapitulate the phases of the Kane-Mele-Hubbard model in mean-field approximation referring to the Haldane model. As described in section 2.2, the Haldane model has been introduced to describe systems with intrinsic quantum Hall effect without requiring a magnetic field. For that purpose, time reversal symmetry has to be broken. The Kane-Mele model without Rashba interaction is a combination of two Haldane models, one for each spin, to obey \mathcal{T} symmetry. The total Chern number is therefore 0, but the topology for each spin is still nontrivial. An antiferromagnetic moment caused by a strong mean-field interaction lifts \mathcal{T} symmetry and together with a sublattice potential λ_{ν} the two modified Haldane models are not opposing each other any more. This makes it possible that the Hamiltonians for each spin are in different topology classes. In that case, the system becomes a quantum anomalous Hall insulator with non-zero Chern number just like the Haldane model, but with a spin dependent Hall conductivity.

3.4 Influence of Rashba coupling

In the case of a noninteracting Kane-Mele model (section 2.3.3) the only additional phase appearing when $\lambda_{\text{R}} \neq 0$ is a metallic one, realized for large λ_{R} . The critical coupling decreases if λ_{SO} increases and increases with growing λ_{ν} . Hence, in order to emphasise the influence of a Rashba coupling, in this section a phase diagram with axes λ_{R} and U is analysed, with $\lambda_{\text{SO}} = 0.5$ (as in the previous chapter) and $\lambda_{\nu} = 0$.

For $U = 0$ it is known from section 2.3.3 that the system is a topological

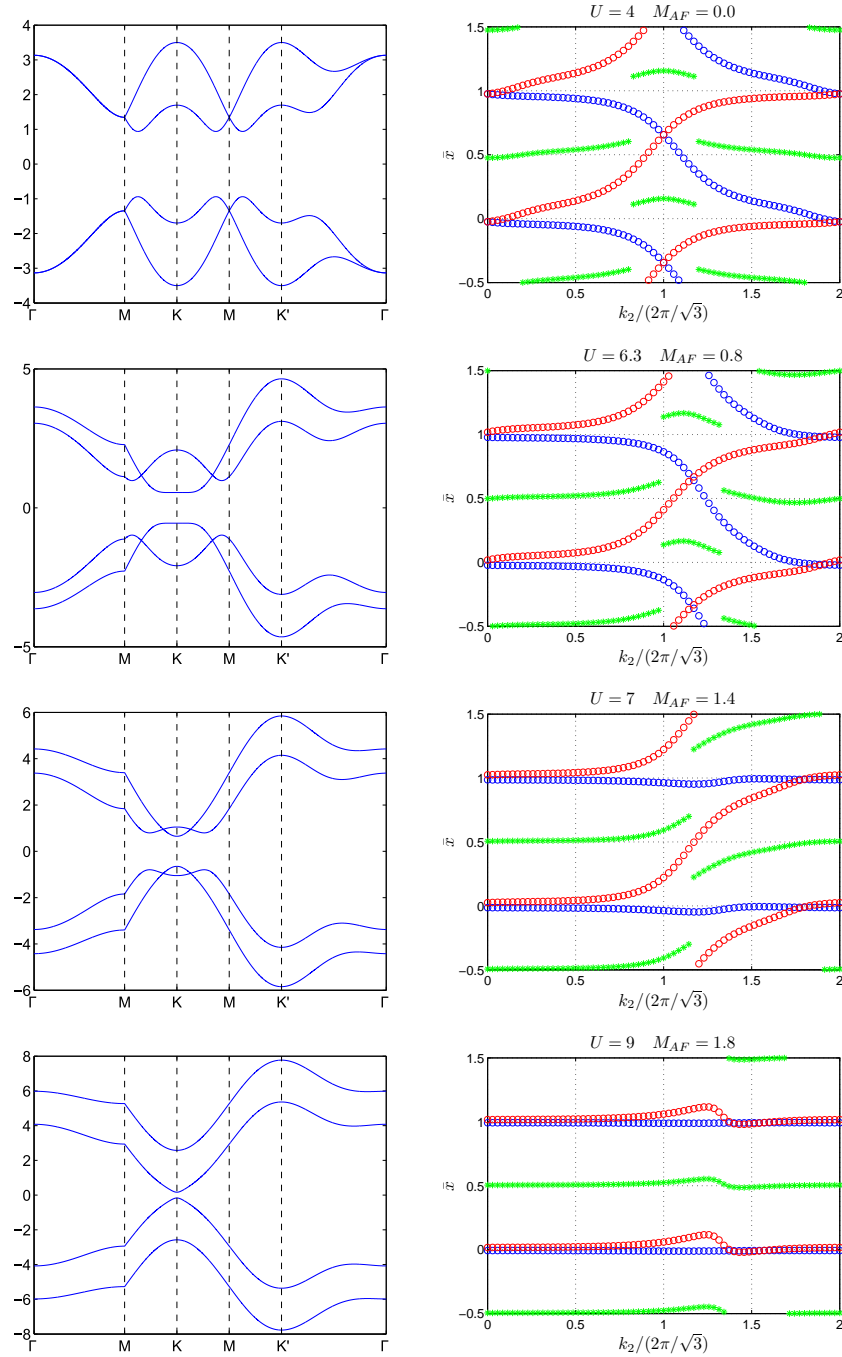


Figure 3.8: Bands and Wannier charge centers for $\lambda_{SO} = 0.5$, $\lambda_\nu = 3\lambda_{SO}$ and $\lambda_R = 0$ for various values of U .

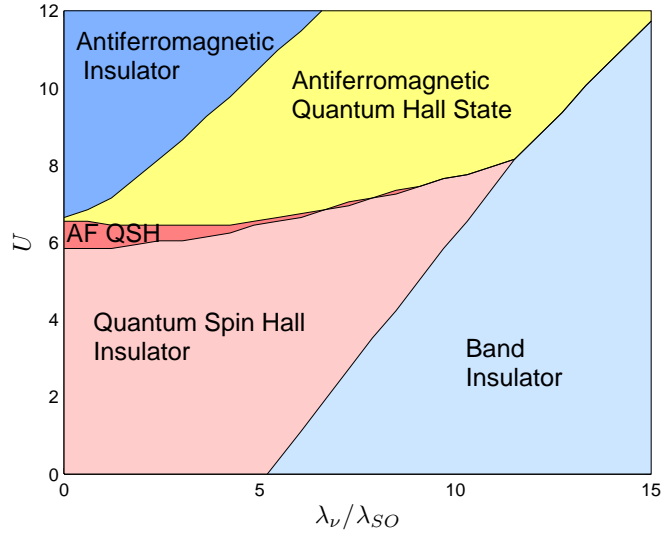


Figure 3.9: Phase diagram of the Kane-Mele-Hubbard model in mean-field approximation as a function of U and λ_ν for $\lambda_{SO} = 0.5$ and $\lambda_R = 0$.

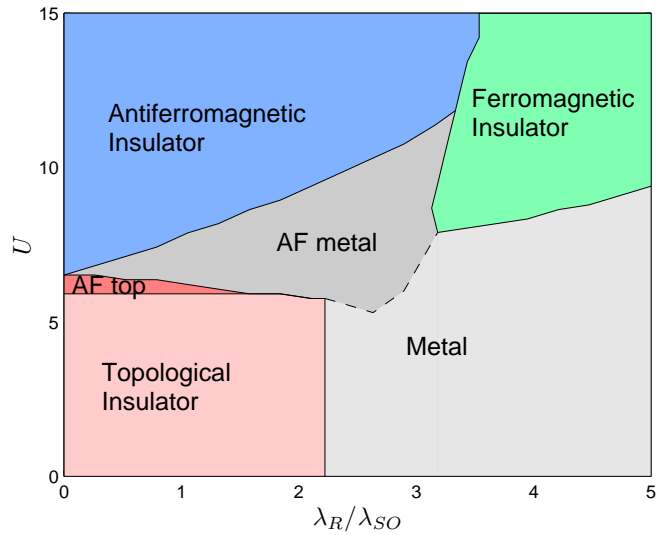


Figure 3.10: Phase diagram of the Kane-Mele-Hubbard model in mean-field approximation as a function of U and λ_R for $\lambda_{SO} = 0.5$ and $\lambda_\nu = 0$. The phase boundary between the two different metallic phases is dashed since the onset of magnetisation is inaccurately determined from the self consistency equation if the system is not gapped.

insulator if $\lambda_R < \lambda_R^c \approx 2.23\lambda_{SO}$ and metallic if $\lambda_R > \lambda_R^c$. In the other limiting case, $\lambda_R = 0$, an antiferromagnetic moment appears for $U > U_1^c$ which destroy the topological order for $U > U_2^c$. If both parameters are present, it turns out that U_1^c , the onset of magnetisation, hardly changes as long as $\lambda_R < \lambda_R^c$. In fact, the relative change is within 3%. Furthermore, the critical Rashba coupling remains constant within numerical accuracy of 10^{-4} as U is varied as long as the antiferromagnetic moment vanishes (see figure 3.10).

As already mentioned, for $\lambda_R = 0$ a magnetisation appears with increasing U that decreases the bandgap and finally closes it at $U = U_2^c$. For larger values, it reopens again. For $0 < \lambda_R < \lambda_R^c$ the behaviour is similar: Magnetisation closes the band gap, but in contrast to $\lambda_R = 0$ the band gap remains closed for a finite interval $U \in (U_{2\text{close}}^c, U_{2\text{open}}^c)$. This metallic phase is conceptionally different to the first one mentioned above, since here not only the Rashba coupling causes the gap close, but the interplay of Rashba coupling with rising magnetisation. Furthermore, in section 3.2 it is shown for the case $\lambda_R = 0$ that the topology is nontrivial before the gap close even if an antiferromagnetic moment is present, but it becomes trivial for $U > U_2^c$. There is strong evidence that this holds also for $\lambda_R \neq 0$ since the gap does not close as Rashba coupling rises from 0. However, it is still important to consider the topology since λ_R breaks the conservation of spin in z direction. This has the consequence that it is not possible to track the Wannier charge centers individually since they cannot be ordered by spin any more. If no magnetisation is present and hence the Hamiltonian is time reversal invariant, this is no substantial problem since the Fu-Kane definition (1.53) together with Soluyanov-Vanderbilt method can be used, as described in section 2.3.3. However, if $\lambda_R \neq 0$ and $U > U_1^c$, \mathcal{T} symmetry and spin conservation are broken, which means that the \mathbb{Z}_2 invariant by Fu and Kane is not defined as well as C_\uparrow , C_\downarrow and C_s . A generalisation of the definition by Fu-Kane is given in section 3.2.1. With this method it is provable that the a generalised invariant ν remains 1 until the gap closes and that it becomes trivial when it opens again. The possible inaccuracies mentioned in section 3.2.1 due to jumps in the maximum interspace function $z(k_2)$ without accompanied crossings of the WCC are for the model and parameters here not relevant since the crossings for $U < U_{2\text{close}}$ are always clearly detectable, whereas no jump in $z(k_2)$ appears for $U > U_{2\text{open}}$. Examples for the WCC within each phase are given in figure 3.11. It is important to mention that this generalised topological structure is different to the spin Chern structure realized in the case $\lambda_R = 0$ since less symmetries are present. If both spin conservation and time-reversal symmetry are violated (region labelled "AF top" in figure 3.10), edge states do non necessarily close the gap. This is analyzed later in section 3.5.2.

If both U and λ_R are large ($U \approx 7$, $\lambda_R \approx 3$), a ferromagnetic state rather than a antiferromagnetic state is realized. For $U = 13$ the magnetic moments are shown as a function of the Rashba coupling in figure 3.12. One sees that the transition is sharp, i.e. the ferromagnetic moment raises discontinuously at a critical Rashba coupling from 0 to a finite value whereas the antiferromagnetic moment drops to zero. The detailed phase boundaries are shown in figure 3.10.

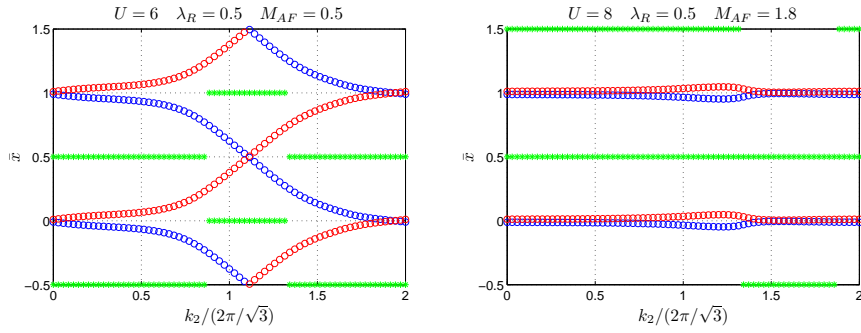


Figure 3.11: Wannier charge center of the Kane-Mele-Hubbard model in mean-field approximation for $\lambda_{SO} = 0.5$, $\lambda_\nu = 0$ and $\lambda_R = \lambda_{SO}$. The left picture with $U = 6$ shows a topological phase since the WCC are changing by 1 and -1 , respectively, within a period. The invariant in the right with $U = 8$ is trivial.

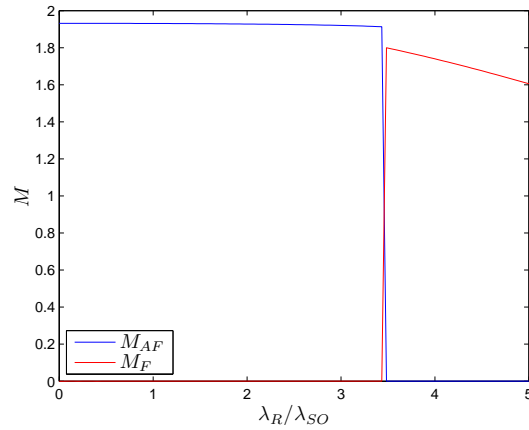


Figure 3.12: Magnetic moments as a function of λ_R for $\lambda_{SO} = 0.5$, $\lambda_\nu = 0$ and $U = 13$.

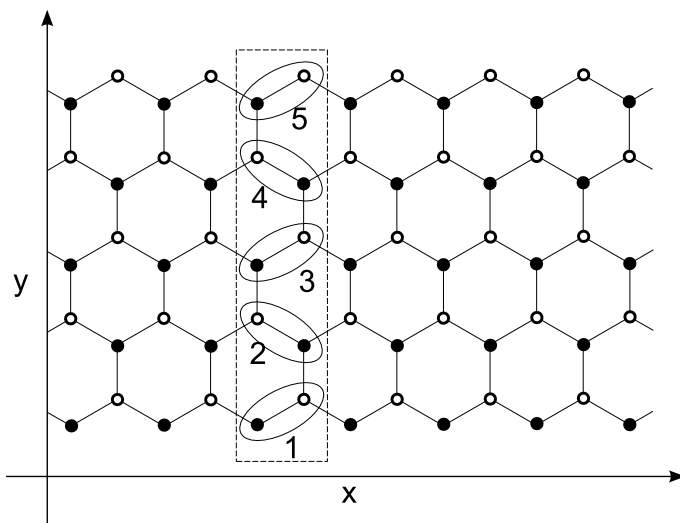


Figure 3.13: Pairing of A and B sites along the unit cell of a zigzag ribbon from $l = 1$ to $l = N = 5$. Note that the orientation is different for pairs with even index l and for those with odd l .

3.5 KMH model on a zigzag ribbon

The Kane-Mele-Hubbard model shows in mean-field approximation a variety of different topological and magnetic phases. In order to cross check the results obtained for the bulk, the model is analysed in this section on a zigzag ribbon, especially to see whether the number of edge states and their properties are consistent with the topological structure.

3.5.1 Magnetisation

In contrast to the 2D bulk lattice, the unit cell of a zigzag ribbon contains N sites of each sublattice, as shown in section 2.4 and especially in figure 2.19. Since the different sites within a unit cell are independent, the particle densities and thus the magnetic moments may vary along the width of the ribbon. The self consistency equation (3.9) is still valid, but with the difference that the combined index r consists not only of spin and sublattice, but also of the position index in y direction. Because of half filling, the total density is fixed $\sum_r \langle n_r \rangle = 2N$. Therefore, the number of independent variables that have to be determined self consistently is $4N - 1$. In the bulk case, the four densities have been transformed to the three independent parameters M_{AF} , M_F and ΔN_{AB} . In order to compare with the results from the ribbon, the transformation is performed here as well for each pair of sites. The way the sites are grouped is shown in figure 3.13.

The behaviour of magnetisation of the KMH model as a function of U is known from bulk results: A non magnetic state is realised up to a threshold U_1^c and a growing antiferromagnetic moment appears for higher U . The actual

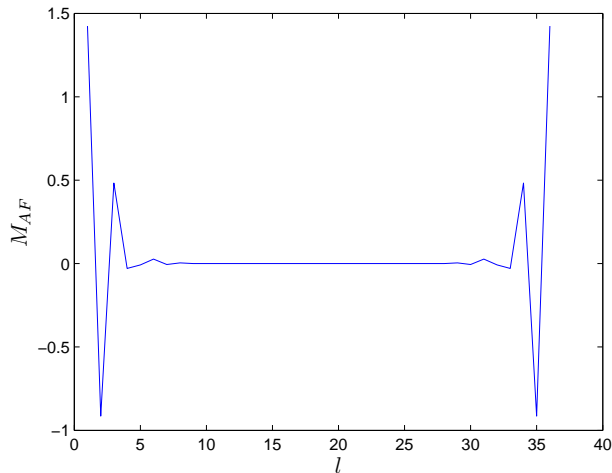


Figure 3.14: Antiferromagnetic moment along a ribbon of width $N = 36$ as a function of pair index l (see figure 3.13) for $U = 5.7$, $\lambda_{\text{SO}} = 0.5$.

value of the Kane-Mele parameters (λ_{SO} , λ_{ν} and λ_{R}) changes the threshold interaction and the value of magnetisation, but does not affect the qualitative behaviour. The only exception are very high Rashba couplings, see section 3.4. Therefore, the rising magnetisation is analysed here for fixed $\lambda_{\text{SO}} = 0.5$, $\lambda_{\nu} = \lambda_{\text{R}} = 0$. From the bulk the threshold interaction is known to be $U_1^c \approx 5.84$. As expected, for small $U \ll U_1^c$ the magnetisation vanishes throughout the ribbon, for large $U \gg U_1^c$ M_{AF} is approximately constant along the ribbon and close to the saturation value of 2. For interactions a bit smaller than the bulk threshold, a finite antiferromagnetic moment appears along the edges. An example is given in figure 3.14. Note that the antiferromagnetic moment of pairs is shown and not spin densities of single sites. Hence, the magnetic order at the edges is $\downarrow\uparrow\downarrow\uparrow\downarrow\uparrow\downarrow \dots$ and not $\uparrow\downarrow\uparrow\downarrow \dots$ as in the bulk for large U . To analyse the ordering as interaction varies, the antiferromagnetic moment of the first pair, the second pair, a pair situated in the middle of the ribbon and the average of the whole ribbon are plotted in figure 3.15. The magnetic moment vanishes for small U . At $U \approx 4.9$ a transition at the edges happens with an ordering explained above. The threshold for ordering in the middle of the ribbon is $U \approx 5.9$ which is approximately the value found for the bulk. The middle region seems not to be affected from the edges since the ordering is $\uparrow\downarrow$ in contrast to $\downarrow\downarrow\uparrow\uparrow$ ordering still persisting at the boundaries. The last transition takes place at $U \approx 6.3$ where the edges adopt the ordering from the bulk.

3.5.2 Topology and edge states

In order to check the topologically distinct phases of diagram 3.9, the dispersion relation of one selected point within each phase has been calculated. The results are shown in figure 3.16 and can be compared with bulk results shown in figure 3.8. Because of the asymmetry of all curves one can see that the anti-

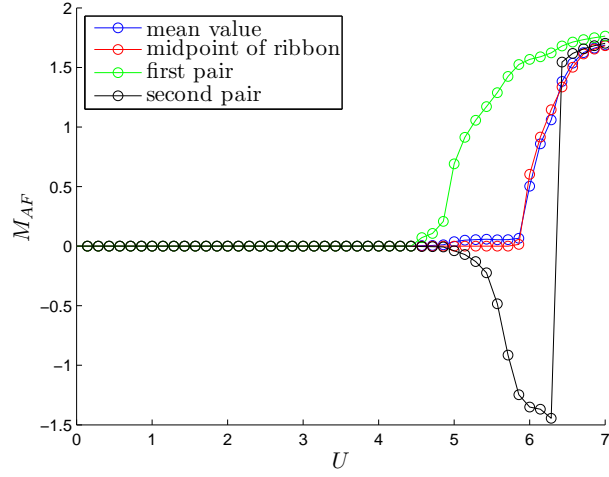


Figure 3.15: Antiferromagnetic moments of selected pairs of a ribbon of width $N = 36$ as a function of U for $\lambda_{\text{SO}} = 0.5$.

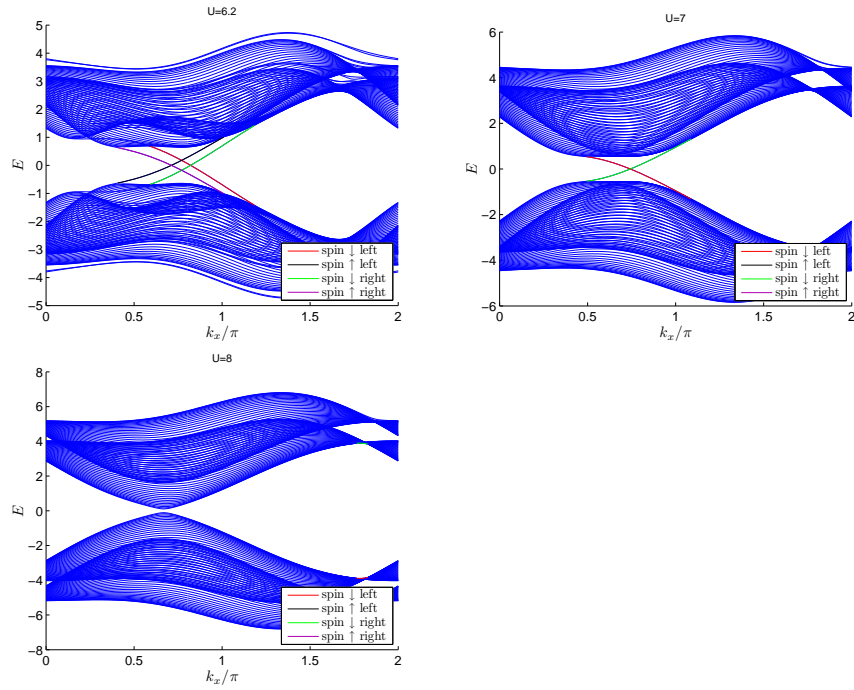


Figure 3.16: Dispersion relations of ribbons of width $N = 40$ for $\lambda_{\text{SO}} = 0.5$, $\lambda_{\nu} = 2\lambda_{\text{SO}}$ and $U = 6.2, 7$ and 8 .

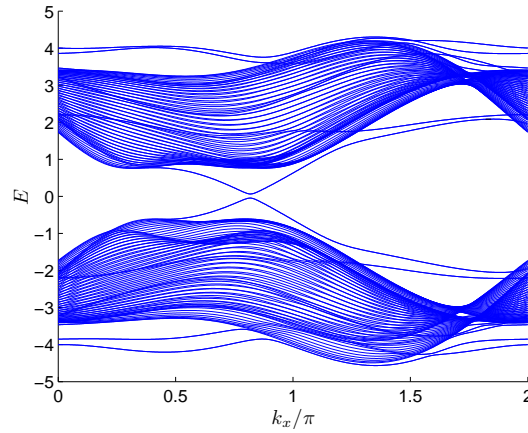


Figure 3.17: Dispersion relations of a ribbon of width $N = 40$ for $\lambda_{SO} = 0.5$, $\lambda_V = 0$, $\lambda_R = 0.1$ and $U = 6.2$.

ferromagnetic moment does not vanish throughout the ribbon in all three cases. In the first picture ($U = 6.3$), four edge states exist with the same structure as in the noninteracting case described in section 2.4, so two edge states exist on each edge, one with spin up and one with spin down. For $U = 7$, which is in a phase identified as quantum Hall state, only the edge states with spin down persist. This accords with the topological analyses in section 3.3 where it has been concluded that the spin up part of the Hamiltonian is trivial whereas the spin down part remains topological. For $U = 8$ the topology of the whole Hamiltonian is trivial and no edge states occur.

In the cases considered above, the picture of a spin Hall insulator explained in section 1.3.1 is applicable since the spin in z direction is conserved. A Rashba coupling destroys this symmetry, but preserves time-reversal symmetry and the topological \mathbb{Z}_2 structure if no interaction is present (see section 2.3.3). If a magnetic moment due to strong interaction and a Rashba coupling are present, both symmetries are broken. It is possible to generalize the topological invariant to this case using Wannier charge centers (see section 3.2.1), but the lack of symmetries changes the nature of the edge states. As shown in figure 3.17, the edge states are not necessarily gapless any more. For large Rashba couplings, the gap size can be even of the same order of magnitude as the bulk gap.

Chapter 4

Kane-Mele-Hubbard model beyond mean-field approximation

As mentioned in the previous chapter, the KMH model is a good system in order to understand the influence of interactions on topology. It is thus also expected to work as a toy model to test the advanced methods to determine topological constants explained in section 1.8. Therefore, it has been investigated by several methods after Rachel and Le Hur [48] first considered this model in mean-field approximation. The the critical U for a finite magnetisation has been examined for example with a determinant quantum Monte Carlo [49] as well as with a cellular dynamical mean-field theory [50]. The Variational Cluster Approach has also been used in order to determine the phases [50–52]. In the two latter references, the obtained Green's function of the inversion symmetric model is used to determine topological phases with equation (1.77). The aim of this chapter is to use also a self-energy-functional based method to calculate topological invariants even if inversion symmetry is broken, to look whether the topologically nontrivial phases with antiferromagnetic moment described in chapter 2 persist beyond mean-field approximation.

4.1 Self-energy-functional approach

Consider a Hamiltonian $H = H_0(\mathbf{t}) + H_1(\mathbf{U})$ consisting of a noninteracting part depending on a hopping matrix \mathbf{t} and an interacting one depending on an interaction tensor \mathbf{U} ,

$$H = \sum_{ij} t_{ij} c_i^\dagger c_j + \frac{1}{2} \sum_{ijkl} U_{ijkl} c_i^\dagger c_j^\dagger c_l c_k. \quad (4.1)$$

The Green's function of H_0 is given by $\mathbf{G}_0 = 1/(\omega + \mu - \mathbf{t})$ and determines together with the self-energy $\mathbf{\Sigma}$ the full Green's function \mathbf{G} via the Dyson equation $\mathbf{G} = \mathbf{G}_0 + \mathbf{G}_0 \mathbf{\Sigma} \mathbf{G}$ (see for example [47]). In contrast to the free Green's function, the self-energy is not known beforehand and can usually only be calculated approximately. In the following, the self-energy-functional approach [53]

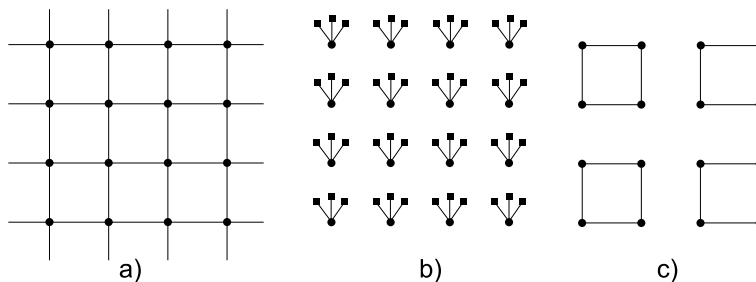


Figure 4.1: Reference systems for a quadratic lattice. In a), the original system is shown with a constant hopping between all nearest-neighbor sites. b) displays the reference system for a DIA with $n_s = 4$, c) the 4 site clusters of a VCA.

is summarized which is a frequently used method to estimate Σ . In 2003, the self-energy-functional

$$\Omega_{\mathbf{t}}[\Sigma] \equiv \text{Tr} \log \left(-(\mathbf{G}_0^{-1} - \Sigma)^{-1} \right) + F[\Sigma] \quad (4.2)$$

was first proposed by Potthoff [53]. $F[\Sigma]$ denotes the Legendre transform of the Luttinger-Ward functional $\Phi[\mathbf{G}]$ [53, 54]. The subscript \mathbf{t} indicates the dependence of the functional on the hopping through \mathbf{G}_0 . It can be shown [53] that the grand potential Ω is a stationary point of the self-energy-functional $\Omega_{\mathbf{t}}[\Sigma]$. The physical self-energy thus fulfils $\delta\Omega_{\mathbf{t}}[\Sigma] = 0$. The problem is that $\Omega_{\mathbf{t}}[\Sigma]$ is in general not known exactly. The approximation of this method is now to restrict the space of self energies Σ . This subset \mathcal{S} of all self energies is spanned by all $\Sigma(\mathbf{t}')$ that are the exact physical self energies of a so called reference system $H' = H_0(\mathbf{t}') + H_1(\mathbf{U})$, which has the same interaction part H_1 as the original system but a different hopping matrix. The reference system has to be solvable so that $\Sigma(\mathbf{t}')$ can be calculated. By varying \mathbf{t}' , $\Sigma(\mathbf{t}')$ is scanned through the restricted sub space in order to find the self-energy $\Sigma \in \mathcal{S}$ that gives the best solution of $\Omega_{\mathbf{t}}[\Sigma]$. Hence, the optimal solution within this approximation is a stationary point of the functional $\Omega_{\mathbf{t}}[\Sigma(\mathbf{t}')$. Note that \mathbf{t}' only influences the self-energy, the effect of the original hopping \mathbf{t} is present due to the parametric dependence of the functional $\Omega_{\mathbf{t}}$ on \mathbf{G}_0 . The parametrized functional can be reduced to [53]

$$\Omega_{\mathbf{t}}[\Sigma(\mathbf{t}')] = \Omega'(\mathbf{t}') + \text{Tr} \log \left(-(\mathbf{G}_0^{-1}(\mathbf{t}') - \Sigma(\mathbf{t}'))^{-1} \right) - \quad (4.3)$$

$$- \text{Tr} \log \left(-(\mathbf{G}_0^{-1}(\mathbf{t}) - \Sigma(\mathbf{t}'))^{-1} \right) \quad (4.4)$$

and can thus be calculated if the Green's function of the reference system is known.

A crucial role plays the reference hopping \mathbf{t}' . Rather simple systems are needed to compute the self-energy $\Sigma(\mathbf{t}')$, but they still need to be complex enough in order to host self energies close to the exact physical self-energy of the original system. The first considered reference system was a single impurity Anderson model (SIAM) for each lattice site [53] which is also frequently used as an impurity model for dynamical mean-field theory with exact diagonalisation

as impurity solver. The system that has to be solved exactly has n_s sites, consisting of one correlated impurity and $n_s - 1$ bath sites. An example with $n_s = 4$ is shown in figure 4.1 b). A self-energy-functional approach with SIAM reference system is usually called dynamical impurity approximation (DIA) [53, 55]. Another frequently used reference system consists of isolated clusters tiling up the original system, as in cluster perturbation theory. The resulting method is called variational cluster approach (VCA) [56], see also figure 4.1 c). The VCA incorporates the correlation effects correctly at length scales of the cluster and acts like a mean-field approximation beyond [57]. The clusters of a VCA may also include additional bath sites which makes the DIA to a special case of the VCA with minimal cluster size of one bath site. In addition to the bare hopping within a cluster and towards bath sites, a mean-field like Weiss field

$$H_W = \sum_i c_i^\dagger (\mathbf{h}_i \cdot \boldsymbol{\sigma}) c_i \quad (4.5)$$

can be used to handle spontaneous symmetry breaking [52, 58].

Once the reference system is defined, the stationary point of the VCA grand potential (4.3) has to be found. The first term $\Omega'(\mathbf{t}')$ is the grand potential of the reference system. The other two terms which are traces over the logarithm of Green's functions can be expressed simply by the single particle excitation energies of the respective Green's functions [55, 57]:

$$\text{Tr} \log \left(-(\mathbf{G}_0^{-1}(\mathbf{t}) - \boldsymbol{\Sigma}(\mathbf{t}'))^{-1} \right) - \text{Tr} \log \left(-(\mathbf{G}_0^{-1}(\mathbf{t}') - \boldsymbol{\Sigma}(\mathbf{t}'))^{-1} \right) = \quad (4.6)$$

$$= - \sum_m T \log(1 + e^{-\beta \omega_m}) + \sum_m T \log(1 + e^{-\beta \omega'_m}) = \quad (4.7)$$

$$\stackrel{T=0}{=} \sum_m \omega_m \Theta(-\omega_m) - \sum_m \omega'_m \Theta(-\omega'_m). \quad (4.8)$$

Here $\beta = 1/T$ is the inverse temperature and $\Theta(\omega)$ the Heaviside step function. ω_m are the poles of the VCA Green's function $\mathbf{G}_{\text{VCA}} = (\mathbf{G}_0^{-1}(\mathbf{t}) - \boldsymbol{\Sigma}(\mathbf{t}'))^{-1}$, ω'_m are the poles of the reference system's Green's function $\mathbf{G}' = (\mathbf{G}_0^{-1}(\mathbf{t}') - \boldsymbol{\Sigma}(\mathbf{t}'))^{-1}$. Supposed that the poles of the reference system can be determined, the poles of \mathbf{G}_{VCA} can be calculated as well using following procedure [57]: First, \mathbf{G}' has to be expressed in Lehmann representation in the form [57, 59]

$$G'_{\alpha\beta} = \sum_m Q_{\alpha m} \frac{1}{\omega - \omega'_m} Q_{m\beta}^\dagger, \quad (4.9)$$

where $\omega'_m = E_s - E_r$ is the pole resulting from an excitation from state $|r\rangle$ to another state $|s\rangle$. For $T = 0$, the Q -matrices are given by

$$Q_{\alpha m} = \delta_{r,0} \langle 0 | c_\alpha | s \rangle + \delta_{s,0} \langle r | c_\alpha | 0 \rangle. \quad (4.10)$$

Defining the difference between physical system and reference system as $\mathbf{V} \equiv \mathbf{t} - \mathbf{t}'$ and the diagonal matrix of the reference system's poles $\Lambda_{mn} \equiv \delta_{mn} \omega'_m$, the excitation energies ω_m are the eigenvalues of the matrix $\mathbf{M} = \mathbf{\Lambda} + \mathbf{Q}^\dagger \mathbf{V} \mathbf{Q}$.

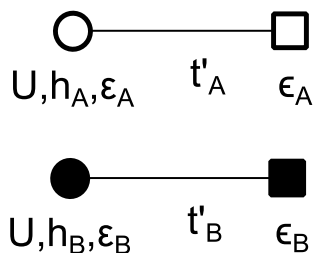


Figure 4.2: Reference system of a $n_s = 2$ DIA for 2 sites per unit cell. The total reference system is a multiplication of this cluster for each unit cell, see figure 4.1b).

4.2 Kane-Mele-Hubbard model in 2 site DIA

As mentioned in the previous section, the selection of the reference system may have an influence on the result. How symmetries of the chosen cluster affect topological properties can be seen for example in [60]. In that paper, the Haldane-Fermi-Hubbard model (Haldane model (2.11) with nearest-neighbor interaction $V \sum_{\langle i,j \rangle} n_i n_j$ but without on-site potential M) has been analysed using exact diagonalisation. The Chern invariant is calculated using twisted boundary conditions (1.70). For small V , the system is a topological insulator, for large V in a charge density wave order. Depending on the cluster geometry, the CDW and topological order coexist. If a cluster is chosen that preserves the symmetry of the honeycomb lattice, the coexisting phase vanishes. The Haldane model is related to the Kane-Mele model and the topological CDW region corresponds to the topological antiferromagnetic region discussed in mean-field approximation (section 2.3). Hence, there is evidence that the existence of a topological AF phase could possibly depend on the cluster geometry of a VCA. Therefore, a DIA (e.g. a single site cluster VCA) is chosen here in order to analyse the phase diagram of the KMH model since all symmetries are inherently conserved. A disadvantage of that approach is that the self-energy is local so that basically a mean-field theory is considered. However, an improvement to the mean-field approximation in chapter 3 is that due to the undefined magnetisation direction and the hopping to bath sites a much more flexible system is considered. The number of bath sites is chosen here to 1, the total number of sites is hence $n_s = 2$. This keeps the effort to calculate the poles of the reference system marginal and still reproduces the phase diagram for the Mott transition, as analysed in detail for the Hubbard model on a square lattice in [55]. To analyse magnetic transitions, additionally a Weiss field (4.5) is added.

The used clusters consist of a correlated impurity of interaction strength U with on site energy ε and a Weiss field \mathbf{h} , and of an uncorrelated bath site with on site energy ϵ , see figure 4.2. The two sites are linked through a hopping t' . The total reference system is an infinite number of such clusters, one for each site of the physical system. Note that the variational parameters (\mathbf{h} , ϵ , ε and t') of clusters on A sites might be different from those on B sites, wherefore the total number of parameters is 12 if no constraints or symmetries are considered.

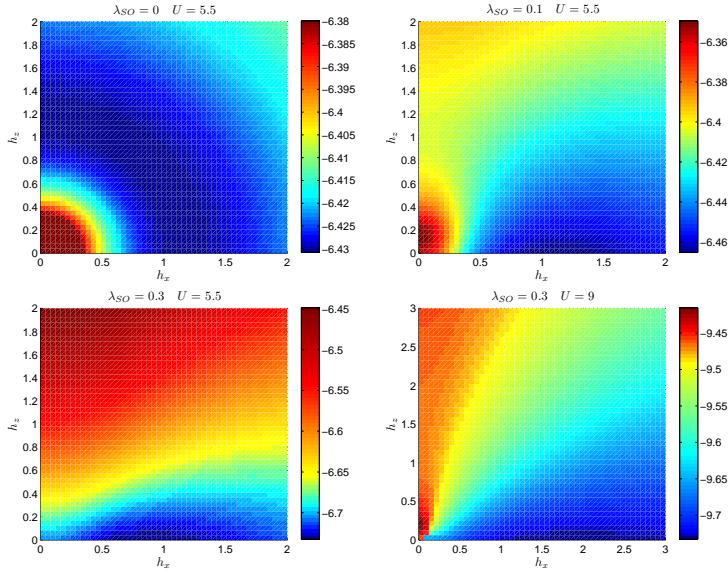


Figure 4.3: Examples of the self-energy-functional as a function of the Weiss field for already optimized hopping t' . A Discussion of the stationary points is given in the text, see also [52].

To generate a phase diagram of the KMH model as a function of λ_{SO} and U for vanishing sublattice potential and Rashba coupling as in figure 3.2, the number of parameters can be reduced. First, lattice sites A and B are identical wherefore the only allowed difference between the two clusters is due to an unequal symmetry breaking Weiss field, which reduces the parameters by 3, i.e. $\mathbf{h}_A \neq \mathbf{h}_B$, $\epsilon_A = \epsilon_B$, $\epsilon_A = \epsilon_B$, $t'_A = t'_B$. Furthermore, particle hole symmetry forces the energy of the impurity to be zero, $\epsilon = 0$. The bath sites have to be arranged symmetrically as well and since here only one bath site is added the energy is fixed to the chemical potential, i.e. $\epsilon = \mu = U/2$. Thus, except for the Weiss field, the only parameter that has to be varied is t' . The Weiss fields \mathbf{h}_A and \mathbf{h}_B can be varied in principle without restriction, but symmetries can be used to reduce the effort. The KMH Hamiltonian is symmetric in exchanging x and y coordinate, therefore also the potential $\Omega_t[\boldsymbol{\Sigma}(t')]$ obeys the same symmetry. Hence, only h_x and h_z have to be considered since the set of all solutions can be generated by rotating the special solution $\mathbf{h} = (h_x, 0, h_z)$ around the z axis. In addition, because of the mean-field results in chapter 3 it is assumed that only antiferromagnetism will be physical. Hence, $\mathbf{h}_B = -\mathbf{h}_A$. This can be easily checked by adding small ferromagnetic moments in addition to the observed stationary point in order to see if it is stable. To sum up, only three parameters are varied in order to find a stationary point: h_x , h_z and t' .

The direction of a magnetic moment is not known beforehand. In order to check it, the stationary t' has been calculated for various values of h_x and h_z , the resulting potential $\Omega_t[\boldsymbol{\Sigma}(h_x, h_z, t'_{\text{best}}(h_x, h_z))]$ is shown in figure 4.3. For the bare Hubbard model on a hexagonal lattice, i.e. $\lambda_{SO} = 0$, not just h_x and h_y are equivalent, but also h_z due to $SU(2)$ spin symmetry. If U is small, a minimum

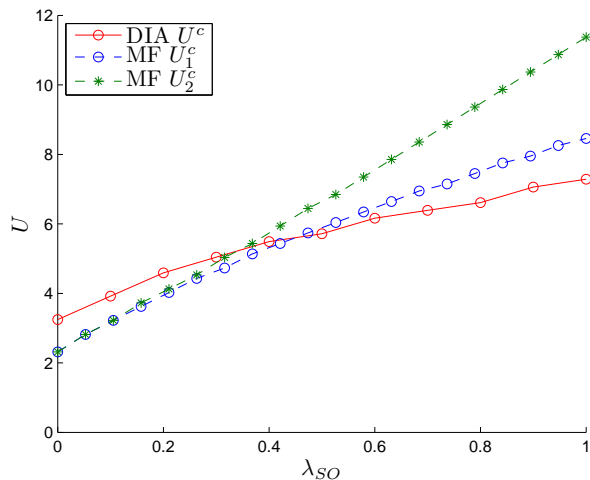


Figure 4.4: Phase diagram of the KMH model for $\lambda_\nu = \lambda_R = 0$ using a two site DIA. The phase boundary is shown as a solid red line. In comparison, the mean-field results are shown in dashed lines, the magnetic transition U_1^c in blue and the topological transition U_2^c in green.

at $\mathbf{h} = 0$ is the only stationary point. Over a critical interaction this point becomes a maximum and the minimum shifts to a finite value of $|\mathbf{h}|$, see also figure 4.3 and [52]. If the spin-orbit coupling is raised from 0, the symmetry between x and z axis is lifted with the consequence that the functional is lower in h_x direction. In this regime, 3 different stationary points exist: A minimum along h_x axis, a maximum along h_z for small values of order 0.1, and a saddle point also along h_z but approximately of the same magnitude than the minimum. For different cluster geometries, only the minimum and the saddle point exist [52]. For even larger values of λ_{SO} , keeping U constant, the minimum with an anti-ferromagnetic Weiss field in x direction is the only stationary point. Looking at the changes of the stationary points as U is varied and λ_{SO} is kept constant, the first stationary point apart $\mathbf{h} = 0$ evolving with increasing U is the minimum in x direction. For large U also the saddle point and the maximum in z direction exist. However, for all values of spin-orbit coupling and interaction strength it turns out that the minimum of the potential is always achieved along the axis $h_z = 0$, which means that in order to determine the phase diagram only two parameters, h_x and t' , have to be varied. By inspection of $\Omega_t[\Sigma(h_x, t')]$ it turns out that the stationary point of interest with non vanishing t' and h_x is always a minimum. The minimisation of the potential with respect to the two parameters has been done using a Nelder-Mead downhill simplex algorithm. As in mean-field, the Weiss field vanishes if the interaction is small and has a finite value for large U . The threshold interaction $U_1^c(\lambda_{SO})$ is shown in figure 4.4. In comparison to the mean-field results (figure 3.2), the slope of the phase boundary is lower, i.e. for small spin-orbit couplings the threshold interaction is higher in DIA, for high λ_{SO} lower.

The topological properties can be calculated using the topological Hamil-

tonian, see section 1.8. The obtained VCA Green's function is a matrix of size 8. For the topological Hamiltonian, only the four dimensions of the impurity have to be considered, i.e. $H_{\text{top}}(\mathbf{k}) = \mathbf{G}_{\text{VCA impurity}}^{-1}(\mathbf{k})$. The resulting 4×4 matrix is identical to the Bloch Hamiltonian of the noninteracting system $H_0(\mathbf{k})$ with an additional constant self-energy Σ on the diagonal and a Weiss field in x direction. As a consequence, without magnetisation the topological Hamiltonian is, up to a constant that can be shifted into the chemical potential, identical to the noninteracting one. Therefore, also the WCC remain unchanged. Thus, without a magnetisation the topology cannot be changed. Above the critical interaction $U > U_1^c$, a finite antiferromagnetic moment in xy plane exists, that breaks time reversal symmetry and thus lifts Kramers degeneracy of the WCC $\bar{x}^I(k_2 = \sqrt{3}\pi/2) = \bar{x}^{II}(k_2 = \sqrt{3}\pi/2)$. An example is given in figure 4.5. Since the time reversal symmetry is broken and spin in z direction S_z is not conserved because of the magnetisation in x direction, the \mathbb{Z}_2 invariant is not defined beforehand. A discussion of this general case is given in section 3.2.1. As mentioned there, counting the discontinuities of the maximum interspace function $z(k_2)$ may lead to wrong results because of the loss of Kramers degeneracy (see also figure 4.5). However, the special case $\lambda_V = \lambda_R = 0$ provides symmetries for the WCC. First, as it is discussed in the mean-field chapter, $x^I(k_2) = -x^{II}(k_2) \bmod 1$ for Hamiltonians obeying inversion symmetry. Furthermore, as long as the magnetic moment in z direction vanishes, $x^s(k_2) = x^s(4\pi/\sqrt{3} - k_2)$ holds. As a consequence, a possible crossing of the WCC away from the TRIM $k_2 = 0$ and $k_2 = 2\pi/\sqrt{3}$, is doubled, just as in the time reversal symmetric case. The only difference is that the degeneracy at the TRIM is not guaranteed. Hence, topological properties are encoded at the Wannier charge centers at $k_2 = 2\pi/\sqrt{3}$. If the two WCC cross at this point, the topology can be determined using Soluyanov-Vanderbilt method (for the parameters here, it is always nontrivial), if not, the system is a trivial band insulator. Hence, the possible numerical problems described in section 3.2.1 cannot appear because of symmetries, only the TRIM $k_2 = 0$ and $k_2 = 2\pi/\sqrt{3}$ have to be checked.

It turns out that any magnetisation in x direction immediately destroys topological order. In contrast to the mean-field magnetisation in z direction, the intersection point of the two WCC curves is not shifted to a different momentum, but does not persist in the entire Brillouin zone. Each non vanishing magnetisation in x direction "gaps" the Wannier charge center curves, see figure 4.5. Hence, the DIA shows no antiferromagnetic topological phase as proposed by mean-field theory. The reason is the different direction of magnetisation. If only magnetisation in z direction was allowed and thus the saddle point was considered (see figure 4.3), the antiferromagnetic trivial phase would appear just as in the mean-field case. The transition because of a Weiss field in x direction is of a different kind than the transition caused by a field in z direction. The latter case is explained in detail in the mean-field chapter 3: An increasing magnetic moment shifts both bands and WCC, which can be assigned to a certain spin in z direction. Exactly when the band gap closes, the Chern invariant for each spin type changes to zero. In contrast, a magnetic moment in x direction does never close the band gap. The magnetic moment inherently breaks the conservation of S_z and thus topological order. It is not a topological quantum phase transition with a gap close as was always the case in mean-field approximation,

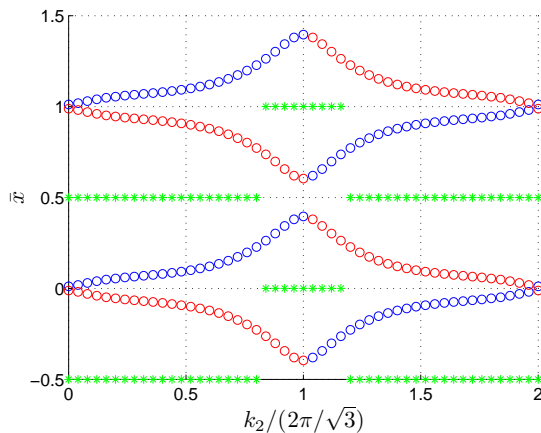


Figure 4.5: Wannier charge center of the topological Hamiltonian for $\lambda_{\text{SO}} = 0.5$ and $U = 5.7$. The resulting magnetisation in x direction is $h_x \approx 0.24$, the corresponding hopping to the bath sites $t' \approx 1.86$.

it is a topological transition due to a symmetry breaking.

If a sublattice potential λ_ν is included, the threshold interaction for an antiferromagnetic moment is increased, see figure 4.6. As already mentioned above, the DIA does not change the topological Hamiltonian if no Weiss field is present. The reason for that is that an unequal occupation of the two sublattices that has been seen in mean-field (see section 3.3) is not included in this model. Hence, in contrast to MF, the critical potential for a topological phase transition $\lambda_\nu^c = 3\sqrt{3}\lambda_{\text{SO}}$ does not depend on the interaction strength. A possible reason for that are the assumed symmetries between the two clusters on A and B sites. A relaxation of the constraints could change the phase boundaries, but increases the effort to find stationary points. Since for a first step beyond mean-field the reference system used here is sufficient, different clusters on the sublattices are postponed to future work.

For high interaction strengths, when an antiferromagnetic Weiss field is present, new phases as in the mean-field approach (see section 3.3) are expected. However, in DIA the system does not provide a topological antiferromagnetic phase due to the magnetisation in x direction. Additionally, the Quantum Hall phase obtained using mean-field approximation cannot be realized with a magnetisation in x direction since the WCC are symmetric around the TRIM $k_2 = 2\pi/\sqrt{3}$. This has the consequence that the total Chern number always has to vanish if $h_z = 0$. Except the antiferromagnetic region, the only additional phase caused by very strong interactions ($U \approx 20$) is a Mott insulator characterised by a decoupled cluster, i.e. $t' = 0$.

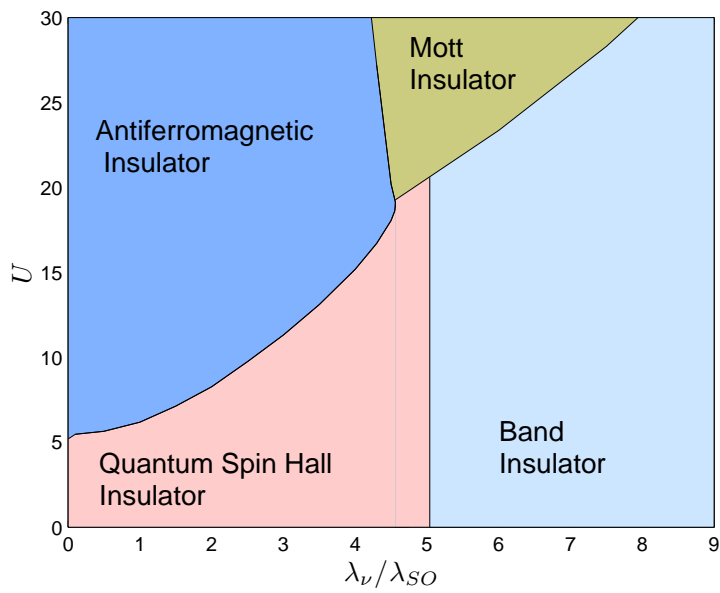


Figure 4.6: Phase diagram of the KMH model using a two site DIA for $\lambda_{SO} = 0.5$ and $\lambda_R = 0$.

Chapter 5

Conclusions and outlook

Calculating topological invariants for strongly correlated systems is an interesting and demanding task since the picture of a topological one-particle band structure is not compatible with the many-body framework enforced by interactions. In this thesis, the Kane-Mele-Hubbard model was investigated to understand the influence of an interaction on a topological insulator. First, the noninteracting Kane-Mele model was analyzed in order to get a clear picture of topological invariants in general and how they are affected by certain parameters. An introduction in topological invariants was given in chapter 1, resulting in the statement that the topological information is encoded in Wannier charge centers (WCC) which was highlighted by Soluyanov and Vanderbilt. This framework was used to explain the definition of the \mathbb{Z}_2 invariant given by Fu and Kane, which is suitable for time-reversal symmetric systems. Furthermore, another definition via the spin Chern number is given, which can only be used if the spin in z direction is conserved.

In chapter 2, the methods described above were applied to the noninteracting Kane-Mele model. It was analyzed how spin-orbit coupling, sublattice potential and Rashba coupling affect both band structure and WCC. Furthermore, the phase diagram valid for small spin-orbit couplings published by Kane and Mele was reproduced and expanded to large λ_{SO} . Finally, the results were compared to the existence of edge states at a zigzag ribbon to check the bulk-boundary correspondence, which showed perfect agreement.

In order to introduce an interacting term, the Kane-Mele-Hubbard (KMH) Hamiltonian was considered in mean-field approximation. This simple theory has been chosen in order to keep the WCC framework, which is based on the existence of Bloch states. In chapter 3, the phase diagram was analyzed in detail. It turned out that if the interaction U is large, an antiferromagnetic moment that breaks time-reversal symmetry appears. It is important to mention that the topological spin order persists even when the magnetic moment is finite. The topological order is destroyed if the magnetic order exceeds a critical value. Furthermore, an on-site potential λ_{ν} and a Rashba coupling λ_{R} were included, which causes additional phases. The spin ordering on the sublattices and the energetic difference due to λ_{ν} allow different absolute values of the two spin Chern numbers. Hence, for a certain parameter set, an anomalous Hall phase is

possible. The chapter was concluded with a check of bulk-boundary correspondence in mean-field theory, which showed again perfect agreement. However, if time-reversal symmetry and spin symmetry are broken simultaneously, the edge states are gapped.

In the last chapter 4, a two-site Dynamical Impurity Approximation (DIA) was used to check the existence of various phases in a first step beyond mean-field. So-called topological Hamiltonians, that had been already introduced at the end of chapter 1, were used in order to allow the calculation of WCC. It turned out that the magnetic moment aligns in x direction, as already published by several other groups using different clusters or methods. In the simple mean-field approximation of chapter 3, a magnetisation in z direction had been inherently assumed. The direction of magnetisation had great impact on the topological order, since other symmetries are imposed on the WCC. Within DIA, an antiferromagnetic quantum spin Hall state, which has been found in mean-field approximation, is not possible. Thus, one can conclude that the correct determination of the easy axis of a magnetic moment is of certain importance in order to determine the topology correctly.

The two-site DIA is a very simple model to test topology beyond mean-field. A further step would be to increase the cluster size in order to check the influence of a nonlocal self-energy. This increases of course the effort to calculate the topological Hamiltonian. A simpler addition to the work presented here would be a mean-field approximation where the x axis is the reference direction. This could possibly reproduce the DIA results qualitatively on a Hartree level. The final goal is of course to use different models closer to real systems to predict strongly correlated materials with nontrivial topology.

Appendix A

Kane-Mele Bloch Hamiltonians

A.1 Bulk

In this appendix, matrix representation (2.20) is derived by writing the Kane-Mele Hamiltonian

$$H_{\text{KM}} = -t \sum_{\langle i,j \rangle} c_i^\dagger c_j + i\lambda_{\text{SO}} \sum_{\langle\langle i,j \rangle\rangle} \nu_{ij} c_i^\dagger \sigma^z c_j \quad (\text{A.1})$$

$$+ i\lambda_{\text{R}} \sum_{\langle i,j \rangle} c_i^\dagger (\boldsymbol{\sigma} \times \hat{\mathbf{d}}_{ij})_z c_j + \lambda_{\nu} \sum_i \xi_i c_i^\dagger c_j$$

in the form $H_{\text{KM}} = \sum_{\mathbf{k}} \Psi_{\mathbf{k}}^\dagger H(\mathbf{k}) \Psi_{\mathbf{k}}$, using the basis $\Psi_{\mathbf{k}}^\dagger = (a_{\mathbf{k}\uparrow}^\dagger, b_{\mathbf{k}\uparrow}^\dagger, a_{\mathbf{k}\downarrow}^\dagger, b_{\mathbf{k}\downarrow}^\dagger)$, where $a_{\mathbf{k}\uparrow}^\dagger$ creates a spin up particle with momentum \mathbf{k} on sublattice A . The lattice geometry is defined in section 2.1. Lattice sites A are thus situated at $\mathbf{R} = n\mathbf{a}_1 + m\mathbf{a}_2$, lattice sites B at $\mathbf{R} + \boldsymbol{\delta}_1$. Hence, spinors $c^\dagger \equiv (c_\uparrow^\dagger, c_\downarrow^\dagger)$ are transformed to momentum space by

$$c_{\mathbf{R}}^\dagger = a_{\mathbf{R}}^\dagger = \sum_{\mathbf{k}} e^{i\mathbf{k}\cdot\mathbf{R}} a_{\mathbf{k}}^\dagger \quad \text{if } i \in A, \quad (\text{A.2})$$

$$c_{\mathbf{R}}^\dagger = b_{\mathbf{R}}^\dagger = \sum_{\mathbf{k}} e^{i\mathbf{k}\cdot(\mathbf{R}+\boldsymbol{\delta}_1)} b_{\mathbf{k}}^\dagger \quad \text{if } i \in B. \quad (\text{A.3})$$

The transformation of the sublattice potential term $\lambda_{\nu} \sum_i \xi_i c_i^\dagger c_j$ is trivial since it is diagonal. In the following, each of the remaining three terms is transformed separately.

Tight-binding term:

$$-t \sum_{\langle i,j \rangle} c_i^\dagger c_j = -t \sum_{\langle i,j \rangle} (a_i^\dagger b_j + b_i^\dagger a_j) = -t \sum_{\langle i,j \rangle} a_i^\dagger b_j + \text{h.c.} \quad (\text{A.4})$$

$$\sum_{\langle i,j \rangle} a_i^\dagger b_j = \sum_{\mathbf{R}} \sum_{l=1}^3 a_{\mathbf{R}}^\dagger b_{\mathbf{R}+\delta_l} = \sum_{\mathbf{R}} \sum_{l=1}^3 \sum_{\mathbf{k}\mathbf{k}'} e^{i(\mathbf{k}\cdot\mathbf{R}-\mathbf{k}'\cdot(\mathbf{R}+\delta_l))} a_{\mathbf{k}}^\dagger b_{\mathbf{k}'} \quad (\text{A.5})$$

$$= \sum_{\mathbf{k}} \sum_{l=1}^3 e^{-i\mathbf{k}\cdot\delta_l} a_{\mathbf{k}}^\dagger b_{\mathbf{k}} \quad (\text{A.6})$$

The sum over nearest-neighbors is combined to $g_{\mathbf{k}}$, which has been already used in the dispersion relation of graphene (2.6). Simplifying the sum gives

$$g_{\mathbf{k}}/t \equiv \sum_{l=1}^3 e^{-i\mathbf{k}\cdot\delta_l} = e^{i\frac{k_y}{\sqrt{3}}} + e^{-i\left(\frac{k_x}{2} + \frac{k_y}{2\sqrt{3}}\right)} + e^{-i\left(-\frac{k_x}{2} + \frac{k_y}{2\sqrt{3}}\right)} \quad (\text{A.7})$$

$$= e^{i\frac{k_y}{\sqrt{3}}} + 2e^{-i\frac{k_y}{2\sqrt{3}}} \cos\left(\frac{k_x}{2}\right). \quad (\text{A.8})$$

The tight-binding term of the Kane-Mele model can thus be written as

$$-t \sum_{\langle i,j \rangle} c_i^\dagger c_j = \sum_{\mathbf{k}} g_{\mathbf{k}} a_{\mathbf{k}}^\dagger b_{\mathbf{k}} + \text{h.c.}, \quad (\text{A.9})$$

with $g_{\mathbf{k}}$ expressed above.

Spin-orbit coupling:

$$\sum_{\langle\langle i,j \rangle\rangle} \nu_{ij} c_i^\dagger \sigma^z c_j = \sum_{\langle\langle i,j \rangle\rangle} \nu_{ij} (c_{i\uparrow}^\dagger c_{j\uparrow} - c_{i\downarrow}^\dagger c_{j\downarrow}) \quad (\text{A.10})$$

$$= \sum_{\langle\langle i,j \rangle\rangle} \nu_{ij} (a_{i\uparrow}^\dagger a_{j\uparrow} - a_{i\downarrow}^\dagger a_{j\downarrow} + b_{i\uparrow}^\dagger b_{j\uparrow} - b_{i\downarrow}^\dagger b_{j\downarrow}) \quad (\text{A.11})$$

The 6 next-nearest-neighbor vectors are (see figure 2.1):

$$\Delta_{1,2} = \pm \mathbf{a}_1 = \pm \frac{1}{2} \begin{pmatrix} 1 \\ \sqrt{3} \end{pmatrix} \quad \Delta_{3,4} = \pm \mathbf{a}_2 = \pm \frac{1}{2} \begin{pmatrix} -1 \\ \sqrt{3} \end{pmatrix} \quad (\text{A.12})$$

$$\Delta_{5,6} = \pm (\mathbf{a}_1 - \mathbf{a}_2) = \pm \begin{pmatrix} 1 \\ 0 \end{pmatrix} \quad (\text{A.13})$$

Since the expression is similar for both sublattices, only sublattice A is treated here:

$$\sum_{\langle\langle i,j \rangle\rangle} \nu_{ij} a_{i\sigma}^\dagger a_{j\sigma} = \sum_{\mathbf{R}} \sum_{l=1}^6 \nu_{\Delta_l} a_{\mathbf{R}\sigma}^\dagger a_{\mathbf{R}+\Delta_l\sigma} \quad (\text{A.14})$$

$$= \sum_{\mathbf{R}} \sum_{l=1}^6 \sum_{\mathbf{k}\mathbf{k}'} \nu_{\Delta_l} e^{i(\mathbf{k}\cdot\mathbf{R}-\mathbf{k}'\cdot(\mathbf{R}+\Delta_l))} a_{\mathbf{k}\sigma}^\dagger a_{\mathbf{k}'\sigma} \quad (\text{A.15})$$

$$= \sum_{\mathbf{k}} \sum_{l=1}^6 \nu_{\Delta_l} e^{-i\mathbf{k}\cdot\Delta_l} a_{\mathbf{k}\sigma}^\dagger a_{\mathbf{k}'\sigma} \quad (\text{A.16})$$

As for the tight-binding term, the sum over l is combined to $\gamma_{\mathbf{k}}$. For the evaluation of the sum, $\Delta_l = -\Delta_{l+1}$ for l odd and $\nu_{\Delta} = -\nu_{-\Delta}$ can be used, which gives

$$\frac{\gamma_{\mathbf{k}}}{i\lambda_{\text{SO}}} \equiv \sum_{l=1}^6 \nu_{\Delta_l} e^{-i\mathbf{k}\cdot\Delta_l} = \sum_{l\text{ odd}} \nu_{\Delta_l} (e^{i\mathbf{k}\cdot\Delta_l} - e^{-i\mathbf{k}\cdot\Delta_l}) \quad (\text{A.17})$$

$$= \sum_{l\text{ odd}} \nu_{\Delta_l} 2i \sin(\mathbf{k} \cdot \Delta_l) \quad (\text{A.18})$$

$$= i \sin(k_x) - i \sin\left(-\frac{k_x}{2} + \frac{\sqrt{3}k_y}{2}\right) + i \sin\left(-\frac{k_x}{2} - \frac{\sqrt{3}k_y}{2}\right) \quad (\text{A.19})$$

$$= 4i \sin\left(\frac{k_x}{2}\right) \cos\left(\frac{\sqrt{3}k_y}{2}\right) - 2i \sin(k_x). \quad (\text{A.20})$$

For sublattice B , an overall minus sign appears since $\nu_{A\Delta_l} = -\nu_{B\Delta_l}$, see figure 2.4. Hence, the total spin-orbit term can be written as

$$i\lambda_{\text{SO}} \sum_{\langle\langle i,j \rangle\rangle} \nu_{ij} c_i^\dagger \sigma^z c_j = \sum_{\mathbf{k}} g_{\mathbf{k}} \left(a_{\mathbf{k}\uparrow}^\dagger a_{\mathbf{k}\uparrow} - a_{\mathbf{k}\downarrow}^\dagger a_{\mathbf{k}\downarrow} - b_{\mathbf{k}\uparrow}^\dagger b_{\mathbf{k}\uparrow} + b_{\mathbf{k}\downarrow}^\dagger b_{\mathbf{k}\downarrow} \right). \quad (\text{A.21})$$

Rashba term:

$$\sum_{\langle i,j \rangle} c_i^\dagger (\boldsymbol{\sigma} \times \hat{\mathbf{d}}_{ij})_z c_j = \sum_{\langle i,j \rangle} \begin{pmatrix} c_{i\uparrow}^\dagger & c_{i\downarrow}^\dagger \end{pmatrix} \begin{pmatrix} 0 & \hat{d}_y + i\hat{d}_x \\ \hat{d}_y - i\hat{d}_x & 0 \end{pmatrix} \begin{pmatrix} c_{j\uparrow} \\ c_{j\downarrow} \end{pmatrix} \quad (\text{A.22})$$

$$= \sum_{\langle i,j \rangle} \left(\hat{d}_y + i\hat{d}_x \right) c_{i\uparrow}^\dagger c_{j\downarrow} + \text{h.c.} \quad (\text{A.23})$$

Considering creation on sublattice A and annihilation on sublattice B , the relation $\sum_{\langle i,j \rangle} a_i^\dagger b_j = \sum_{\mathbf{k}} \sum_{l=1}^3 e^{-i\mathbf{k}\cdot\delta_l} a_{\mathbf{k}}^\dagger b_{\mathbf{k}}$ has been already proven in equation (A.6). In analogy, the relation

$$\sum_{\langle i,j \rangle} \left(\hat{d}_y + i\hat{d}_x \right) a_{i\uparrow}^\dagger b_{j\downarrow} = \sum_{\mathbf{k}} \sum_{l=1}^3 \left(\hat{\delta}_{ly} + i\hat{\delta}_{lx} \right) e^{-i\mathbf{k}\cdot\delta_l} a_{\mathbf{k}\uparrow}^\dagger b_{\mathbf{k}\downarrow} \quad (\text{A.24})$$

holds. It has been used that the difference vector \mathbf{d}_{ij} is equal to the nearest-neighbor vector $\boldsymbol{\delta}_l$. Inserting the nearest-neighbor vectors $\boldsymbol{\delta}_l$, the result for the sum over l is

$$\frac{\rho_{\mathbf{k}}}{i\lambda_{\text{R}}} \equiv \sum_{l=1}^3 \left(\hat{\delta}_{ly} + i\hat{\delta}_{lx} \right) e^{-i\mathbf{k}\cdot\delta_l} \quad (\text{A.25})$$

$$= -e^{-i\frac{k_y}{3}} + \left(\frac{1}{2} + i\frac{\sqrt{3}}{2} \right) e^{i\left(\frac{k_x}{2} + \frac{k_y}{2\sqrt{3}}\right)} + \left(\frac{1}{2} - i\frac{\sqrt{3}}{2} \right) e^{i\left(-\frac{k_x}{2} + \frac{k_y}{2\sqrt{3}}\right)} \quad (\text{A.26})$$

$$= -e^{-i\frac{k_y}{\sqrt{3}}} + e^{i\frac{k_y}{2\sqrt{3}}} \left(\cos\left(\frac{k_x}{2}\right) - \sqrt{3} \sin\left(\frac{k_x}{2}\right) \right), \quad (\text{A.27})$$

which defines the term $\rho_{\mathbf{k}}$. In the term which is related to a hopping from A to B , the difference vector \mathbf{d}_{ij} in equation (A.23) is not $\boldsymbol{\delta}_l$, but $-\boldsymbol{\delta}_l$. It is easy

to see that a transformation $\delta \rightarrow -\delta$ leads to $\rho_{\mathbf{k}} \rightarrow -\rho_{-\mathbf{k}}$. Hence, the Rashba term in momentum spaces takes the form

$$i\lambda_R \sum_{\langle i,j \rangle} c_i^\dagger (\boldsymbol{\sigma} \times \hat{\mathbf{d}}_{ij})_z c_j = \sum_{\mathbf{k}} \left(\rho_{\mathbf{k}} a_{\mathbf{k}\uparrow}^\dagger b_{\mathbf{k}\downarrow} - \rho_{-\mathbf{k}} b_{\mathbf{k}\uparrow}^\dagger a_{\mathbf{k}\downarrow} \right) + \text{h.c.} \quad (\text{A.28})$$

with $\rho_{\mathbf{k}}$ defined in equation A.27.

To sum up, after a Fourier transformation the three terms of the Kane-Mele take the form (A.9), (A.21) and (A.28). Writing these expressions and the sublattice potential term in matrix form as defined by equation 2.19, the Bloch Hamiltonian (2.20) is obtained. The explicit form of the coefficients $g_{\mathbf{k}}$, $\gamma_{\mathbf{k}}$ and $\rho_{\mathbf{k}}$ given in the equations (2.21-2.23) is proven as can be seen from the relations (A.8), (A.20) and (A.27).

A.2 Zigzag ribbon

In the case of a bulk material, the transversal invariance in both x and y direction can be used to write the Hamiltonian in a block diagonal form (the Hamiltonian is diagonal in momentum \mathbf{k}) so that only 4 degrees of freedom remain. A ribbon is translational invariant in only one direction. The unit cell of a zigzag ribbon is shown in figure 2.19. The size of the block diagonal parts for each k_x is the number of sites in the unit cell times 2 (spin degree of freedom). In order to have no dangling bonds, the number of sites of sublattice A within a unit cell has to be equal to the number of sites of sublattice B and is in the following denoted by N . We used, as in the bulk case, $\Psi_{k_x}^\dagger \equiv (a_{k_x\uparrow}^\dagger, b_{k_x\uparrow}^\dagger, a_{k_x\downarrow}^\dagger, b_{k_x\downarrow}^\dagger)$ as a basis. Here, however, $c_{k_x\sigma}^\dagger \equiv (c_{k_x1\sigma}^\dagger, c_{k_x2\sigma}^\dagger, \dots, c_{k_xN\sigma}^\dagger)$ is a vector of length N . Therefore, $\Psi_{k_x}^\dagger$ has dimension $4N$. The Bloch Matrix $H(k_x)$ has the block form

$$H(k_x) = \begin{pmatrix} H_{A\uparrow A\uparrow} & H_{A\uparrow B\uparrow} & H_{A\uparrow A\downarrow} & H_{A\uparrow B\downarrow} \\ H_{A\uparrow B\uparrow}^\dagger & H_{B\uparrow B\uparrow} & H_{B\uparrow A\downarrow} & H_{B\uparrow B\downarrow} \\ H_{A\uparrow A\downarrow}^\dagger & H_{B\uparrow A\downarrow}^\dagger & H_{A\downarrow A\downarrow} & H_{A\downarrow B\downarrow} \\ H_{A\uparrow B\downarrow}^\dagger & H_{B\uparrow B\downarrow}^\dagger & H_{A\downarrow A\downarrow}^\dagger & H_{B\downarrow B\downarrow} \end{pmatrix} \quad (\text{A.29})$$

where each block will be sparse (maximum tridiagonal for zigzag, pentadiagonal for armchair ribbons) since only nearest and next-nearest-neighbor interactions are considered. The analysis here is similar to the bulk case in section A.1. Therefore, only one hopping type within each term will be considered, for example, from $A \uparrow$ to $B \downarrow$ in the case of the Rashba coupling. The other hoppings can be easily reconstructed using the results of the bulk in section A.1 by comparing the block form of Bloch Hamiltonian (A.29) of the ribbon with the Bloch Hamiltonian (2.20) of the bulk. For example, $H_{A\uparrow A\uparrow}(k_x) = H_{B\uparrow B\uparrow}(k_x)$ and $H_{A\uparrow B\downarrow}(k_x) = -H_{B\uparrow A\downarrow}(-k_x)$. The only qualitative difference to the bulk case is that the index m representing the y component remains since no translational symmetry in this direction is given. Therefore, m is the index or the row or the column, respectively, of the block matrices in equation (A.29).

Tight-binding term:

$$\sum_{\langle i,j \rangle} a_i^\dagger b_j = \sum_{\mathbf{R}} \sum_{l=1}^3 a_{\mathbf{R}}^\dagger b_{\mathbf{R}+\delta_l} \quad (\text{A.30})$$

$$= \sum_{nm} \sum_{l=1}^3 \sum_{k_x k'_x} e^{i(k_x R_x^n - k'_x (R_x^n + \delta_x^l))} a_{k_x m}^\dagger b_{k_x m + d^l} \quad (\text{A.31})$$

$$= \sum_{k_y} \sum_m \sum_{l=1}^3 e^{-ik_x \delta_x^l} a_{k_x m}^\dagger b_{k_x m + d^l} \quad (\text{A.32})$$

$$= \sum_{k_y} \sum_n \left(e^{-ik_y \frac{\sqrt{3}}{2}} a_{k_x m}^\dagger b_{k_x m + 1} + e^{ik_y \frac{\sqrt{3}}{2}} a_{k_x m}^\dagger b_{k_x m + 1} + \right. \quad (\text{A.33})$$

$$\left. + a_{k_x m}^\dagger b_{k_x m - 1} \right) \quad (\text{A.34})$$

$$= \sum_{k_y} \sum_m 2 \left(\cos \left(k_x \frac{\sqrt{3}}{2} \right) a_{k_x m}^\dagger b_{k_x m + 1} + a_{k_x m}^\dagger b_{k_x m - 1} \right) \quad (\text{A.35})$$

Spin-orbit coupling:

$$\sum_{\langle\langle i,j \rangle\rangle} \nu_{ij} a_{i\sigma}^\dagger a_{j\sigma} = \sum_{\mathbf{R}} \sum_{l=1}^6 \nu_{\Delta_l} a_{\mathbf{R}\sigma}^\dagger a_{\mathbf{R}+\Delta_l\sigma} \quad (\text{A.36})$$

$$= \sum_{nm} \sum_{l=1}^6 \sum_{k_x k'_x} \nu_{\Delta_l} e^{i(k_x R_x^n - k'_x (R_x^n + \Delta_x^l))} a_{k_x m\sigma}^\dagger a_{k_x m + D^l\sigma} \quad (\text{A.37})$$

$$= \sum_{k_x} \sum_m \sum_{l=1}^6 \nu_{\Delta_l} e^{-ik_x \Delta_x^l} a_{k_x m\sigma}^\dagger a_{k_x m + D^l\sigma} \quad (\text{A.38})$$

As shown in figure 2.19, pairs of next-nearest-neighbor sites having the same y coordinate Δ_y can be formed. The x component within a pair changes by factor of -1 , wherefore, as in equation (A.17), $\nu_{\Delta_x, \Delta_y} = -\nu_{-\Delta_x, \Delta_y}$ can be used to combine the exponential terms to sinuses. The final result is

$$\begin{aligned} \sum_{\langle\langle i,j \rangle\rangle} \nu_{ij} a_{i\sigma}^\dagger a_{j\sigma} = \sum_{k_x} \sum_m \left[-2 \sin \left(k_x \sqrt{3} \right) a_{k_x m\sigma}^\dagger a_{k_x m\sigma} + \right. \\ \left. + 2 \sin \left(k_x \frac{\sqrt{3}}{2} \right) a_{k_x m\sigma}^\dagger a_{k_x m + 1\sigma} + \right. \\ \left. + 2 \sin \left(k_x \frac{\sqrt{3}}{2} \right) a_{k_x m\sigma}^\dagger a_{k_x m - 1\sigma} \right]. \end{aligned} \quad (\text{A.39})$$

Rashba coupling:

$$\sum_{\langle i,j \rangle} (\hat{d}_y + i\hat{d}_x) a_{i\uparrow}^\dagger b_{j\downarrow} =$$

$$= \sum_m \sum_{k_x} \sum_{l=1}^3 (\hat{\delta}_{ly} + i\hat{\delta}_{lx}) e^{-ik_x \delta_{lx}} a_{k_x m \uparrow}^\dagger b_{k_x m + d_l \downarrow} \quad (\text{A.40})$$

$$= \frac{1}{2} \sum_{k_x} \sum_m \left[(\sqrt{3} + i) e^{-ik_y \frac{\sqrt{3}}{2}} a_{k_x m \uparrow}^\dagger b_{k_x m + 1 \downarrow} + \right. \\ \left. + (-\sqrt{3} + i) e^{ik_y \frac{\sqrt{3}}{2}} a_{k_x m \uparrow}^\dagger b_{k_x m + 1 \downarrow} - 2i a_{k_x m \uparrow}^\dagger b_{k_x m - 1 \downarrow} \right] \quad (\text{A.41})$$

$$= i \sum_{k_x} \sum_m \left[\left(-\sqrt{3} \sin \left(k_y \frac{3}{2} \right) + \cos \left(k_y \frac{3}{2} \right) \right) a_{k_x m \uparrow}^\dagger b_{k_x m + 1 \downarrow} - \right. \\ \left. - 2a_{k_x m \uparrow}^\dagger b_{k_x m - 1 \downarrow} \right] \quad (\text{A.42})$$

With these results, the block matrices of equation (A.29) can be constructed easily. For instance, $H_{A\uparrow A\uparrow}$ is determined by equation (A.39) and has for $N = 5$ the form

$$H_{A\uparrow A\uparrow}(k_x) = \begin{pmatrix} \alpha & \beta & 0 & 0 & 0 \\ \beta & \alpha & \beta & 0 & 0 \\ 0 & \beta & \alpha & \beta & 0 \\ 0 & 0 & \beta & \alpha & \beta \\ 0 & 0 & 0 & \beta & \alpha \end{pmatrix} \quad (\text{A.43})$$

with $\alpha = -2 \sin(k_x \sqrt{3})$ and $\beta = 2 \sin\left(k_x \frac{\sqrt{3}}{2}\right)$.

Bibliography

- [1] M. V. Berry. Quantal phase factors accompanying adiabatic changes. *Proceedings of the Royal Society of London. A. Mathematical and Physical Sciences*, 392(1802):45–57, 1984.
- [2] Yoichi Ando. Topological Insulator Materials. *Journal of the Physical Society of Japan*, 82(10):102001, 2013.
- [3] Katharina Durstberger. Geometric phases in quantum theory. Master’s thesis, Universität Wien, 2002.
- [4] Mikio Nakahara. *Geometry, Topology and Physics*. Institute of Physics Publishing, Dirac House, Temple Back, Bristol BS1 6BE, UK, 2 edition, 2003.
- [5] Mahito Kohmoto. Topological invariant and the quantization of the Hall conductance. *Annals of Physics*, 160(2):343 – 354, 1985.
- [6] J. E. Avron, R. Seiler, and B. Simon. Homotopy and Quantization in Condensed Matter Physics. *Phys. Rev. Lett.*, 51:51–53, Jul 1983.
- [7] M. Z. Hasan and C. L. Kane. Colloquium: Topological insulators. *Rev. Mod. Phys.*, 82:3045–3067, Nov 2010.
- [8] Wu-Yi Hsiang and Dung-Hai Lee. Chern-Simons invariant in the Berry phase of a 2×2 Hamiltonian. *Phys. Rev. A*, 64:052101, Oct 2001.
- [9] K. v. Klitzing, G. Dorda, and M. Pepper. New method for high-accuracy determination of the fine-structure constant based on quantized hall resistance. *Phys. Rev. Lett.*, 45:494–497, Aug 1980.
- [10] D. J. Thouless, M. Kohmoto, M. P. Nightingale, and M. den Nijs. Quantized Hall Conductance in a Two-Dimensional Periodic Potential. *Phys. Rev. Lett.*, 49:405–408, Aug 1982.
- [11] Wolfgang Nolting. *Quantenmechanik - Grundlagen*. Springer-Verlag, Berlin, Heidelberg, 7 edition, 2009.
- [12] C. L. Kane and E. J. Mele. Quantum spin hall effect in graphene. *Phys. Rev. Lett.*, 95:226801, Nov 2005.
- [13] M. Hohenadler and F. F. Assaad. Correlation effects in two-dimensional topological insulators. *Journal of Physics: Condensed Matter*, 25(14):143201, 2013.

- [14] D. N. Sheng, Leon Balents, and Ziqiang Wang. Phase diagram for quantum hall bilayers at $\nu = 1$. *Phys. Rev. Lett.*, 91:116802, Sep 2003.
- [15] D. N. Sheng, Z. Y. Weng, L. Sheng, and F. D. M. Haldane. Quantum spin-hall effect and topologically invariant chern numbers. *Phys. Rev. Lett.*, 97:036808, Jul 2006.
- [16] Franz Schwabl. *Quantenmechanik für Fortgeschrittene (QMII)*. Springer-Verlag, Berlin, Heidelberg, 5 edition, 2008.
- [17] Gregory H. Wannier. The structure of electronic excitation levels in insulating crystals. *Phys. Rev.*, 52:191–197, Aug 1937.
- [18] E.I. Blount. Formalisms of band theory. volume 13 of *Solid State Physics*, pages 305 – 373. Academic Press, 1962.
- [19] Nicola Marzari and David Vanderbilt. Maximally localized generalized Wannier functions for composite energy bands. *Phys. Rev. B*, 56:12847–12865, Nov 1997.
- [20] Liang Fu and C. L. Kane. Time reversal polarization and a Z_2 adiabatic spin pump. *Phys. Rev. B*, 74:195312, Nov 2006.
- [21] Jean Dalibard Jean-Louis Basdevant. *Quantum Mechanics*. Springer-Verlag, Berlin, Heidelberg, New York, 1 edition, 2005.
- [22] Liang Fu and C. L. Kane. Topological insulators with inversion symmetry. *Phys. Rev. B*, 76:045302, Jul 2007.
- [23] Alexey A. Soluyanov and David Vanderbilt. Computing topological invariants without inversion symmetry. *Phys. Rev. B*, 83:235401, Jun 2011.
- [24] Qian Niu, D. J. Thouless, and Yong-Shi Wu. Quantized Hall conductance as a topological invariant. *Phys. Rev. B*, 31:3372–3377, Mar 1985.
- [25] V. Gurarie. Single-particle green’s functions and interacting topological insulators. *Phys. Rev. B*, 83:085426, Feb 2011.
- [26] Grigory E. Volovik. The Universe in a Helium Droplet. volume 117 of *International Series of Monographs on Physics*, pages 305 – 373. Oxford University Press, 2003.
- [27] Andrew M. Essin and Victor Gurarie. Bulk-boundary correspondence of topological insulators from their respective Green’s functions. *Phys. Rev. B*, 84:125132, Sep 2011.
- [28] Zhong Wang, Xiao-Liang Qi, and Shou-Cheng Zhang. Topological invariants for interacting topological insulators with inversion symmetry. *Phys. Rev. B*, 85:165126, Apr 2012.
- [29] Zhong Wang and Shou-Cheng Zhang. Simplified topological invariants for interacting insulators. *Phys. Rev. X*, 2:031008, Aug 2012.
- [30] Zhong Wang and Binghai Yan. Topological hamiltonian as an exact tool for topological invariants. *Journal of Physics: Condensed Matter*, 25(15):155601, 2013.

- [31] R. Jackiw and C. Rebbi. Solitons with fermion number $\frac{1}{2}$. *Phys. Rev. D*, 13:3398–3409, Jun 1976.
- [32] W. P. Su, J. R. Schrieffer, and A. J. Heeger. Solitons in polyacetylene. *Phys. Rev. Lett.*, 42:1698–1701, Jun 1979.
- [33] B. I. Halperin. Quantized hall conductance, current-carrying edge states, and the existence of extended states in a two-dimensional disordered potential. *Phys. Rev. B*, 25:2185–2190, Feb 1982.
- [34] R. B. Laughlin. Quantized hall conductivity in two dimensions. *Phys. Rev. B*, 23:5632–5633, May 1981.
- [35] Robert B. Laughlin. Nobel Lecture: Fractional Quantization. http://www.nobelprize.org/nobel_prizes/physics/laureates/1998/laughlin-lecture.html, December 1998. [Online; Nobelprize.org. Nobel Media AB 2014. Web. 20 Feb 2015.].
- [36] Schulz-Baldes. Persistence of spin edge currents in disordered quantum spin Hall system. *Commun. Math. Phys.*, 324:589–600, 2013.
- [37] M. Porta G. M. Graf. Bulk-edge correspondence for two-dimensional topological insulators . *Commun. Math. Phys.*, 324:851–895, 2013.
- [38] K. S. Novoselov, A. K. Geim, S. V. Morozov, D. Jiang, Y. Zhang, S. V. Dubonos, I. V. Grigorieva, and A. A. Firsov. Electric field effect in atomically thin carbon films. *Science*, 306(5696):666–669, 2004.
- [39] D. C. Elias, R. R. Nair, T. M. G. Mohiuddin, S. V. Morozov, P. Blake, M. P. Halsall, A. C. Ferrari, D. W. Boukhvalov, M. I. Katsnelson, A. K. Geim, and K. S. Novoselov. Control of graphene’s properties by reversible hydrogenation: Evidence for graphane. *Science*, 323(5914):610–613, 2009.
- [40] P. R. Wallace. The Band Theory of Graphite. *Phys. Rev.*, 71:622–634, May 1947.
- [41] A. H. Castro Neto, F. Guinea, N. M. R. Peres, K. S. Novoselov, and A. K. Geim. The electronic properties of graphene. *Rev. Mod. Phys.*, 81:109–162, Jan 2009.
- [42] F. D. M. Haldane. Model for a quantum hall effect without landau levels: Condensed-matter realization of the ”parity anomaly”. *Phys. Rev. Lett.*, 61:2015–2018, Oct 1988.
- [43] Shuichi Murakami. Quantum spin hall phases. *Progress of Theoretical Physics Supplement*, 176:279–301, 2008.
- [44] C. L. Kane and E. J. Mele. Quantum spin hall effect in graphene. *Phys. Rev. Lett.*, 95:226801, Nov 2005.
- [45] Jean-Christophe Charlier, Xavier Blase, and Stephan Roche. Electronic and transport properties of nanotubes. *Rev. Mod. Phys.*, 79:677–732, May 2007.

- [46] J. Hubbard. Electron correlations in narrow energy bands. *Proceedings of the Royal Society of London A: Mathematical, Physical and Engineering Sciences*, 276(1365):238–257, 1963.
- [47] Wolfgang Nolting. *Viel-Teilchen-Theorie*. Springer-Verlag, Berlin, Heidelberg, New York, 6 edition, 2009.
- [48] Stephan Rachel and Karyn Le Hur. Topological insulators and mott physics from the hubbard interaction. *Phys. Rev. B*, 82:075106, Aug 2010.
- [49] Dong Zheng, Guang-Ming Zhang, and Congjun Wu. Particle-hole symmetry and interaction effects in the kane-mele-hubbard model. *Phys. Rev. B*, 84:205121, Nov 2011.
- [50] Wei Wu, Stephan Rachel, Wu-Ming Liu, and Karyn Le Hur. Quantum spin hall insulators with interactions and lattice anisotropy. *Phys. Rev. B*, 85:205102, May 2012.
- [51] Jan Carl Budich, Ronny Thomale, Gang Li, Manuel Laubach, and Shou-Cheng Zhang. Fluctuation-induced topological quantum phase transitions in quantum spin-hall and anomalous-hall insulators. *Phys. Rev. B*, 86:201407, Nov 2012.
- [52] Manuel Laubach, Johannes Reuther, Ronny Thomale, and Stephan Rachel. Rashba spin-orbit coupling in the Kane-Mele-Hubbard model. *Phys. Rev. B*, 90:165136, Oct 2014.
- [53] Potthoff, M. Self-energy-functional approach to systems of correlated electrons. *Eur. Phys. J. B*, 32(4):429–436, 2003.
- [54] J. M. Luttinger and J. C. Ward. Ground-state energy of a many-fermion system. ii. *Phys. Rev.*, 118:1417–1427, Jun 1960.
- [55] M. Potthoff. Self-energy-functional approach: Analytical results and the mott-hubbard transition. *The European Physical Journal B - Condensed Matter and Complex Systems*, 36(3):335–348, 2003.
- [56] M. Potthoff, M. Aichhorn, and C. Dahnken. Variational cluster approach to correlated electron systems in low dimensions. *Phys. Rev. Lett.*, 91:206402, Nov 2003.
- [57] M. Aichhorn, E. Arrigoni, M. Potthoff, and W. Hanke. Variational cluster approach to the hubbard model: Phase-separation tendency and finite-size effects. *Phys. Rev. B*, 74:235117, Dec 2006.
- [58] David Sénéchal. An introduction to quantum cluster methods. arXiv:0806.2690v2 [cond-mat.str-el], November 2010.
- [59] Marc G. Zacher, Robert Eder, Enrico Arrigoni, and Werner Hanke. Evolution of the stripe phase as a function of doping from a theoretical analysis of angle-resolved photoemission data. *Phys. Rev. B*, 65:045109, Jan 2002.
- [60] Christopher N. Varney, Kai Sun, Marcos Rigol, and Victor Galitski. Topological phase transitions for interacting finite systems. *Phys. Rev. B*, 84:241105, Dec 2011.